M. Bittens

A Parametric Modeling Concept for Predicting Biomechanical Compatibility in Total Hip Arthroplasty

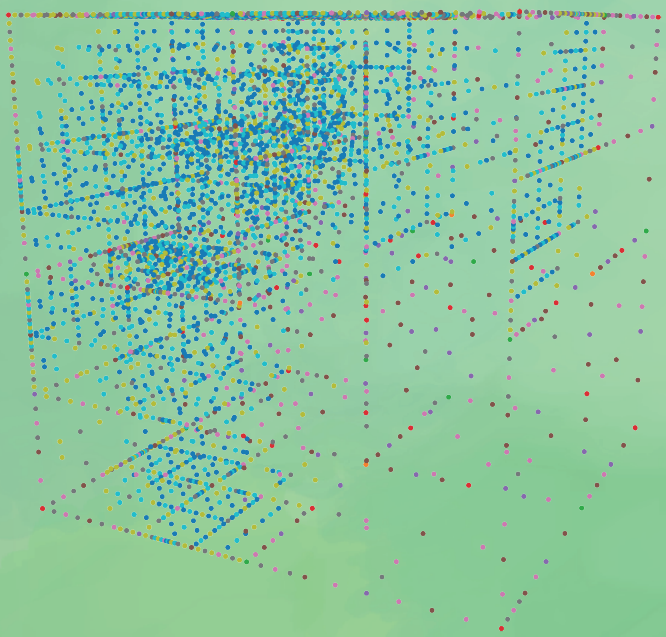

F 21/01 Institut für Baumechanik
und Numerische Mechanik
Gottfried Wilhelm Leibniz Universität Hannover

ibnm
A Parametric Modeling Concept for Predicting Biomechanical Compatibility in Total Hip Arthroplasty
M. Bittens
F 21/01

Erratum

Erratum zur Dissertation „A parametric modeling concept for predicting biomechanical compatibility in total hip arthroplasty“ vorgelegt von Maximilian Bittens, 2020.

Seite 56
In der algorithmisch konsistenten Materialtangente fehlt der innere Ableitungsterm

$$\left(\varrho_{(n)} + \Delta\varrho^{(k)}\right)^{n-1} .$$

Um diesen ergänzt lautet die Materialtangente:

$$\left.\frac{\partial \mathbb{C}(\varrho_{(n)} + \Delta\varrho^{(k)})}{\partial \boldsymbol{\varepsilon}^{*}_{(n+1)}}\right|_{\boldsymbol{\varepsilon}^{\mathrm{tr},(k)}_{(n+1)}} = n\varrho_0^{-n}\Delta t \cdot c \left(\varrho_{(n)} + \Delta\varrho^{(k)}\right)^{n-1} \left(\frac{\varrho_{(n)}}{\varrho_0}\right)^{n-m} \boldsymbol{\sigma}^{\mathrm{LE}(k)}_{(n+1)} \otimes \mathbb{C}^{\mathrm{LE}} .$$

Stand: 14.02.2023

A parametric modeling concept for predicting biomechanical compatibility in total hip arthroplasty

Von der

Fakultät für Bauingenieurwesen und Geodäsie
der Gottfried Wilhelm Leibniz Universität Hannover
zur Erlangung des Grades

Doktor-Ingenieur (Dr.-Ing.)

genehmigte Dissertation von

Maximilian Bittens, M.Sc.

Erscheinungsjahr 2021

Referent:
Prof. Dr.-Ing. U. Nackenhorst

Korreferenten:
Univ.-Prof. Dr.-Ing. Tim Ricken

Tag der Promotion:
26. November 2020

Herausgeber:
Prof. Dr.-Ing. U. Nackenhorst

Verwaltung:
Institut für Baumechanik und
Numerische Mechanik
Gottfried Wilhelm Leibniz Universität
Hannover
Appelstr. 9A
30167 Hannover
Tel.: +49 (0)511 / 762-3560
Fax.: +49 (0)511 / 762-19053

Maximilian Bittens

Institut für Baumechanik und
Numerische Mechanik
Gottfried Wilhelm Leibniz Universität
Hannover
Appelstr. 9A
30167 Hannover

Typeset in FreeSerif with LaTeX

ISBN 978-3-935732-53-6

Zusammenfassung

Computerassistierte Planung und Durchführung orthopädischer Eingriffe konnten sich trotz unbestreitbarer Vorteile wie die übersichtlichere Visualisierung des Operationsbereiches und die damit einhergehende bessere Planbarkeit sowie die durch Roboterassistenz gegebene Möglichkeit der präziseren Durchführung bis zum heutigen Tage nicht vollends durchsetzen. Dies liegt zum einen in den hohen Kosten begründet, zum anderen ist es fraglich, ob die meist längere Operationszeit und das damit verbundene höhere Infektionsrisiko durch ein besseres Operationsresultat und dem damit einhergehenden kleineren Revisionsrisiko aufgewogen wird.
Ein weiterer Grund für die mangelnde Akzeptanz dieser Methoden ist, dass diese meist rein visueller Natur sind. Das bedeutet, der Operateur bekommt besser aufgelöste Informationen, auf deren Grundlage er seine Operationstaktik begründen kann, sowie die Möglichkeit, diese genauer umzusetzen; eine *Entscheidungshilfe* bieten solche Systeme meist nicht oder in bisher nur unzureichender Form. Das Resultat ist, dass das Ergebnis der Operation ebenso wie vor der Einführung digitaler Hilfssysteme maßgeblich von der Erfahrung des Operateurs abhängig bleibt.
In dieser Arbeit wird deshalb versucht, am Beispiel der Hüftendoprothetik auf Grundlage verfügbarer patientenindividueller Informationen sowie möglicher Einbaupositionen der Prothese eine Vorhersage über das Langzeitresultat der Operation zu treffen. Dazu wird ein ganzheitliches Modellierungskonzept zur numerischen Simulation der Osseointegration und Langzeitstabilität von Endoprothesen unter Einbeziehung möglicher Prothesenpositionen entwickelt. Hierfür werden neue, effiziente und verlässliche Methoden zur numerischen Beschreibung des adaptiven Knochenumbaus und der Osseointegration vorgeschlagen:
Der adaptive Knochenumbau wird als geometrisch-lineares, materiell-nicht-lineares Finite-Element-Modell unter Beachtung der Richtlinien für thermodynamisch konsistente Materialmodellierung beschrieben. Die so erhaltenen Konstitutivgleichungen werden zur Beschreibung der Osseointegration erweitert und in ein *Kontaktinterface* zwischen Knochen und Prothese übertragen. Die Ergebnisse werden mithilfe einer neu entwickelten Simulation für Röntgenbilder in ein Format übertragen, welches für medizinisches Personal leichter zu interpretieren ist.
Das Einbeziehen möglicher Prothesenpositionen spannt einen unendlich-dimensionalen Ereignisraum auf. Deshalb wird das Modell mithilfe von Dimensionsreduktion in ein endlich-dimensionales Ersatzmodell überführt, welches anschließend mit einer adaptiven Kollokationsmethode für dünne Gitter abgetastet wird.
Jede einzelne der hier vorgestellten Methoden sowie das gesamte Modellierungskonzept wurde im Hinblick darauf entwickelt, dass diese der klinischen Validierung leicht zugänglich sein sollen. Ohne klinische Validierung können verlässliche Aussagen nicht getroffen werden, weshalb die in dieser Arbeit angeführten numerischen Beispiele als Beweis der korrekten Implementierung beziehungsweise als Machbarkeitsstudie angesehen werden können. Diese Dissertation gibt also eine Antwort auf die Frage, wie viel numerischer Aufwand betrieben werden muss, um für einen orthopädischen Eingriff eine echte digitale Entscheidungshilfe bereitzustellen.

Abstract

To this day, computer-aided orthopedic surgery has not been able to fully establish itself in clinical routine, despite obvious advantages, such as digital visualizations of the operational field and the resulting better planning, as well as more precise execution provided by robot assistance. On the one hand, this is due to the higher costs; on the other hand, it is questionable whether the usually longer operation time and the associated higher risk of infection will be outweighed by a better operation result and the associated lower risk of revision.
Another reason for the lack of acceptance of these methods is that they are highly visual in nature. This means that the surgeon receives better-resolved information based on which he can justify his surgical tactics, as well as the possibility of implementing them more precisely, but such systems usually do not offer a *decision aid* or, if they do, only to an insufficient extent. This results in a major dependency of the outcome of the operation, just as before the introduction of digital auxiliary systems, on the surgeon's experience.
Therefore, this work attempts to predict the long-term outcome of the operation using the example of total hip arthroplasty based on available patient-specific information and possible installation positions of the prosthesis. For this purpose, a holistic modeling approach for the numerical simulation of osseointegration and long-term stability of endoprostheses, including possible prosthesis positions, is developed. In addition, new, efficient and reliable methods for the numerical description of adaptive bone remodeling and osseointegration are proposed:
The adaptive bone remodeling is described as a geometric-linear, material-nonlinear finite element model, following thermodynamically consistent material modeling guidelines. The resulting constitutive equations are expanded to describe osseointegration and transferred into a contact interface between bone and prosthesis. Using a newly developed simulation for X-ray images, the results are projected to an imaging format that is easier to interpret for medical professionals.
The inclusion of possible prosthesis positions spans an infinite-dimensional event space. Therefore, the model is reduced to a finite-dimensional surrogate model sampled with an adaptive sparse-grid collocation method.
Each of the methods presented here and the entire modeling concept have been developed with regard to them being accessible for clinical validation. Without clinical validation, reliable statements cannot be made, and therefore the numerical examples given in this thesis can be regarded as proof of correct implementation and feasibility studies. This dissertation thus provides an answer to the question of how much computational effort is required to provide a real digital decision aid in orthopedic surgery.

Contents

Chapter 1

Introduction

This work addresses the numerical modeling of adaptation phenomena in biomechanical tissue, or more precisely, the ingrowth of bone substance into implanted hip prostheses and the subsequent remodeling of bone structure within the femur as a consequence of predefined patients individual characteristics, altered internal physiological conditions, and different prosthesis positions. This ultimately results in a comprehensive modeling approach for predicting change in bone mass following a hip replacement, which could be used to design a surgical guidance tool.

1.1 Motivation

Hip replacement is by far the most common of all orthopedic surgeries. In the year 2015, a total of 1.8 million hip replacement surgeries were performed worldwide. Projective studies suggest that there will be an increased demand for hip arthroplasty with presumably up to 2.8 million surgeries in 2050 [Pabinger et al., 2018]. Albeit also being one of the most successful orthopedic procedures performed nowadays [Gwam et al., 2017], with stated revision rates from $5 - 10\%$ within five years [Labek et al., 2011, Kandala et al., 2015, Bayliss et al., 2017], preliminary failure of hip prostheses amounts to great numbers with costs for revisions of 3.8 billion U.S. dollars in 2015 in the United States of America alone [Rajaee et al., 2018].
The age group with the fastest growth rate are persons aged 45-64 years [Chidambaram and Cobb, 2009, Rajaee et al., 2018], which in the medium-term will create a significant number of individuals outliving the expected lifetime of their prostheses by far [Schreurs and Hannink, 2017]. The increased risk of revision after a first prosthesis had been replaced due to failure [Ong et al., 2010] renders high-durable hip prostheses even more important.
Although surgical techniques have improved, the experience of surgeons and their proper planning of prostheses position remains a crucial factor in successful hip arthroplasty [Zenk et al., 2014, Shaikh, 2018, Jolbäck et al., 2018]. While computer-aided surgery was shown to increase the accuracy of the mounting position of prostheses [Chang et al., 2017], the efficient application thereof is questionable, and to this day, computer-aided systems are not prevalent in hip replacement surgery [Zagra, 2017].
For the surgeon to exploit the increased accuracy in the mounting position, two different conditions have to be fulfilled: (1) patient individual characteristics like geometry, age, bone condition, and weight would have to be included in the surgical planning in addition to the prosthesis position, all with an accuracy in the same order of magnitude and (2) the planning tool must be able to create and evaluate changes in the prosthesis position without additional modeling effort. Consequently, the need for a surgical guidance tool can be deduced, which predicts the secondary and long-term stability depending on the parameters mentioned above.

1.2 Problem description

Bone remodeling, bone growth, and bone healing are highly complex phenomena for the description of which different relevant length scales with associated dominant reaction processes have to be identified first. This includes, in descending order of length scale, mechanical, biological, and chemical processes as well as processes of physical chemistry at the molecular level, all of which are ongoing research topics in the scientific community, and some of these processes are not fully understood yet [Sabet et al., 2016].
Whilst not being impossible, the latter at least aggravates a *bottom-up* modeling approach, starting from the micro- or nanoscale and its efficient numerical treatment. This could have potentially resulted in the impracticability of the numerical description of bone growth processes if it had not been shown in the past that even phenomenological models based only on macroscopic observation lead to simulation results which were in good agreement with clinical studies [Huiskes, 1993]. It can be noted that even these macroscopic observations cannot be made to any degree of accuracy *in vivio* since they have to be measured indirectly from X-ray or CT scan. However, insights gained from these models led to a better understanding of the preliminary failure of hip prosthesis, such as aseptic loosening caused by stress-shielding [Inaba et al., 2016].
From this, it can be stated that one objective of this thesis is not to describe bone growth processes following hip surgery with the help of the most in-detail model possible, but rather to create a model which takes readily available patient individual data into account and provides a result of an expected bone-mass density distribution in which each input parameter has a relative error contribution in the same order of magnitude while being computational efficient at the same time. As a result, the presented framework should be applicable to address individual patient issues, like a patient-specific optimal prosthesis position.

1.3 State of the art

Computer-aided surgery is a widespread topic in the scientific community, and there are plenty of approaches trying to provide guidance in surgical planning. However, most of these approaches are purely visual in nature and mostly do not include any information about the biomechanical compatibility of the planned surgery.
First attempts of patient individual generation of finite element models from CT-data were provided by, amongst others, Keyak et al. [1990], Merz et al. [1991], Kang et al. [1993], or Viceconti et al. [1998a]; however, at this point, without any prospect of being integrated into clinical workflow. Only O'Toole III et al. [1995] carried out a first attempt in improving patient-specific preoperative planning by the use of two-dimensional models to analyze the altered stress distribution due to hip arthroplasty. A significant drawback of this early approach is the complexity of the application that made configuration, operation, and evaluation only possible by experts in numerical mechanics. A more user-friendly approach was stated in Lattanzi et al. [2002], where user-interface and visualization were designed along the lines of already established medical applications like radiographic projection software. This approach was found to improve the accuracy of preoperative planning [Viceconti et al., 2003], and even a first attempt incorporating the prediction of subject-specific primal stability was made [Reggiani et al., 2007]. Independent of the latter, a similar approach was stated in [Bah et al., 2011], by which different prosthesis positions can be generated through mesh-morphing, and subsequently, micro-motions between prosthesis and bone are used as an indicator for primal stability. Lutz [2011] was the first to provide a more comprehensive model by investigating both secondary and long-term stability in a joint approach. Concerning preoperative planning, a drawback here was that changes in individual patient characteristics are combined with great modeling effort.
As mentioned before, there are plenty of purely geometrical preoperative planning approaches, such as Davila et al. [2006] or Steinberg et al. [2010], where radiographic images combined with

CAD-models are used to improve preoperative planning. In Palit et al. [2019] a two-dimensional representation of the hip movement is stated, and thus an attempt is made to establish a relationship of the acetabular cup position and different failure modes of hip prostheses.
In Dick et al. [2008] and Dick et al. [2009] advanced three-dimensional visualization techniques are used to visualize the stress tensor field before and after hip replacement under the same loading condition in order to improve prostheses positioning.
In conclusion, it can be stated that a holistic approach in preoperative planning, which indicates the biomechanical compatibility of different prosthesis positions that is secondary and long-term stability, depending on available patient data and physical admissible prosthesis positions, is still missing.

1.4 Aims and objectives

The objective of this thesis is to provide a comprehensive modeling approach in the prediction of secondary and long-term stability in total hip arthroplasty, including different patient individual characteristics as well as *all* possible protheses position within a physical admissible range presuming primary stability is achieved during the surgery. This will be done with the aim of moving one step closer to the genuinely beneficial introduction of digital tools into the operational planning process.
Within this thesis, it can be distinguished between two different biomechanical processes that are *osseointegration* and *bone remodeling*, resulting in indicators for secondary and long-term stability, respectively, of implanted hip prostheses, which will be modeled in close analogy but still as separate processes. The tool of choice will be the finite element method because its application is tried and tested. Most methods and ideas used throughout this thesis were originally formulated using finite elements. Another important aspect here was the robust and efficient modeling of these biomechanical processes since they are subject to model order reduction, a concept introduced at a later stage.
The results will be transferred to a medical imaging format to be readily understandable for medical professionals. To this end, a new approach in virtual X-ray imaging will be proposed, operating directly onto finite element results, respecting element formulation of higher-order. Another advantage of this approach is the compression of the result format from complex three-dimensional finite element post-processing results to only two-dimensional radiographic images. Including all possible prosthesis positions, this problem is rendered computationally *unfeasible*. As already mentioned, to be computable, a surrogate model by hands of model order reduction has to be introduced. A simple discrete surrogate model using the *response surface methodology* will be sufficient. This approach was chosen because of its general applicability and its inherent interpolation property.
Concluding, it can be noted that all concepts used throughout this thesis should be constructed modularly, that is independent of each other, to be exchangeable in case a better solution for any subproblem in terms of accuracy, robustness, or efficiency is available, and in addition, to be readily a subject to clinical validation.

1.5 Structure of this thesis

Chapter 2 should give a brief introduction to the biomechanical foundations and processes. In this, the objective is **not** to explain all facts and figures comprehensively, since that is better done by specialists, but rather to introduce all necessary terms and concepts which are covered in this thesis. In **chapter 3**, the continuum mechanic fundamentals are outlined first to introduce a notation, which will be used throughout this thesis. As a next step, the balance laws within the framework of open thermodynamic systems are introduced, which will serve as a basis for consistent thermodynamic modeling. Concluding this chapter, a constitutive theory for bone remodeling is established. In **chapter 4**, the finite element approach used here

is introduced, which will serve as a basis for consistent linearizations and the incorporation of the constitutive relations and material responses into the global Newton-Raphson scheme. The automatic modeling approach is introduced in **chapter 5**, followed by the virtual X-ray imaging approach in **chapter 6**. Virtual X-ray imaging is used to facilitate the results and for the results to be comparable with DEXA images from clinical studies. In **chapter 7** and **chapter 8**, bone remodeling and the numerical simulation of osseointegration are described. While the former is modeled as a finite element material model, the latter is described by a *node-to-node* contact interface. Both methods are developed with great care, especially the consistent thermodynamic modeling and the consistent incorporation into the global Newton-Raphson scheme. Proof of the functionality of the methods is given by numerical examples. In **chapter 9**, the theory for the adaptive sparse-grid collocation method is re-stated, and a numerical example is provided to verify the implementation. In **chapter 10**, the overall modeling approach for the prediction of biomechanical compatibility in total hip arthroplasty is stated. Hereby, a fully abstract model is defined first to derive a reduced model thereof. In **chapter 11**, the function of the modeling approach is demonstrated by two numerical examples. Finally, **chapter 12** concludes the presented work.

Chapter 2

Biomechanical foundations

In the following chapter, biomechanical foundations required to describe a hip replacement surgery are briefly aggregated. The following summary does not claim completeness.

2.1 Anatomy of hip region

The term *hip region* refers to an anatomical region consisting out of *hip bone* and *femur*. The hip bone (see figure 2.1) consists of three parts: *ilium*, *ischium*, and *pubis*. While separated at

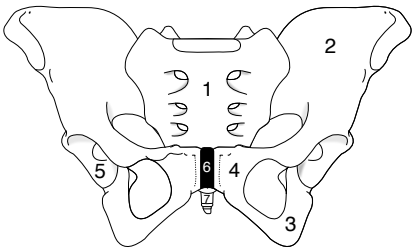

Figure 2.1: Human pelvis [based upon: © Fred the Oyster, 2014]: 1. Sacrum, 2. Ilium, 3. Ischium, 4. Pubis, 5. Acetabulum, 6. Pubic symphysis, 7. Coccyx

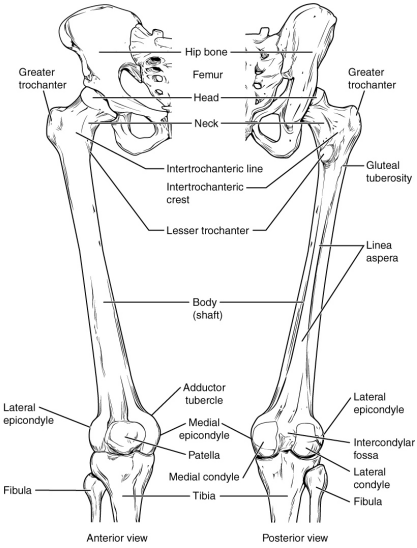

Figure 2.2: Femur and patella [© OpenStax College, 2013]

birth, these three parts will have fused to one region as an adult. The left and the right hip bone together with *pubic symphysis*, *sacrum*, and *coccyx* form the *pelvis*.
The femur or thigh bone (see figure 2.2) is the longest bone in human body and can be divided

in *upper part*, *body*, and *lower part*. The upper part consists of *head*, *neck*, *greater trochanter*, and *lesser trochanter*. The body or so-called *shaft* of the femur is a long, slender, and almost cylindrical bone. Part of it is the *linea apera*, which gives attachment to the preterm musculature (*adductors*). The lower femur consists out of two parts: the *medial condyle* and the *lateral condyle* which together forms one part of the knee joint.
The *hip joint* is formed by the rounded head of the femur and a concave surface of the pelvis, the so-called *acetabulum*. The acetabulum itself is shaped by parts of the ilium, ischium, and pubis. A comprehensive description of the anatomy of the hip region can be found, for example, in Netter et al. [1989] or Byrd [2012].

2.2 Hip replacement

Ultima ratio treatment for a painful hip is a hip replacement surgery. Hip replacement surgeries can be roughly separated into *total hip arthroplasty* (THA), where both parts of the hip joint, that is, the femoral head and acetabulum, are replaced by prosthetic implants and *hemi-arthroplasty*, where in general, only the femoral head is replaced. The main reason for hip replacement is a painful hip due to osteoarthritis, a joint disease where the cartilage of the hip joint is worn out. An illustration of a hip with osteoarthritis can be found in figure 2.3. There is a variety of causes for osteoarthritis, including, for example, obesity, joint injury, or

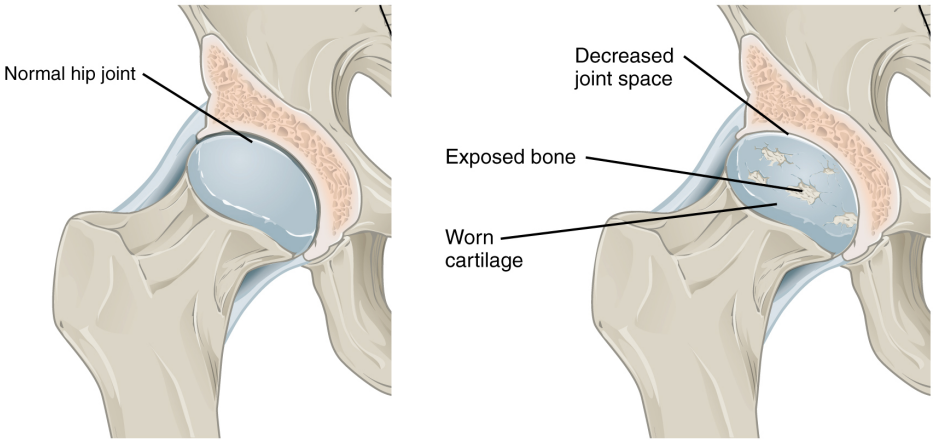

Figure 2.3: Left picture: healty hip; right picture: hip with osteoarthritis [© OpenStax, 2016]

misalignment [Felson, 1988]. Conservative treatment of a painful hip is not yet possible apart from preventive measures to reduce risk factors such as weight or pain [Lühmann et al., 2000]. In hip replacement we can further subdivide treatment by fixation of the implant in *cemented* and *uncemented* hip replacement surgery, neglecting *hybrid* approaches here. Which method is superior is still an ongoing topic in medical research [Abdulkarim et al., 2013], but it can be stated that cemented implants were mostly revised due to aseptic loosening, while the major causes for revision in uncemented implants were infection and dislocation [Abdulkarim et al., 2013, Tyson et al., 2019]. Furthermore, it can be stated that cemented hip prostheses are more likely to outperform uncemented prostheses in elderly patients (>60 years). In contrast, the opposite seems to be true for younger patients [Zhang et al., 2017]. In figure 2.4 an X-ray picture of the hip region after THA with an uncemented prosthesis can be seen. In THA,

Figure 2.4: X-ray of hip region after THA [© Monfils, 2011]

it can be distinguished between primary stability, which should be achieved immediately after surgery, secondary stability, which is usually established in a period of several weeks or months, and long-term stability, which determines the overall durability of the prosthesis. In cemented hip prostheses, primary and secondary stability is achieved collectively when the cement has hardened. In uncemented hip prostheses, primary stability is achieved through a press-fit of the prosthesis within the femur, which has to be established during surgery. Secondary stability is achieved through *osseointegration*, a process where bone substance grows into the roughened surface of the prosthesis. In order for this to proceed properly, primary stability is required [Parithimarkalaignan and Padmanabhan, 2013]. The process of osseointegration is discussed briefly in section 2.4.
The overall objective in most THAs performed is to retain physiological conditions within the hip region despite the presence of the implanted prosthesis. An important aspect here is prosthesis selection and positioning, which can, for example, directly affect the angle of the femoral head and acetabulum. Any change in that angle will result in a shift of the femoral offset and therefore results in an adaption of hip joint reaction forces [Van Houcke et al., 2017]. The latter and the prosthesis itself, which is much stiffer than the surrounding bone, can reduce long-term stability significantly since the bone is subject to *bone remodeling*.

2.3 Biomechanics of bone

Bone can be represented as a calcified composite tissue that exhibits a complex hierarchical structure. The extracellular matrix consists of organic as well as inorganic components. The

organic part consists mainly of collagen, while the inorganic part consists primarily of hydroxyapatite [Feng, 2009]. The third major part is water. On the macroscopic level, bone can be subdivided into compact and cancellous bone. Compact or cortical bone forms the exterior layer of the skeleton, is much more dense and stiffer than cancellous bone, and accounts for approximately 80% of the total bone mass in an adult's skeleton. Cancellous bone, also known as spongy or trabecular bone, forms the internal tissue of the skeleton, is more flexible compared with cortical bone, and consists of an open-cell porous network [cf. Ott, 2018]. The hierarchical structure will not be discussed here, and instead, reference will be made to Reznikov et al. [2014]. Many attempts have been carried out to describe bone as an anisotropic composite material, first, as a two-phase composite with different volume fractions of collagen and hydroxyapatite [Katz, 1971, Currey, 1969]. Later, more sophisticated attempts were made, such as bone modeled as a platelet reinforced composite [Wagner and Weiner, 1992], or by the inclusion of the hierarchical structure of bone, first proposed by Katz [1980] including two hierarchical layers, or following in Porter [2004] as a multi-scale model representing bone as a natural hybrid nano-composite. A more comprehensive review of material modeling of bone can be found in Mellon and Tanner [2012]. However, it can be stated that if bone remodeling is addressed, to date, no material model is available significantly outperforming a simple macroscopic constitutive modeling approach with a phenomenological isotropic material law [Peng et al., 2006, Baca et al., 2008, Yosibash et al., 2010], directly connecting bone mineral density and Young's modulus [see, e.g. Haba et al., 2012, Nobakhti and Shefelbine, 2018]. Furthermore, it can be stated that there is consensus in the scientific community that the small strain assumption is sufficient to describe bone in a structural mechanics approach [cf. Hegedus and Cowin, 1976, Cowin and Doty, 2007, Viceconti, 2012, Currey, 2014] since it seldomly experiences strain above 0.4%.

Bone remodeling. Julius Wolff was among the first to postulate a direct relation between the structure of a bone and the load under which it is placed. This is referred to as *Wolffs law* [Wolff, 1892]. Willhelm Roux did a similar postulate by observations in his theory of *functional adaption* [Roux, 1881]. Pauwels did further refinement to Wolffs law [Pauwels, 1965] and was the first to cross the line of pure research and applied knowledge obtained from biomechanical considerations in clinical routine, e.g. the introduction of tension flanges for the treatment of bone fractures [cf. Regling, 2011]. In the following, many more researchers contributed to the theory of bone remodeling or experimental validation thereof, including Frost [1960] and Moffett Jr et al. [1964], for example. To conclude this historical outline, Cowin and Hegedus [1976] should be stated as the first to provide a closed mathematical description of bone remodeling.
From a biochemical point of view, four types of cells control bone metabolism: osteoblasts, osteoclasts, osteocytes, and bone lining cells. For more information on cellular mechanisms of bone remodeling the reader is referred to Eriksen [2010] or Mellon and Tanner [2012].
To outline the basic ideas shared by most researchers, bone can be considered self-adapting to some functional stimulus related to local stresses and strains. This process of self-adaption can be displayed as an optimization process where bone is a least-weight structure with respect to the mechanical loading [cf. American Society of Mechanical Engineers, 2001, Reiter, 1996, Wolff, 1892, Pauwels, 1965, Reiter, 1995].

2.4 Osseointegration

In cementless THA, most prostheses are equipped with a coated area, whereby the coating consists of bioinert or bioactive material with a surface configuration that is attractive for bone deposition [Schenk and Buser, 1998]. The success of cementless THA, which is the achievement of secondary stability, is determined by the biomechanical properties of the bone-implant interface [Gao et al., 2019]. The evolution of the mechanical properties of the bone-implant interface

as a function of healing time, also referred to as osseointegration, were first described by Branemark [1977]. The term osseointegration can be further specified by the process of bony ingrowth of bone substance into this roughened surface and was characterized as “a direct structural and functional connection between ordered, living bone and the surface of a load-bearing implant” by Listgarten et al. [1991]. Prerequisite for osseointegration is precise fitting of the implant, primary stability, and adequate loading during the healing process [Schenk and Buser, 1998].
In a broadly simplified representation, osseointegration can be subdivided into (1) formation of woven bone at the bone-implant interface and (2) remodeling of woven bone to mature bone [cf. Gao et al., 2019, Schenk and Buser, 1998]. Precise information on the duration of each individual process is difficult to find; however, in the first 4-6 weeks, the formation of woven bone seems to be dominant at the interface, while bone remodeling starts around the third month after the surgery with a peak in process speed around the fourth month [Schenk and Buser, 1998, Haga et al., 2009]. Afterward, the speed of the process slows down, but bone remodeling at the interface continues for the rest of life and is a prerequisite for the bone-implant interface to remain stable as the cells within the interface are renewed by this process [Schenk and Buser, 1998].
Finally, it can be stated that low amplitude micromotions at the bone-implant interface stimulate osseointegration [Mori and Burr, 1993, Szmukler-Moncler et al., 1998], while high amplitude micromotions result in the formation of fibrous tissue [Duyck et al., 2006].

Chapter 3

Continuum mechanics fundamentals

Continuum mechanics is a mathematical framework for studying the transmission of force through and deformation of materials of all types [Klausner, 2012]. In the following chapter, the continuum mechanical relations and formulas are stated as far as it is needed for the rest of this thesis. In chapter 3.1-3.3, the kinematics of bodies in $\mathbb{R}^3$ and all necessary measures for stress and strain for the *infinitesimal strain theory* are derived. In chapter 3.4, balance laws for *open systems* are outlined. Finally, in chapter 3.5, constitutive equations for bone remodeling are provided. This ultimately results in a closed set of governing equations describing thermodynamically consistent bone remodeling.
An attempt has been made to use a notation that is familiar to most readers; however, in case of ambiguity, reference is made to chapter 13, where symbols and the syntax of operations acting on vectors and tensors are introduced.

3.1 Kinematics

In order to describe the deformation of a continuum body, we assume the existence of a stress-free *reference configuration* $\mathcal{B}_0$. The deformation can then be measured by a function $\varphi_t : \mathcal{B}_0 \to \mathcal{B}_t$, which maps $\mathcal{B}_0$ to a *current configuration* $\mathcal{B}_t$ (see figure 3.1). Consequently, a particle $\boldsymbol{x} \in \mathcal{B}_t$

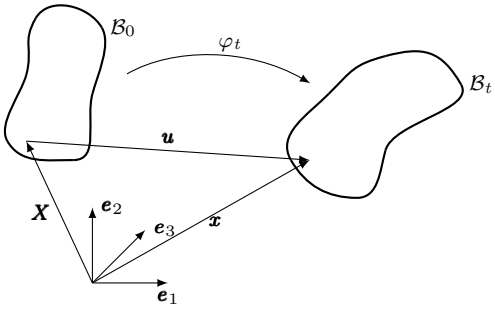

Figure 3.1: Reference body $\mathcal{B}_0$ and deformed body $\mathcal{B}_t$

can be described with the help of its initial position $\boldsymbol{X}$ by $\boldsymbol{x} := \boldsymbol{x}(\boldsymbol{X}, t) = \varphi(\boldsymbol{X}, t)$. That allows for the definition of a *displacement vector* $\boldsymbol{u}$ as

$$\boldsymbol{u}(\boldsymbol{X}, t) = \boldsymbol{x}(\boldsymbol{X}, t) - \boldsymbol{X} \,. \tag{3.1}$$

Alternatively, the inverse map $\varphi^{-1} : \mathcal{B}_t \to \mathcal{B}_0$ can be used to define

$$\tilde{\boldsymbol{u}}(\boldsymbol{x}, t) = \boldsymbol{x} - \boldsymbol{X}(\boldsymbol{x}, t)\,. \tag{3.2}$$

Throughout this thesis, the assumption is made that $\boldsymbol{u}$ itself and derivations of $\boldsymbol{u}$ are **small**, that is

$$O(\boldsymbol{\varepsilon}) = \left|\frac{\partial u_i}{\partial X_j}\right| \ll 1\,. \tag{3.3}$$

Rearranging (3.1) and differentiating with respect to $\boldsymbol{x}$ yields

$$\frac{\partial X_i}{\partial x_j} = \delta_{ij} - \frac{\partial u_i}{\partial x_j}\,. \tag{3.4}$$

The partial derivative $\partial u_i/\partial x_j$ can be expanded by $\partial X_k/\partial X_k$, providing for a recursive definition of $\partial X_i/\partial x_j$ as

$$\frac{\partial X_i}{\partial x_j} = \delta_{ij} - \frac{\partial u_i}{\partial X_k}\frac{\partial X_k}{\partial x_j} \tag{3.5}$$

$$\frac{\partial X_i}{\partial x_j} = \delta_{ij} - \frac{\partial u_i}{\partial X_k}\left(\delta_{kj} - \frac{\partial u_k}{\partial X_l}\left(\delta_{lj} - \cdots\right)\right)\,. \tag{3.6}$$

Since $\partial u_i/\partial X_j$ is small, higher order derivatives $\partial^n u_i/\partial {X_j}^n$ with $n > 1$ are negligible resulting in

$$\frac{\partial X_i}{\partial x_j} \approx \delta_{ij} - \frac{\partial u_i}{\partial X_j}\,. \tag{3.7}$$

Using the above and the relation $\varphi_t \circ \varphi_t^{-1} = \mathrm{Id.} \Leftrightarrow \tilde{\boldsymbol{u}}(\boldsymbol{x}, t) = \boldsymbol{u}(\boldsymbol{X}, t)$, it can be shown that for the small strain case, it isn't necessary to distinguish between reference and current configuration

$$\frac{\partial \tilde{u}_i}{\partial x_j} = \frac{\partial u_i}{\partial X_k}\frac{\partial X_k}{\partial x_j} \approx \frac{\partial u_i}{\partial X_k}\left(\delta_{kj} - \frac{\partial u_k}{\partial X_j}\right) \approx \frac{\partial u_i}{\partial X_j} \tag{3.8}$$

if derivations of $\boldsymbol{u}$ are derived.

3.1.1 Deformation gradient F

In order to derive the *deformation gradient* $\mathbf{F}$, the deformation of an infinitesimal material line element $\mathrm{d}\boldsymbol{X}$ is considered first. Therefore it is convenient to re-write relation (3.1) for a material point $\boldsymbol{X}$ and its infinitesimal surrounding $\mathrm{d}\boldsymbol{X}$ as

$$\boldsymbol{x} + \mathrm{d}\boldsymbol{x} = \boldsymbol{X} + \mathrm{d}\boldsymbol{X} + \boldsymbol{u}(\boldsymbol{X} + \mathrm{d}\boldsymbol{X})\,, \tag{3.9}$$

or in component form as

$$x_i + \mathrm{d}x_i = X_i + \mathrm{d}X_i + u_i(\boldsymbol{X} + \mathrm{d}\boldsymbol{X})\,. \tag{3.10}$$

The term $u_i(\boldsymbol{X} + \mathrm{d}\boldsymbol{X})$ can be expanded by a Taylor series

$$u_i(\boldsymbol{X} + \mathrm{d}\boldsymbol{X}) \approx u_i(\boldsymbol{X}) + \frac{\partial u_i}{\partial X_j}\mathrm{d}X_j\,, \tag{3.11}$$

which is truncated after the partial derivative of order one, yielding the expression

$$x_i + \mathrm{d}x_i = X_i + \mathrm{d}X_i + u_i(\boldsymbol{X}) + \frac{\partial u_i}{\partial X_j}\mathrm{d}X_j \,. \tag{3.12}$$

Now we can simply deduct the relation (3.1) in component form $x_i = X_i + u_i(\boldsymbol{X})$ from the latter equation and finally obtain

$$\mathrm{d}x_i = \mathrm{d}X_i + \frac{\partial u_i}{\partial X_j}\mathrm{d}X_j \,, \tag{3.13}$$

the transformation of an infinitesimal line element component $\mathrm{d}X_i$ in the reference configuration to $\mathrm{d}x_i$ in the current configuration. By re-writing this equation as

$$\mathrm{d}x_i = \left(\delta_{ij} + \frac{\partial u_i}{\partial X_j}\right)\mathrm{d}X_j \,, \tag{3.14}$$

it is possible to identify the deformation gradient as

$$\mathbf{F} = \mathrm{F}_{ij}\,\boldsymbol{e}_i \otimes \boldsymbol{e}_j \quad \text{with} \quad \mathrm{F}_{ij} = \frac{\partial x_i}{\partial X_j} = \delta_{ij} + \frac{\partial u_i}{\partial X_j}, \tag{3.15}$$

illustrating that a line element $\mathrm{d}\boldsymbol{X}$ gets transformed to the deformed current configuration by the deformation gradient:

$$\mathrm{d}x_i = \mathrm{F}_{ij}\mathrm{d}X_j \quad \rightarrow \quad \mathrm{d}\boldsymbol{x} = \mathbf{F}\mathrm{d}\boldsymbol{X} \,. \tag{3.16}$$

3.1.2 Green-Lagrange strain tensor E

In order to derive the Green-Lagrange strain tensor $\mathbf{E}$, we start with the squared length $(\mathrm{d}\boldsymbol{x})^2 = \mathrm{d}x_i \cdot \mathrm{d}x_i$ of an infinitesimal line segment. Inserting (3.14) yields

$$(\mathrm{d}\boldsymbol{x})^2 = \left(\delta_{ij} + \frac{\partial u_i}{\partial X_j}\right)\mathrm{d}X_j \left(\delta_{ik} + \frac{\partial u_i}{\partial X_k}\right)\mathrm{d}X_k \,. \tag{3.17}$$

After some algebraic manipulations, the latter equation can be written as [see e.g. Singh, 2007]

$$(\mathrm{d}\boldsymbol{x})^2 = \left(\delta_{jk} + \frac{\partial u_k}{\partial X_j} + \frac{\partial u_j}{\partial X_k} + \frac{\partial u_i}{\partial X_j}\frac{\partial u_i}{\partial X_k}\right)\mathrm{d}X_j\mathrm{d}X_k \,. \tag{3.18}$$

As a next step, the difference of the squared length of an infinitesimal line segment $\mathrm{d}\boldsymbol{x}$ in the current configuration and $\mathrm{d}\boldsymbol{X}$ in the reference configuration is derived:

$$(\mathrm{d}\boldsymbol{x})^2 - (\mathrm{d}\boldsymbol{X})^2 = \left(\delta_{jk} + \frac{\partial u_k}{\partial X_j} + \frac{\partial u_j}{\partial X_k} + \frac{\partial u_i}{\partial X_j}\frac{\partial u_i}{\partial X_k}\right)\mathrm{d}X_j\mathrm{d}X_k - \mathrm{d}X_j\mathrm{d}X_j \,. \tag{3.19}$$

By the identity $\mathrm{d}X_j\mathrm{d}X_j = \delta_{jk}\mathrm{d}X_j\mathrm{d}X_k$, it is easy to see that following simplification holds true:

$$(\mathrm{d}\boldsymbol{x})^2 - (\mathrm{d}\boldsymbol{X})^2 = \left(\frac{\partial u_k}{\partial X_j} + \frac{\partial u_j}{\partial X_k} + \frac{\partial u_i}{\partial X_j}\frac{\partial u_i}{\partial X_k}\right)\mathrm{d}X_j\mathrm{d}X_k \,. \tag{3.20}$$

In the latter equation the components of the Green-Lagrange strain tensor can be identified by

$$(\mathrm{d}\boldsymbol{x})^2 - (\mathrm{d}\boldsymbol{X})^2 = 2\mathrm{E}_{jk}\mathrm{d}X_j\mathrm{d}X_k \quad \text{with} \quad \mathrm{E}_{jk} = \frac{1}{2}\left(\frac{\partial u_k}{\partial X_j} + \frac{\partial u_j}{\partial X_k} + \frac{\partial u_i}{\partial X_j}\frac{\partial u_i}{\partial X_k}\right) . \tag{3.21}$$

Here the multiplication factor $1/2$ has been introduced artificially for the components of the tensor to match the definition of the Green strain $1/2(\lambda - 1)$.

3.1.3 Linearization of Green-Lagrange strain

For the linearized version $\boldsymbol{\varepsilon}$ of the Green-Lagrange strain tensor, the term $(\partial u_i/\partial X_j)(\partial u_i/\partial X_k)$ in equation (3.21) is assumed to be negligible, resulting in the small strain tensor

$$\varepsilon_{jk} = \frac{1}{2}\left(\frac{\partial u_k}{\partial X_j} + \frac{\partial u_j}{\partial X_k}\right). \tag{3.22}$$

As a note, it is stated that the components of the strain tensor fulfill compatibility equations of the form

$$\frac{\partial^2 \varepsilon_{ij}}{\partial X_k \partial X_m} + \frac{\partial^2 \varepsilon_{km}}{\partial X_i \partial X_j} + \frac{\partial^2 \varepsilon_{ik}}{\partial X_j \partial X_m} + \frac{\partial^2 \varepsilon_{jm}}{\partial X_i \partial X_k} = 0\,. \tag{3.23}$$

For more information, the reader is referred to Slaughter [2012], for example.

3.2 Stress vector

In general, there are two different kinds of forces acting on continuum bodies; *body forces* and *surface forces*. Here, only surface forces should be considered as they give rise to the Cauchy stress tensor defined in the following chapter.

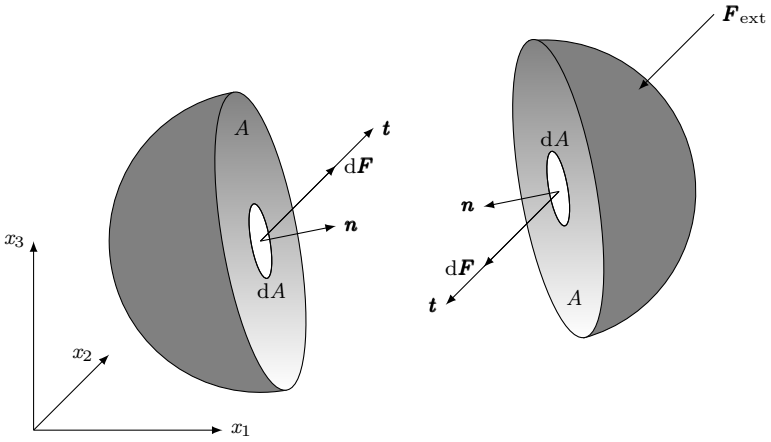

Figure 3.2: A body $\mathcal{B}_t$ subject to external load $\boldsymbol{F}_{\text{ext}}$.

Let $\mathcal{B}_t$ be a continuum body subject to an external load $\boldsymbol{F}_{\text{ext}}$, as shown in figure 3.2. The *stress vector* $\boldsymbol{t}$, also called *traction* or *traction vector*, is defined as the limit value

$$t_i(\boldsymbol{n}) = \lim_{A \to 0} \frac{F_i}{A(\boldsymbol{n})} = \frac{\mathrm{d}F_i}{\mathrm{d}A(\boldsymbol{n})} \tag{3.24}$$

of the force $\mathrm{d}\boldsymbol{F}$ acting onto the dividing surface area $\mathrm{d}A$, defined by surface normal $\boldsymbol{n}$.

3.3 Cauchy stress tensor

For a one-dimensional load case, the stress σ is defined as the fraction of the force F and the cross-sectional area A, which coincides with the definition of the surface tractions. An illustration of an *uniaxial* stress state is given in figure 3.3. For an arbitrary point P within

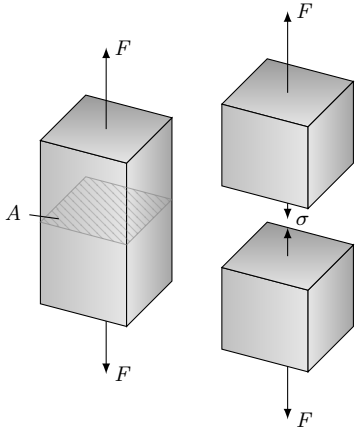

Figure 3.3: Infinitesimal volume element under uniaxial stress.

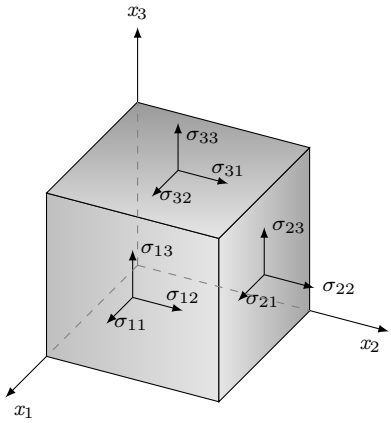

Figure 3.4: Stress components of an arbitrary combined stress state.

a deformed continuum body in three dimensions, the general stress state, that is a *triaxial* stress state, can be defined by *all* existing traction vectors, each acting onto one of the infinite number of planes passing through P. *Cauchy's theorem* shows [see, e.g. Hjelmstad, 2007] that the complete stress state is known if the traction vectors of three mutually perpendicular planes passing through P are known. All other traction vectors can be found by means of coordinate transformation. A convenient choice is the three planes defined by the normal vectors $\boldsymbol{n}_i = \boldsymbol{e}_i$ with $i = 1, 2, 3$, resulting in three traction vectors

$$\boldsymbol{t}(\boldsymbol{e}_1) = t_1(\boldsymbol{e}_1)\boldsymbol{e}_1 + t_2(\boldsymbol{e}_1)\boldsymbol{e}_2 + t_3(\boldsymbol{e}_1)\boldsymbol{e}_3 = \sigma_{11}\boldsymbol{e}_1 + \sigma_{12}\boldsymbol{e}_2 + \sigma_{13}\boldsymbol{e}_3\,, \tag{3.25}$$

$$\boldsymbol{t}(\boldsymbol{e}_2) = t_1(\boldsymbol{e}_2)\boldsymbol{e}_1 + t_2(\boldsymbol{e}_2)\boldsymbol{e}_2 + t_3(\boldsymbol{e}_2)\boldsymbol{e}_3 = \sigma_{21}\boldsymbol{e}_1 + \sigma_{22}\boldsymbol{e}_2 + \sigma_{23}\boldsymbol{e}_3\,, \text{ and} \tag{3.26}$$

$$\boldsymbol{t}(\boldsymbol{e}_3) = t_1(\boldsymbol{e}_3)\boldsymbol{e}_1 + t_2(\boldsymbol{e}_3)\boldsymbol{e}_2 + t_3(\boldsymbol{e}_3)\boldsymbol{e}_3 = \sigma_{31}\boldsymbol{e}_1 + \sigma_{32}\boldsymbol{e}_2 + \sigma_{33}\boldsymbol{e}_3\,, \tag{3.27}$$

from which the components of $\boldsymbol{\sigma}$ are known. An illustration of the stress components of an infinitesimal volume element is given in figure 3.4. Cauchy's theorem generalizes the above by stating that the traction $\boldsymbol{t}(\boldsymbol{n})$ is a linear function of $\boldsymbol{n}$ and there exists a second order tensor $\boldsymbol{\sigma}$ independent of $\boldsymbol{n}$, such that

$$\boldsymbol{t}(\boldsymbol{n}) = \boldsymbol{\sigma}^{\mathrm{T}} \cdot \boldsymbol{n} \quad \Leftrightarrow \quad t_j(\boldsymbol{n}) = \sigma_{ij}\, n_i \tag{3.28}$$

holds. Usually, the above is stated as $\boldsymbol{t}(\boldsymbol{n}) = \boldsymbol{\sigma} \cdot \boldsymbol{n}$ since the stress tensor is symmetric, which follows from the balance of angular momentum (c.f. chapter 3.4.3).

3.4 Balance laws

To derive *conservation laws* or, more generally, *balance laws* in continuum mechanics, we classically start with the assumption of a thermodynamically *closed* system that does not transfer mass with its surroundings. However, this isn't a valid assumption for biomechanical systems as matter and energy can vary throughout a biological process like bone remodeling, and therefore matter and energy needs to be exchanged with the environment. Consequently, biomechanical systems fall within the class of *thermodynamically open systems* as first described as a continuum approach in Cowin and Hegedus [1976], named *the theory of adaptive elasticity.* Subsequently, many other models were based on the incorporation of an additional *mass source* into the common set of balance equations, see e.g. Beaupré et al. [1990b], Weinans et al. [1992], or Harrigan and Hamilton [1992]. More comprehensive approaches to *open system continuum thermodynamics* were provided by Epstein and Maugin [2000], Kuhl and Steinmann [2003], or Kuhl [2004], for example. Balance equations enhanced by mass sources and mass fluxes are described herein, ultimately resulting in a set of constitutive equations for biomechanical tissue. In the following, the works mentioned above will be used as a basis to re-state all necessary balance laws in their *mass-specific* version, which is beneficial in the modeling of growth, as stated in Kuhl et al. [2003].

3.4.1 Balance of mass

The local version of the balance of mass for open systems can be stated

$$\mathrm{D}_t \varrho = \mathfrak{R} \tag{3.29}$$

as the equality of the rate of chance of the spatial mass density ϱ and a mass source $\mathfrak{R}$, which is left to be defined in section 3.5.2. As mentioned before, many other bone tissue models with a balance of mass of type (3.29) can be found in the literature by, amongst others, Beaupré et al. [1990b], Weinans et al. [1992], or Harrigan and Hamilton [1992]. The incorporation of a mass flux into the balance of mass, as shown in Kuhl and Steinmann [2003], is omitted here. In doing so, the resulting set of governing equations would require a numerical discretization scheme, the solution of which would be much more costly. To the author, this additional expenditure does not seem to be justified since, for bone remodeling, both approaches lead to the same basic results, as shown in Kuhl et al. [2003].

3.4.2 Balance of linear momentum

The total linear momentum of a continuum body is defined by

$$\boldsymbol{L} = \int_{\mathcal{B}} \varrho \boldsymbol{v} \, \mathrm{d}v \, . \tag{3.30}$$

In 1776, Euler stated that for a continuum body, or equally a portion of a continuum body, within a closed system, *the rate of change of linear momentum is equal to the total applied force* in any inertial frame, which is known as the *principle of linear momentum.* Starting with the above, the volume-specific version of the local balance of linear momentum for an *open* system can be derived as

$$\mathrm{D}_t(\varrho \boldsymbol{v}) = \mathrm{Div}(\boldsymbol{\sigma}) + \varrho \boldsymbol{b} + \boldsymbol{v}\mathfrak{R} \, , \tag{3.31}$$

where $\boldsymbol{v}$ is the spatial velocity, $\boldsymbol{\sigma}$ is the Cauchy stress tensor, also referred to as *momentum flux*, $\boldsymbol{b}$ are volume forces, also referred to as *momentum sources*, and $\boldsymbol{v}\mathfrak{R}$ is the momentum carried by the mass entering or leaving the open system. It is noted, that detailed derivations can be

found in most basic continuum mechanic books [see e.g. Basar and Weichert, 2013]. Inserting the time-derivative $\mathrm{D}_t(\varrho \boldsymbol{v}) = \varrho \mathrm{D}_t \boldsymbol{v} + \boldsymbol{v} \mathrm{D}_t \varrho$ into (3.31) yields:

$$\varrho \mathrm{D}_t \boldsymbol{v} + \boldsymbol{v} \mathrm{D}_t \varrho = \mathrm{Div}(\boldsymbol{\sigma}) + \varrho \boldsymbol{b} + \boldsymbol{v} \mathfrak{R} \,. \tag{3.32}$$

It is then possible to deduct the velocity-weighted version of the mass balance

$$\boldsymbol{v}\, \mathrm{D}_t \varrho = \boldsymbol{v}\, \mathfrak{R} \tag{3.33}$$

from (3.32) and the result is the mass-specific version of the momentum balance

$$\varrho \mathrm{D}_t \boldsymbol{v} = \mathrm{Div}(\boldsymbol{\sigma}) + \varrho \boldsymbol{b} \,, \tag{3.34}$$

as shown in Kuhl [2004], for example. In the following, the restriction to the the quasi-static case ($\mathrm{D}_t \boldsymbol{v} = \boldsymbol{0}$) and the omission of body forces ($\boldsymbol{b} = \boldsymbol{0}$) is assumed.

3.4.3 Balance of angular momentum

The angular momentum

$$\boldsymbol{H} = \int_{\mathcal{B}} \boldsymbol{a} \times (\varrho \boldsymbol{v}) \, \mathrm{d}v \tag{3.35}$$

is defined by the cross-product of a position vector $\boldsymbol{a} \in \mathcal{B}$ and the momentum density $\varrho \boldsymbol{v}$. According to Kuhl et al. [2003], the mass-specific version of the local balance of angular momentum then follows simply from the cross product of the mass-specific version of the balance of linear momentum (3.34) and the position vector $\mathbf{a}$ as

$$\boldsymbol{a} \times \mathrm{Div}\, \boldsymbol{\sigma} = \boldsymbol{0} \,. \tag{3.36}$$

By the use of the balance of angular momentum, the symmetry of the Cauchy stress tensor can be derived. However, this is omitted here and instead reference is made to Basar and Weichert [2013], where a detailed derivation can be found.

3.4.4 Balance of internal energy

According to Malvern [1965], the volume-specific balance of energy states that the rate of change of energy

$$\mathrm{D}_t(\varrho E) = \mathrm{D}_t(\varrho K + \varrho U) = P^{\mathrm{ext}} + Q \tag{3.37}$$

is equal to the sum of the external mechanical power input P^{ext} and the non-mechanical input Q. The total energy $E = K + U$ can be displayed as the sum of the *kinetic energy* K and the *internal energy* U. The balance of kinetic energy can be stated as the rate of change of kinetic energy

$$\mathrm{D}_t(\varrho K) = P^{\mathrm{ext}} - P^{\mathrm{int}} \tag{3.38}$$

is equal to the difference of external and internal power. Deducting equation (3.38) from equation (3.37) provides the balance of internal energy as

$$\mathrm{D}_t(\varrho U) = P^{\mathrm{int}} + Q \,. \tag{3.39}$$

The internal power

$$P^{\mathrm{int}} = \boldsymbol{\sigma} : \mathrm{D}_t \boldsymbol{\varepsilon} \tag{3.40}$$

is defined by the *stress power*, which for small strain elasticity is defined by the the double contraction of the cauchy stress tensor $\boldsymbol{\sigma}$ and the linearized strain rate $\mathrm{D}_t\boldsymbol{\varepsilon}$ [Hjelmstad, 2007]. For systems with non-constant mass, the non-mechanical input

$$Q = \mathrm{Div}\,(-\boldsymbol{Q}) + \mathcal{Q} + U\mathfrak{R} \tag{3.41}$$

can be defined as the divergence of a heat flux $\boldsymbol{Q}$, a heat source $\mathcal{Q}$, and an energy source $U\mathfrak{R}$ due to the changing mass. Since heat is not assumed to be generated for bone remodeling, the heat flux ($\boldsymbol{Q} = \boldsymbol{0}$) and the heat source ($\mathcal{Q} = 0$) both vanish identically. Inserting (3.40) and (3.41) into (3.39) yields

$$\mathrm{D}_t(\varrho U) = \boldsymbol{\sigma} : \mathrm{D}_t\boldsymbol{\varepsilon} + U\mathfrak{R} \tag{3.42}$$

the volume-specific version of the balance of internal energy for open continuum systems in the regime of small deformations with changing mass but without mass flux. For the mass-specific version of the balance of internal energy, an energy-weighted version of the balance of mass

$$U\mathrm{D}_t\varrho = U\mathfrak{R} \tag{3.43}$$

is deducted from (3.42), resulting in

$$\varrho\,\mathrm{D}_t U = \boldsymbol{\sigma} : \mathrm{D}_t\boldsymbol{\varepsilon} \tag{3.44}$$

the mass-specific version of the balance of internal energy [cf. Kuhl and Steinmann, 2003].

3.4.5 Dissipation inequality

Respecting the non-constant mass in an open system results in an additional *entropy source* $\mathcal{S}$, as shown in Schrödinger [1944], Malvern [1965], or Epstein and Maugin [2000], for example. Against this background, Kuhl and Steinmann [2003] provided a free-energy density-based version of the *Clausius-Duhem* inequality for open systems of the form

$$\boldsymbol{\sigma} : \mathrm{D}_t\boldsymbol{\varepsilon} - \varrho\mathrm{D}_t\psi - \varrho(S + \mathrm{D}_\theta\psi)\mathrm{D}_t\theta - \mathcal{S}\theta - \boldsymbol{Q}\cdot\nabla_{\boldsymbol{X}}\ln\theta \geq 0\,, \tag{3.45}$$

where ψ is the specific *Helmholtz free energy* function, S is the entropy, and θ is the absolute temperature. The Clausius-Duhem inequality can be decomposed into a local term d^{loc}, typically referred to as *Clausius-Planck inequality*, and a conductive term d^{cond}, typically referred to as *Fourier inequality*. Both terms are required to hold separately:

$$\begin{cases} d^{\mathrm{loc}} = \boldsymbol{\sigma} : \mathrm{D}_t\boldsymbol{\varepsilon} - \varrho\mathrm{D}_t\psi - \varrho(S + \mathrm{D}_\theta\psi)\mathrm{D}_t\theta - \mathcal{S}\theta & \geq 0 \\ d^{\mathrm{con}} = -\boldsymbol{Q}\cdot\nabla_{\boldsymbol{X}}\ln\theta & \geq 0 \end{cases}. \tag{3.46}$$

Here, the assumption is made that all processes in this thesis are modeled as isothermal processes. This is done mainly for three reasons: (1) The temperature in the human body can be assumed as constant, especially for long-term processes. (2) There is little knowledge available of heat transfer and heat production between bone and prosthesis, and (3) in this thesis, the thermal dissipation is assumed to be much smaller than the mechanical dissipation. Due to that assumption, the Clausius-Duhem inequality reduces itself to the local part d^{loc}, since $d^{\mathrm{con}} \geq 0$ holds if $\nabla_{\boldsymbol{X}}\ln\theta = \boldsymbol{0}$.

3.5 Constitutive theory

The kinematic equations and balance laws described above hold for any solid that deforms under external forces. However, they do not form a complete set of governing equations since, for 15 unknowns, that are three displacements, six stresses, and six strains, there are only six kinematic equations and three equilibrium equations from the balance of linear momentum. As a consequence, six additional equations are needed, and these are the material describing *constitutive equations* relating stress to strain.
There is a set of basic principles of material theory, which has to be fulfilled by any constitutive model, for example, the principle of determinism or the principle of objectivity. For a complete description of constitutive modeling, the reader is referred to Ottosen and Ristinmaa [2005] or de Souza Neto et al. [2011].

3.5.1 A thermodynamically consistent constitutive law for bone remodeling

Following de Souza Neto et al. [2011], it will be assumed that the set of *state variables*

$$\{\varrho, \boldsymbol{\varepsilon}\} \tag{3.47}$$

determines the *thermodynamic state* for any time t at a point $\boldsymbol{X} \in \mathcal{B}_0$, where $\boldsymbol{\varepsilon}$ is the linearized strain and ϱ is reinterpreted as the bone mineral density. Consequently, the Helmholtz specific free energy $\psi = \psi(\varrho, \boldsymbol{\varepsilon})$ is dependent on the state variables. The material time derivative then follows as

$$\mathrm{D}_t \psi(\varrho, \boldsymbol{\varepsilon}) = \partial_\varrho \psi \, \mathrm{D}_t \varrho + \partial_{\boldsymbol{\varepsilon}} \psi : \mathrm{D}_t \boldsymbol{\varepsilon} = \partial_\varrho \psi \, \mathfrak{R} + \partial_{\boldsymbol{\varepsilon}} \psi : \mathrm{D}_t \boldsymbol{\varepsilon} \, . \tag{3.48}$$

Inserting the above into the Clausius-Planck inequality $(3.46)_1$ yields

$$d^{\mathrm{loc}} = (\sigma - \varrho \, \partial_{\boldsymbol{\varepsilon}} \psi) : \mathrm{D}_t \, \boldsymbol{\varepsilon} - \varrho \, \partial_\varrho \psi \, \mathfrak{R} - \varrho (S + \mathrm{D}_\theta \psi) \mathrm{D}_t \theta - \mathcal{S} \theta \geq 0 \, , \tag{3.49}$$

from which the constitutive equations

$$\boldsymbol{\sigma} = \varrho \, \partial_{\boldsymbol{\varepsilon}} \, \psi \, , \quad S = -\mathrm{D}_\theta \, \psi \, = 0, \quad \text{and} \quad \mathcal{S} = -\varrho \frac{1}{\theta} \, \partial_\varrho \psi \, \mathfrak{R} \tag{3.50}$$

are implied. By that procedure, the fulfillment of the Clausius-Planck inequality is guaranteed *a priori*. Thus, concluding the above, the thermodynamically consistent constitutive law for isothermal bone remodeling can be stated as

$$\begin{cases} \psi = \psi(\varrho, \boldsymbol{\varepsilon}) \\ \sigma = \varrho \partial_{\boldsymbol{\varepsilon}} \, \psi \\ \mathrm{D}_t \, \varrho = \mathfrak{R} \\ \mathcal{S} = -\varrho \frac{1}{\theta} \, \partial_\varrho \psi \mathfrak{R} \end{cases} . \tag{3.51}$$

Since the constitutive model described above only depends on the history of the linearized strain $\boldsymbol{\varepsilon}$ and bone mineral density, it is possible to define the *constitutive initial value problem*: presuming the history of linearized strain $\boldsymbol{\varepsilon}(t)$, $t \in [t_0, T]$ and the initial value of the bone mineral density $\varrho(t_0)$ are known, find the history of $\boldsymbol{\sigma}(t)$ and $\varrho(t)$, such that the constitutive equations

$$\begin{cases} \boldsymbol{\sigma}(t) = \varrho(t) \, \partial_{\boldsymbol{\varepsilon}} \, \psi(\varrho(t), \boldsymbol{\varepsilon}(t)) \\ \mathrm{D}_t \, \varrho(t) = \mathfrak{R}(\varrho(t), \boldsymbol{\varepsilon}(t)) \end{cases} \tag{3.52}$$

hold for every $t \in [t_{(0)}, T]$ [c.f. de Souza Neto et al., 2011].

3.5.2 Density-weighted generalized Hooke's law

For isothermal processes, the strain energy density function

$$\Psi(\varrho, \boldsymbol{\varepsilon}) = \varrho\, \psi(\varrho, \boldsymbol{\varepsilon}) \tag{3.53}$$

is defined by the product of the bone mineral density ϱ and the specific Helmholtz free energy ψ [see e.g. Wriggers, 2008]. In bone remodeling, a quite common choice for the specific Helmholtz free energy

$$\psi = \left[\frac{\varrho}{\varrho_0}\right]^n \psi^{\mathrm{LE}}, \quad \psi^{\mathrm{LE}} = \frac{1}{\varrho}\left[\frac{\lambda}{2}(\mathrm{tr}(\boldsymbol{\varepsilon}))^2 + \mu \mathrm{tr}(\boldsymbol{\varepsilon}^2)\right] \tag{3.54}$$

is based on a classical linear-elastic-type free energy function ψ^{LE} weighted by a relative density $(\varrho/\varrho_0)^n$, where the exponent n is allowed to vary between $1 \leq n \leq 3.5$, and λ and μ are Lamé constants, as shown in Carter and Hayes [1977], Gibson and Ashby [1982] or Kuhl and Steinmann [2003], for example. This provides a redefinition of the Cauchy stress tensor as the density-weighted Cauchy stress tensor as

$$\boldsymbol{\sigma} = \partial_{\boldsymbol{\varepsilon}} \Psi = \varrho\, \partial_{\boldsymbol{\varepsilon}} \psi = \left[\frac{\varrho}{\varrho_0}\right]^n \boldsymbol{\sigma}^{\mathrm{LE}} = \left[\frac{\varrho}{\varrho_0}\right]^n (\lambda \mathrm{tr}(\boldsymbol{\varepsilon})\mathbf{I} + 2\mu\boldsymbol{\varepsilon}) \,. \tag{3.55}$$

The density-weighted material tensor can then be derived as

$$\mathbb{C} = \partial_{\boldsymbol{\varepsilon}} \boldsymbol{\sigma} = \left[\frac{\varrho}{\varrho_0}\right]^n \mathbb{C}^{\mathrm{LE}} = \left[\frac{\varrho}{\varrho_0}\right]^n (\lambda \mathbf{I} \otimes \mathbf{I} + 2\mu \mathbb{I}) \,. \tag{3.56}$$

Finally, analogous to the generalized Hooke's law for continuous media, the density-weighted generalized Hooke's law can be stated using (3.55), (3.56), and (3.22), as

$$\boldsymbol{\sigma}(\varrho) = \mathbb{C}(\varrho) : \boldsymbol{\varepsilon} \,. \tag{3.57}$$

Chapter 4

Finite element modeling

The finite element method has proven itself particularly useful for efficient analyses of partial differential equations arising in the context of mathematical and engineering problems. Thereby, an approximate numerical solution to a *weak form* of the original problem is found, which is a *weak solution* in the sense of distributions. Weak forms can be constructed by multiplying a partial differential equation with so-called *test functions* from the space of smooth functions with compact support and subsequently integrating the latter over a domain. The existence and uniqueness of the solution of a weak form are established by the help of the famous *Lax-Milgram* theorem [Lax and Milgram, 1954]. The *calculus of variations* is the standard tool for constructing weak forms, and several approaches can be applied in order to find weak forms of different kinds. Applying the *Ritz-Galerkin* method [cf. Ern and Guermond, 2013], or a derivate thereof, to a weak form converts the continuous problem into a discrete problem, the solution of which can be found by solving a set of algebraic equations. The discretized solution is known to be *quasi-optimal*, a result provided by *Céa*'s lemma [Céa, 1964]. The discrete problem is usually defined by a *discretization strategy*, which is a *mesh* assembled of finite elements with associated basis functions. The type of element and the definition of the basis function can be chosen freely, except for requirements arising from the weak form and boundary conditions. This ultimately results in a zoo of finite elements and among them: *Lagrangian* -, *mixed* -, or *discontinuous Galerkin* finite elements, for example. As a note, it is mentioned that the pioneering work of Arnold et al. [2006] assembles all of the above finite elements, and many more, into a unified framework.
In the context of elasticity problems, the standard procedure to construct a weak form is known as the *principle of virtual work*, which is then solved for the coefficients of the finite element interpolation of the displacement field. More information about finite elements and finite element modeling can be found in Zienkiewicz et al. [1977], Bathe [2006], Braess [2013], or Wriggers [2008], for example.

4.1 Weak form

In chapter 3, a closed set of governing equations with respect to the initial configuration of a continuum body $\mathcal{B}_0$ was introduced:

$$\begin{cases} \operatorname{Div}(\boldsymbol{\sigma}) = \mathbf{0} & \text{(Equilibrium equation)}\,, \\ \boldsymbol{\varepsilon} = \frac{1}{2}\left(\operatorname{Grad}(\boldsymbol{u}) + \operatorname{Grad}(\boldsymbol{u})^{\mathrm{T}}\right) & \text{(Kinematic equation)}\,, \\ \boldsymbol{\sigma} = \mathbb{C}(\varrho) : \boldsymbol{\varepsilon} & \text{(Constitutive equation)}\,. \end{cases} \tag{4.1}$$

Furthermore, the existence and uniqueness of a solution [cf. Truesdell et al., 1975] to the *strong form* (4.1) is only guaranteed with a suitable set of *boundary conditions* prescribed on $\partial\mathcal{B}_0$,

namely *Dirichlet* boundary conditions on $\Gamma_u \subseteq \partial\mathcal{B}_0$ and *Neumann* boundary conditions on $\Gamma_\sigma = \partial\mathcal{B}_0 \setminus \Gamma_u$:

$$\boldsymbol{u}(\boldsymbol{X},t) = \bar{\boldsymbol{u}}(\boldsymbol{X}) \quad \forall\, \boldsymbol{X} \in \Gamma_u \quad \text{and} \quad \boldsymbol{t}(\boldsymbol{X},t) = \bar{\boldsymbol{t}}(\boldsymbol{X}) \quad \forall\, \boldsymbol{X} \in \Gamma_\sigma\,. \tag{4.2}$$

Equation (4.2) is equivalent with demanding $\boldsymbol{u}$ to be a *kinematically admissible displacement field* and $\boldsymbol{\sigma}$ to be a *statically admissible stress field* [cf. Truesdell et al., 1975].
A first weak form can be found by multiplying the equilibrium equation $(4.1)_1$ with a test function $\boldsymbol{\eta}$, which is left to be defined in the following and applying integration by parts:

$$\int_{\mathcal{B}_0} \mathrm{Div}(\boldsymbol{\eta}\cdot\boldsymbol{\sigma})\,\mathrm{d}V - \int_{\mathcal{B}_0} \mathrm{Grad}(\boldsymbol{\eta}) : \boldsymbol{\sigma}\,\mathrm{d}V = 0\,. \tag{4.3}$$

As a next step, the *divergence theorem* can be applied to the first term of the above equation, yielding

$$\int_{\Gamma_\sigma} \boldsymbol{\eta}\cdot\boldsymbol{t}\,\mathrm{d}A - \int_{\mathcal{B}_0} \mathrm{Grad}(\boldsymbol{\eta}) : \boldsymbol{\sigma}\,\mathrm{d}V = 0\,, \tag{4.4}$$

where use has been made of the relation $\boldsymbol{\sigma}\cdot\boldsymbol{n} = \boldsymbol{t}$.

Principle of virtual work. Consider a continuum body $\mathcal{B}$ with an arbitrary but kinematically admissible *virtual* displacement field $\delta\boldsymbol{u}$, i.e., the virtual displacements $\delta\boldsymbol{u} = \bar{\boldsymbol{u}}$ satisfy the Dirichlet boundary conditions on Γ_u. The principle of virtual work then states that for all possible virtual displacements $\delta\boldsymbol{u}$, the *virtual work* $\delta\Pi = \delta U - \delta W$ vanishes if and only if the body is in static equilibrium. Hereby, δU is called *internal virtual work* and δW *external virtual work*.

The principle of virtual work, also called the principle of virtual displacements, can be used to specify the test function as $\boldsymbol{\eta} = \delta\boldsymbol{u}$. Consequently, $\mathrm{Grad}(\boldsymbol{\eta}) = \delta\boldsymbol{\varepsilon}$ can be identified from the kinematic equation $(4.1)_2$ as *virtual strain* and

$$\delta U = \int_{\mathcal{B}_0} \delta\boldsymbol{\varepsilon} : \boldsymbol{\sigma}\,\mathrm{d}V \quad \text{and} \quad \delta W = \int_{\Gamma_\sigma} \delta\boldsymbol{u}\cdot\boldsymbol{t}\,\mathrm{d}A \tag{4.5}$$

can be identified as *virtual internal work* and *virtual external work*, respectively. As a last step, the constitutive equation $(4.1)_3$ is inserted into the virtual internal work. The resultant weak form can then be stated as follows:

$$\delta\Pi = \delta U - \delta W = \int_{\mathcal{B}_0} \delta\boldsymbol{\varepsilon} : \mathbb{C}(\varrho) : \boldsymbol{\varepsilon}\,\mathrm{d}V - \int_{\Gamma_\sigma} \delta\boldsymbol{u}\cdot\boldsymbol{t}\,\mathrm{d}A = 0\,. \tag{4.6}$$

4.2 Material non-linearities

Presuming a constant material tensor $\mathbb{C}$, the weak form (4.6) is a *linear boundary value problem* which, in a finite element framework, ultimately results in a linear system of algebraic equations. Obviously, the latter does not hold here, since in bone remodeling $\mathbb{C} = \mathbb{C}(\varrho)$ is a density-weighted material tensor (see section 3.5.2). The evolution of the bone mineral density is described by the constitutive initial value problem given in equation (3.52), a constraint that has to be fulfilled

in addition to the weak form. Therefore, the problem becomes a *non-linear initial boundary value problem*:

$$\begin{cases} \delta\Pi(\varrho(t), \boldsymbol{u}(t)) = 0 \\ \Phi(\varrho(t), \boldsymbol{u}(t)) = \mathrm{D}_t\, \varrho(t) - \mathfrak{R}(\varrho(t), \boldsymbol{\varepsilon}(t)) = 0 \end{cases}, \tag{4.7}$$

with the prescribed *history* of Dirichlet boundary conditions

$$\boldsymbol{u}(\boldsymbol{X}, t) = \bar{\boldsymbol{u}}(\boldsymbol{X}, t) \quad \forall \boldsymbol{X} \in \Gamma_u\,, \forall t \in [t_0, T]\,, \tag{4.8}$$

the prescribed *history* of Neumann boundary conditions

$$\boldsymbol{t}(\boldsymbol{X}, t) = \bar{\boldsymbol{t}}(\boldsymbol{X}, t) \quad \forall \boldsymbol{X} \in \Gamma_\sigma\,, \forall t \in [t_0, T]\,, \tag{4.9}$$

and the *initial* internal bone mineral density field

$$\varrho(\boldsymbol{X}, t_0) = \varrho_0(\boldsymbol{X}) \quad \forall \boldsymbol{X} \in \mathcal{B}_0\,. \tag{4.10}$$

In general, the constitutive model is path-dependent, and for the problem (4.7), a closed-form solution is not available. However, choosing a backward Euler numerical integration scheme for the constitutive initial value problem (3.52) results in the definition of an *incremental* constitutive function for the bone mineral density

$$\varrho_{(n+1)} = \varrho_{(n)} + \Delta t \hat{\mathfrak{R}}(\varrho_{(n)}, \boldsymbol{\varepsilon}_{(n+1)}) = \varrho_{(n)} + \Delta\varrho \tag{4.11}$$

with $\Delta t = t_{(n+1)} - t_{(n)}$ and an *incremental* constitutive function for the stress tensor

$$\boldsymbol{\sigma}_{(n+1)} = \hat{\boldsymbol{\sigma}}(\varrho_{(n)}, \boldsymbol{\varepsilon}_{(n+1)}) = \mathbb{C}(\varrho_{(n)} + \Delta\varrho) : \boldsymbol{\varepsilon}_{(n+1)}\,. \tag{4.12}$$

As a next step, the above is reintroduced into the weak form (4.6), resulting in an *incremental* boundary value problem. Because within one time-step the bone mineral density is held constant, we can think of $\delta\Pi_{(n+1)} = \delta\Pi(\boldsymbol{u}_{(n+1)})$ as a function of the unknown displacements $\boldsymbol{u}_{(n+1)}$ alone, which makes the constitutive model *path-independent* within one time-step:

$$\begin{aligned} \delta\Pi_{(n+1)} &= \delta\, U_{(n+1)} - \delta\, W_{(n+1)} \\ &= \int_{\mathcal{B}_0} \delta\boldsymbol{\varepsilon} : \mathbb{C}(\varrho_{(n)} + \Delta\varrho) : \boldsymbol{\varepsilon}_{(n+1)}\, \mathrm{d}\, V - \int_{\Gamma_\sigma} \delta\boldsymbol{u} \cdot \boldsymbol{t}_{(n+1)}\, \mathrm{d}\, A = 0\,. \end{aligned} \tag{4.13}$$

The above equation is non-linear and needs consistent linearization to be solved via a *Newton-Raphson* scheme.

4.3 Linearization

Presuming the displacement field $\boldsymbol{u}_{(n)}$ is known, and $\delta\Pi$ is sufficiently smooth in t, an expression for the unknown virtual work

$$\delta\Pi_{(n+1)} = \delta\Pi(\boldsymbol{u}_{(n+1)}) = \delta\Pi(\boldsymbol{u}_{(n)} + \Delta\boldsymbol{u}) \tag{4.14}$$

can be derived at time-step $t_{(n+1)} = t_{(n)} + \Delta t$ with $\boldsymbol{u}_{(n+1)} = \boldsymbol{u}_{(n)} + \Delta\boldsymbol{u}$ and $\boldsymbol{t}_{(n+1)} = \boldsymbol{t}_{(n)} + \Delta\boldsymbol{t}$ by truncating a *Taylor series expansion*

$$\delta\Pi(\boldsymbol{u}_{(n)} + \Delta\boldsymbol{u}) \approx \delta\Pi(\varrho_{(n)}, \boldsymbol{u}_{(n)}) + \Delta(\delta\Pi(\varrho_{(n)}, \boldsymbol{u}_{(n)}, \Delta\boldsymbol{u}))\,. \tag{4.15}$$

Although $\delta\Pi$ only exhibits a variation in $\boldsymbol{u}$, $\delta\Pi$ was written as a function of ϱ and $\boldsymbol{u}$ to indicate the used time-step of each quantity. The same Taylor expansion is applied to the incremental constitutive function which, by defining $\Delta\boldsymbol{\varepsilon} = \mathrm{Grad}(\Delta\boldsymbol{u})$, can be stated as

$$\hat{\boldsymbol{\sigma}}(\varrho_{(n)}, \boldsymbol{\varepsilon}_{(n+1)}) \approx \hat{\boldsymbol{\sigma}}(\varrho_{(n)}, \boldsymbol{\varepsilon}_{(n)}) + \Delta\hat{\boldsymbol{\sigma}}(\varrho_{(n)}, \boldsymbol{\varepsilon}_{(n)}, \Delta\boldsymbol{\varepsilon})\,. \tag{4.16}$$

The variation of the incremental constitutive function can be found by defining the trial strain $\boldsymbol{\varepsilon}^*_{(n+1)} = \boldsymbol{\varepsilon}_{(n)} + \Delta\boldsymbol{\varepsilon}$ and applying the chain rule:

$$\Delta\hat{\boldsymbol{\sigma}}(\varrho_{(n)}, \boldsymbol{\varepsilon}_{(n)}, \Delta\boldsymbol{\varepsilon}) = \left[\left. \frac{\mathbb{C}(\varrho_{(n)} + \Delta\varrho)}{\partial\boldsymbol{\varepsilon}^*_{(n+1)}} \right|_t : \boldsymbol{\varepsilon}^*_{(n+1)} + \mathbb{C}(\varrho_{(n)} + \Delta\varrho) \right] : \Delta\boldsymbol{\varepsilon} \tag{4.17}$$

$$= \bar{\mathbb{C}}_{(n+1)} : \Delta\boldsymbol{\varepsilon}\,, \tag{4.18}$$

where $\bar{\mathbb{C}}$ is the consistent tangent modulus. We can then further define the known principle of virtual work at time-step $t_{(n)}$ as

$$\delta\Pi(\varrho_{(n)}, \boldsymbol{u}_{(n)}) = \delta U_{(n)} - \delta W_{(n)}\,, \tag{4.19}$$

and the variation of the virtual work at time-step $t_{(n)}$ as

$$\Delta(\delta\Pi(\varrho_{(n)}, \boldsymbol{u}_{(n)}, \Delta\boldsymbol{u})) = \Delta\delta U_{(n)} - \Delta\delta W_{(n)}\,. \tag{4.20}$$

In the above, the internal virtual work is defined as

$$\delta U_{(n)} = \int_{\mathcal{B}_0} \delta\boldsymbol{\varepsilon} : \boldsymbol{\sigma}_{(n)}\,\mathrm{d}V = \int_{\mathcal{B}_0} \delta\boldsymbol{\varepsilon} : \hat{\boldsymbol{\sigma}}(\varrho_{(n)}, \boldsymbol{\varepsilon}_{(n)})\,\mathrm{d}V\,, \tag{4.21}$$

the external virtual work as

$$\delta W_{(n)} = \int_{\Gamma_\sigma} \delta\boldsymbol{u} \cdot \boldsymbol{t}_{(n)}\,\mathrm{d}A\,, \tag{4.22}$$

the increment of the internal virtual work as

$$\Delta\delta U_{(n)} = \int_{\mathcal{B}_0} \delta\boldsymbol{\varepsilon} : \bar{\mathbb{C}}_{(n+1)} : \Delta\boldsymbol{\varepsilon}\,\mathrm{d}V\,, \tag{4.23}$$

and the increment of the external virtual work as

$$\Delta\delta W_{(n)} = \int_{\Gamma_\sigma} \delta\boldsymbol{u} \cdot \Delta\boldsymbol{t}\,\mathrm{d}A\,, \tag{4.24}$$

with $\Delta\boldsymbol{t} = \boldsymbol{t}_{(n+1)} - \boldsymbol{t}_{(n)}$. Summarizing all of the above, the resultant linearized weak form can be stated as

$$\int_{\mathcal{B}_0} \delta\boldsymbol{\varepsilon} : \bar{\mathbb{C}}_{(n+1)} : \Delta\boldsymbol{\varepsilon}\,\mathrm{d}V = -\int_{\mathcal{B}_0} \delta\boldsymbol{\varepsilon} : \boldsymbol{\sigma}_{(n)}\,\mathrm{d}V + \int_{\Gamma_\sigma} \delta\boldsymbol{u} \cdot \boldsymbol{t}_{(n+1)}\,\mathrm{d}A\,. \tag{4.25}$$

4.4 Finite element interpolation: the Lagrangian finite element

Let e be a generic finite element, defined by the nodes $\hat{\boldsymbol{x}}^i$, $i = 1, ..., n_{\text{nodes}}$, each node associated with one *shape function* N_i. The shape functions $\{N_i\}_{i=1,...,n_{\text{nodes}}}$ assemble a basis for $\mathcal{B}_e$ by the fulfillment of the *delta property*:

$$N_i(\hat{\boldsymbol{x}}^j) = \delta_{ij} \,. \tag{4.26}$$

Given a generic field $a(\boldsymbol{x})$, defined over $\mathcal{B}_e$, the finite element interpolation $\bar{a}(\boldsymbol{x})$ of $a(\boldsymbol{x})$ is given by

$$a(\boldsymbol{x}) \approx \bar{a}(\boldsymbol{x}) = a(\hat{\boldsymbol{x}}^i) N_i(\boldsymbol{x}) \,. \tag{4.27}$$

4.4.1 The isoparametric concept

Since $\hat{\boldsymbol{x}}^i$ are global coordinate vectors for nodal positions of a generic finite element e, equation (4.26) would have to be solved once for each finite element for all shape function to be known. Instead, we define the shape functions on a *reference element* (see figure 4.1) and consequently

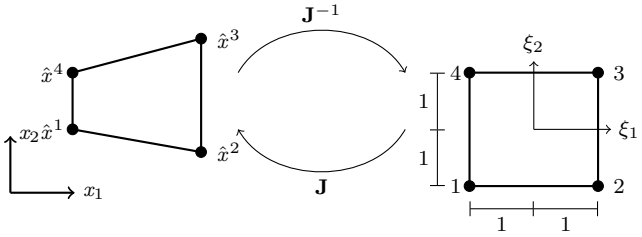

Figure 4.1: Isoparametric mapping to a reference element.

use the shape function for approximating the displacement field as well as the geometry:

$$\boldsymbol{u}(\boldsymbol{\xi}) \approx N_i(\boldsymbol{\xi}) \hat{\boldsymbol{u}}^i \quad \text{and} \quad \boldsymbol{x}(\boldsymbol{\xi}) \approx N_i(\boldsymbol{\xi}) \hat{\boldsymbol{x}}^i \,, \tag{4.28}$$

where $\boldsymbol{\xi}$ is the coordinate system of the reference element and $\hat{\boldsymbol{u}}^i = \boldsymbol{u}(\hat{\boldsymbol{x}}^i)$ is the nodal displacement. Derivatives of the shape functions with respect to global coordinates can be expressed as

$$\frac{\partial N_i}{\partial x_j} = \frac{\partial N_i}{\partial \xi_\alpha} \frac{\partial \xi_\alpha}{\partial x_j} \,, \tag{4.29}$$

and the derivative of global coordinates with respect to the convective coordinates as

$$\frac{\partial x_i}{\partial \xi_j} = \frac{\partial N_\alpha}{\partial \xi_j} \hat{x}_i^\alpha \,. \tag{4.30}$$

The above can be assembled into the *Jacobi* matrix $\mathbf{J}$ and its inverse $\mathbf{J}^{-1}$, with their components given by:

$$J_{ij} = \frac{\partial x_i}{\partial \xi_j} \quad \text{and} \quad J^{-1}_{ji} = \frac{\partial \xi_j}{\partial x_i} \,. \tag{4.31}$$

The Jacobi matrix provides a connection between integration in global coordinates and integration on the reference element defined by the identity

$$\mathrm{d}\,V_{\boldsymbol{x}} = \det\mathbf{J}\,\mathrm{d}\,V_{\boldsymbol{\xi}}\,. \tag{4.32}$$

This approach is usually referred to as the *isoparametric concept*. The finite elements used throughout this thesis are mostly quadratic Lagrangian triangles and quadratic Lagrangian tetrahedrons. For specific examples of shape functions and more information about the finite element interpolation and the isoparametric concept, the reader is referred to Zienkiewicz et al. [1977] or Braess [2013].

4.5 Discretization in space

In this section, the discretization of the weak form is carried out. First, the discretization on the element level is introduced and subsequently on the global level. For convenience, symmetric tensors $\mathbf{a}$ are now denoted in Voigt notation $\tilde{\mathbf{a}}$ (see appendix 13.2.5).
The isoparametric *ansatz* (4.28) for the displacement field of a finite element e can be written in matrix notation

$$\boldsymbol{u}(\boldsymbol{\xi}) = N_i(\boldsymbol{\xi})\hat{\boldsymbol{u}}^i = \mathbf{H}(\boldsymbol{\xi})\hat{\tilde{\boldsymbol{u}}}^e = \begin{bmatrix} N_1(\boldsymbol{\xi}) & 0 & 0 & \cdots & N_n(\boldsymbol{\xi}) & 0 & 0 \\ 0 & N_1(\boldsymbol{\xi}) & 0 & \cdots & 0 & N_n(\boldsymbol{\xi}) & 0 \\ 0 & 0 & N_1(\boldsymbol{\xi}) & \cdots & 0 & 0 & N_n(\boldsymbol{\xi}) \end{bmatrix} \begin{bmatrix} \hat{u}_1^1 \\ \hat{u}_2^1 \\ \hat{u}_3^1 \\ \vdots \\ \hat{u}_1^n \\ \hat{u}_2^n \\ \hat{u}_3^n \end{bmatrix}, \tag{4.33}$$

where $\mathbf{H}$ is the shape function interpolation matrix. By notational abuse, the element-vector $\hat{\tilde{\boldsymbol{u}}}^e$ has been introduced, such that multiplying $\hat{\tilde{\boldsymbol{u}}}^e$ with the $\mathbf{B}$-matrix results in Voigt-notated strains:

$$\tilde{\boldsymbol{\varepsilon}} \approx \mathrm{Grad}(N_i(\boldsymbol{\xi}))\hat{\boldsymbol{u}}^i = \mathbf{D}\mathbf{H}\hat{\tilde{\boldsymbol{u}}}^e = \mathbf{B}\hat{\tilde{\boldsymbol{u}}}^e\,, \tag{4.34}$$

where

$$\mathbf{D} = \begin{bmatrix} \frac{\partial}{\partial x_1} & 0 & 0 \\ 0 & \frac{\partial}{\partial x_2} & 0 \\ 0 & 0 & \frac{\partial}{\partial x_3} \\ \frac{\partial}{\partial x_2} & \frac{\partial}{\partial x_1} & 0 \\ 0 & \frac{\partial}{\partial x_3} & \frac{\partial}{\partial x_2} \\ \frac{\partial}{\partial x_1} & 0 & \frac{\partial}{\partial x_1} \end{bmatrix} \tag{4.35}$$

is the matrix with the suitable partial derivatives to construct the discretized linearized displacement gradient. Inserting (4.33) and (4.34) into (4.25) yields the discretized version of the linearized weak form as

$$(\delta\tilde{\boldsymbol{u}}^e)^{\mathrm{T}} \underbrace{\int_{\mathcal{B}_e} \mathbf{B}^{\mathrm{T}}\,\bar{\bar{\mathbf{C}}}_{(n+1)}\,\mathbf{B}\,\mathrm{d}\,V}_{\mathbf{K}^e_{(n+1)}}\ \Delta\hat{\tilde{\boldsymbol{u}}}^e = (\delta\tilde{\boldsymbol{u}}^e)^{\mathrm{T}} \left[\underbrace{-\int_{\mathcal{B}_e} \mathbf{B}^{\mathrm{T}}\,\tilde{\boldsymbol{\sigma}}_{(n)}\,\mathrm{d}\,V}_{\boldsymbol{f}^{e,\mathrm{int}}_{(n)}} + \underbrace{\int_{\Gamma_{\sigma_e}} \mathbf{H}^{\mathrm{T}}\hat{\tilde{\boldsymbol{t}}}^e_{(n+1)}\,\mathrm{d}\,A}_{\boldsymbol{f}^{e,\mathrm{ext}}_{(n+1)}} \right]. \tag{4.36}$$

Since this equation has to hold for arbitrary admissible virtual displacement fields $(\delta\boldsymbol{u})^{\mathrm{T}}$, the equivalent system of equations for a generic element e can be denoted as

$$\mathbf{K}^{e}_{(n+1)}\,\Delta\hat{\hat{\boldsymbol{u}}} = \boldsymbol{f}^{e,\mathrm{ext}}_{(n+1)} - \boldsymbol{f}^{e,\mathrm{int}}_{(n)}\,. \tag{4.37}$$

It is noted that for the integration of the matrices a suitable numerical integration scheme has to be introduced [see, e.g., Zienkiewicz et al., 1977].

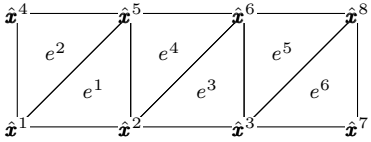

Figure 4.2: Rectangular domain meshed by linear triangles.

Now consider a domain $\mathcal{B}_0$, discretized by a set of finite elements $\{e^i\}_{i=1,\ldots,n_{\mathrm{elems}}}$(see figure 4.2), such it can be stated that

$$\mathcal{B}_0 \approx \bigcup_{e=1}^{n_{\mathrm{elems}}} \mathcal{B}_e\,. \tag{4.38}$$

Subsequently, the global system of equations can then be stated as

$$\mathbf{K}_{(n+1)}\,\Delta\hat{\hat{\boldsymbol{u}}} = \boldsymbol{f}^{\mathrm{ext}}_{(n+1)} - \boldsymbol{f}^{\mathrm{int}}_{(n)}\,, \tag{4.39}$$

where $\Delta\hat{\hat{\boldsymbol{u}}}$ is the *global* displacement increment vector at the nodal positions. The global stiffness matrix can be assembled, presuming a local-to-global mapping $\kappa : \{i\} \to \{i^g\}$ of the degrees of freedom, such that

$$\mathrm{K}_{i^g j^g} = \sum_{\substack{e=1 \\ i^g=\kappa(i)\wedge j^g=\kappa(j)}}^{n_{\mathrm{elems}}} \mathrm{K}^{e}_{\kappa(i)\kappa(j)}\,. \tag{4.40}$$

Furthermore, we can define the global internal force vector and global external force vector as

$$f^{\mathrm{int}}_{i^g} = \sum_{\substack{e=1 \\ i^g=\kappa(i)}}^{n_{\mathrm{elems}}} f^{e,\mathrm{int}}_{\kappa(i)} \quad \text{and} \quad f^{\mathrm{ext}}_{i^g} = \sum_{\substack{e=1 \\ i^g=\kappa(i)}}^{n_{\mathrm{elems}}} f^{e,\mathrm{ext}}_{\kappa(i)}\,, \tag{4.41}$$

respectively.

4.6 Non-linear solution: the Newton-Raphson scheme

In order to solve the non-linear equation (4.13), the iterative Newton-Raphson method is employed. The Newton-Raphson iteration counter will be denoted by a superscript (k) in parentheses, with the first iteration starting at $k = 1$. In contrast global time increments will be denoted by a subscript (t) in parentheses.

For the first global time step, the global displacement vector and the bone mineral density vector have to be initialized, that is

$$\hat{\hat{\boldsymbol{u}}}_{(0)} = 0 \quad \text{and} \quad \boldsymbol{\varrho}_{(0)} = \varrho_0 \,. \tag{4.42}$$

Note that the displacement field is initialized at the nodal positions while the bone mineral density is initialized at the integration point level. Presuming the solution $\hat{\hat{\boldsymbol{u}}}_{(n)}$ is known, it is possible to obtain the next solution vector

$$\hat{\hat{\boldsymbol{u}}}_{(n+1)} \approx \hat{\hat{\boldsymbol{u}}}^{(m-1)}_{(n+1)} + \Delta\hat{\hat{\boldsymbol{u}}}^{(m)} = \hat{\hat{\boldsymbol{u}}}_{(n)} + \sum_{i=1}^{m-1} \Delta\hat{\hat{\boldsymbol{u}}}^{(i)} + \Delta\hat{\hat{\boldsymbol{u}}}^{(m)} \tag{4.43}$$

from the increments $\Delta\hat{\hat{\boldsymbol{u}}}^{(k)}$ of a converged Newton-Raphson procedure with (m) iterations. An incremental version of the weak form (4.36) at $\bar{t} = t_{(n)} + \sum_{i=1}^{k-1} \Delta t^{(i)}$ can be stated as

$$(\delta\tilde{\boldsymbol{u}}^e)^{\mathrm{T}} \underbrace{\int_{\mathcal{B}_e} \mathbf{B}^{\mathrm{T}}\, \bar{\tilde{\mathbb{C}}}^{(k)}_{(n+1)}\, \mathbf{B}\, \mathrm{d}V}_{\mathbf{K}^{e(k)}_{(n+1)}} \Delta\hat{\hat{\boldsymbol{u}}}^{e(k)} = -\,(\delta\tilde{\boldsymbol{u}}^e)^{\mathrm{T}} \left[\underbrace{\int_{\mathcal{B}_e} \mathbf{B}^{\mathrm{T}}\, \tilde{\boldsymbol{\sigma}}^{(k)}_{(n+1)}\, \mathrm{d}V}_{\boldsymbol{f}^{e,\mathrm{int}(k)}_{(n+1)}} + \underbrace{\int_{\Gamma_{\sigma_e}} \mathbf{H}^{\mathrm{T}} \hat{\tilde{\boldsymbol{t}}}^e_{(n+1)}\, \mathrm{d}A}_{\boldsymbol{f}^{e,\mathrm{ext}}_{(n+1)}} \right] . \tag{4.44}$$

In the above, the algorithmic consistent material tangent can be found by the following derivation

$$\bar{\tilde{\mathbb{C}}}^{(k)}_{(n+1)} = \left. \frac{\tilde{\mathbb{C}}(\varrho_{(n)} + \Delta\varrho^{(k)})}{\partial\tilde{\boldsymbol{\varepsilon}}^*_{(n+1)}} \right|_{\bar{t}} : \tilde{\boldsymbol{\varepsilon}}^{\mathrm{tr},(k)}_{(n+1)} + \tilde{\mathbb{C}}(\varrho_{(n)} + \Delta\varrho^{(k)}) \,, \tag{4.45}$$

where the iterative trial strains

$$\tilde{\boldsymbol{\varepsilon}}^{\mathrm{tr},(k)}_{(n+1)} = \tilde{\boldsymbol{\varepsilon}}_{(n)} + \sum_{i=1}^{k-1} \Delta\tilde{\boldsymbol{\varepsilon}}^{(i)} \tag{4.46}$$

have been defined at the integration points, and the residual stresses are given by

$$\tilde{\boldsymbol{\sigma}}^{(k)}_{(n+1)} = \tilde{\boldsymbol{\sigma}}_{(n)} + \sum_{i=1}^{k-1} \Delta\tilde{\boldsymbol{\sigma}}^{(i)}_{(n+1)} \,. \tag{4.47}$$

Note that the increment of the bone mineral density

$$\Delta\varrho^{(k)} = \Delta t \hat{\mathfrak{R}}(\varrho_{(n)}, \tilde{\boldsymbol{\varepsilon}}^{\mathrm{tr},(k)}_{(n+1)}) \tag{4.48}$$

still depends only on the last converged bone mineral density $\varrho_{(n)}$ and the trial strains $\tilde{\boldsymbol{\varepsilon}}^{\mathrm{tr},(k)}_{(n+1)}$. Assembling the element weak form (4.44) results in the system of equations

$$\mathbf{K}^{(k)}_{(n+1)}\, \Delta\hat{\hat{\boldsymbol{u}}}^{(k)} = \boldsymbol{f}^{\mathrm{ext}}_{(n+1)} - \boldsymbol{f}^{\mathrm{int}(k)}_{(n+1)} \,, \tag{4.49}$$

which can be solved for the unknown increment $\Delta\hat{\hat{\boldsymbol{u}}}^{(k)}$. The Newton-Raphson iterations are repeated until for some time-step (m) the procedure is said to be converged if the following condition is fulfilled:

$$\frac{||\Delta\hat{\hat{\boldsymbol{u}}}^{(m)} - \Delta\hat{\hat{\boldsymbol{u}}}^{(m-1)}||}{||\Delta\hat{\hat{\boldsymbol{u}}}^{(1)}||} < \epsilon_{\mathrm{tol}} \,, \tag{4.50}$$

where ϵ_{tol} is a user-defined parameter. The bone material density can only be updated once convergence has been achieved

$$\varrho_{(n+1)} = \varrho_{(n)} + \Delta\varrho^{(m)} \,. \tag{4.51}$$

Chapter 5

Automated model generation

The successful introduction of numerical methods into clinical routine depends largely on the ability to readily convert available patient-individual data, such as CT data or X-ray images, into discrete geometric models onto which numerical analysis can be performed reliably.
Around 1970 *computed tomography* (CT) was established as a quantitative measure for non-invasive determination of bone mineral density [see among others Cameron et al., 1968, Abols et al., 1978, Bradley et al., 1978, Cann and Genant, 1980]. A first approach using CT scans as input for subject-specific finite element analysis was carried out by Huang et al. [1980]. Keyak et al. [1990] were among the first to provide an automated approach thereof. In the following, many more researchers contributed to semi-automated [see, e.g., Cattaneo et al., 2001] or fully-automated approaches [Viceconti et al., 1998a, Taddei et al., 2003, Lavecchia et al., 2018, among others] in patient-specific model generation in biomechanics. Despite the fact that it was shown early that subject-specific finite element models are capable of predicting strains accurately in the human femur [Guldberg et al., 1998, Schileo et al., 2007], to this day, there is a lack of knowledge in how different scanner types, resolutions, setting, and different anatomic locations contribute to the overall error of a finite element analysis [Knowles et al., 2016].
Also, an approach in automatic model generation in two-dimensions from *dual-energy x-rays absorptiometry* (DEXA) was proposed in Luo et al. [2018]. In Grassi et al. [2017] *statistical shape and appearance models* were used to create three-dimensional models from a single DEXA-image, and in Ahmad et al. [2010] and Humbert et al. [2016], the generation of three-dimensional finite element models from multiple DEXA-images were proposed. However, fully automated model generation from DEXA-images in three dimensions is not yet available.
Comparing both approaches, Viceconti et al. [2018] concluded that while subject-specific finite element models from CT scans seem to be more accurate compared with the DEXA approach, it is not guaranteed that CT-based finite element analyses are, in fact, cost-efficient.
Streamlined software solutions that create finite element meshes efficiently mostly depend on a boundary representation of the geometry as an input. In order to take advantage of that kind of software, it is necessary to transfer the stack of CT images to such a boundary representation. A solution to that problem was provided by Viceconti et al. [1998b]. Since this is stated to be beyond the scope of this thesis, it will be assumed that a boundary representation of CT data is available in the following.
It is noted that Young et al. [2008] provided an approach for creating a finite element mesh directly from CT data, which is not applicable here since an intermediate representation, where geometric operations can be performed efficiently, is preferable.
Finally, taking Pavarino et al. [2013] as an example, where free tools and strategies are exploited in order to create a model of the cardiac structure, in the following, only open-source software shall be used in order to create the finite element model from CAD geometry, automatically.

5.1 Geometric manipulations

CAD models of a femur and a prosthesis, adopted from Lutz [2011], serve as input for the finite element model generation (see figure 5.1a). These CAD models were generated from CT data with the help of the commercial software ICEM Surf. Still, they could have been created with the approach stated in Viceconti et al. [1998b] as well, to be in line with the open-source software approach emphasized in the following. The femur and prosthesis possess an initial position that is equivalent to a physiologically suitable installation position. Along with the

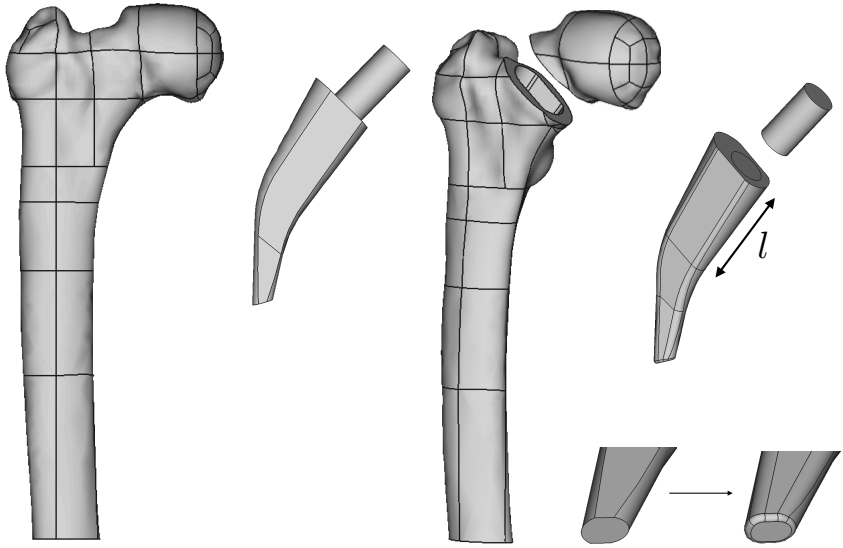

(a) Input CAD models of human femur and prosthesis.

(b) CAD models after geometric manipulations.

Figure 5.1: CAD models of femur and prosthesis.

geometries, there are seven further user-definable parameters; the first six describe a deviation from the initial position (see figure 5.2 for a simplified schematic representation):

- $\theta_1 \in \mathcal{I}_1$, $\mathcal{I}_1 = [\theta_{1,\min}, \theta_{1,\max}]$ is a longitudinal shift in millimeters. The longitudinal axis is oriented along the medial axis of the coated area of the prosthesis (compare with red arrow in figure 5.2).
- $\theta_2 \in \mathcal{I}_2$, $\mathcal{I}_2 = [\theta_{2,\min}, \theta_{2,\max}]$ is a transversal shift in millimeters. The transversal axis is oriented perpendicular to the longitudinal axis as indicated in figure 5.2 by the green arrow.
- $\theta_3 \in \mathcal{I}_3$, $\mathcal{I}_3 = [\theta_{3,\min}, \theta_{3,\max}]$ is a sagittal shift in millimeters. The sagittal axis is perpendicular to both the longitudinal and the transversal axis.
- $\theta_4 \in \mathcal{I}_4$, $\mathcal{I}_4 = [\theta_{4,\min}, \theta_{4,\max}]$ is the pitch angle in degrees (compare with blue arrow in figure 5.2). The pitch angle rotates around the sagittal axis with origin in the centre of gravity of the prosthesis.

- $\theta_5 \in \mathcal{I}_5$, $\mathcal{I}_5 = [\theta_{5,\min}, \theta_{5,\max}]$ is the yaw angle in degrees. The yaw angle rotates around the transversal axis with origin in the centre of gravity of the prosthesis.

- $\theta_6 \in \mathcal{I}_6$, $\mathcal{I}_6 = [\theta_{6,\min}, \theta_{6,\max}]$ is the roll angle in degrees. The roll angle rotates around the longitudinal axis with origin in the centre of gravity of the prosthesis.

The last parameter $\theta_7 \in \mathcal{I}_7$, $\mathcal{I}_7 = [\theta_{7,\min}, \theta_{7,\max}]$ defines the length l of the coating area of the prosthesis as indicated in figure 5.1b. The first six parameters are assembled in the vector $\boldsymbol{\theta}^{\mathrm{M}} = \{\theta_i\}_{i=1,\ldots,6}$.

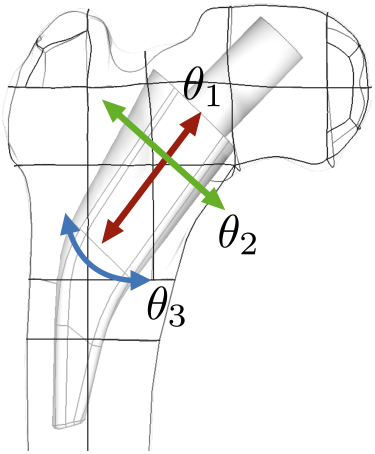

Figure 5.2: Simplified schematic representation of parameterized implant position.

The actual geometric manipulations are performed with the help of the open-source software FreeCAD [Riegel et al., 2016], a general-purpose *parametric* 3D CAD modeler and *building information modeler* [see, e.g., Azhar, 2011], which in turn is based on the open-source software project Open Cascade [Bedaka and Lin, 2018], which provides the *geometric modeling kernel*. FreeCAD itself is accessible on a programmatic level through the in-built FreeCAD python interpreter, which allows for the repeated execution of a constant set of instructions taking into account a varying set of parameters $\boldsymbol{\theta}^{\mathrm{M}}$.
The set of instructions can be summarized into the following three steps:

1. **Model smoothing**: to not introduce singularities within the osseointegration interface, the CAD model of the prosthesis is smoothed with the help of so-called *fillets* (cf. figure 5.1b).

2. **Model positioning**: the prosthesis is positioned and configured according to the set of parameters $\boldsymbol{\theta}^{\mathrm{M}}$.

3. **Boolean operations**: the bone and prosthesis are fused by an operation called boolean fragments, deriving all single fragments that can result from applying boolean operation between two input shapes. Finally, an incision is made to separate the head of the femur from the rest of the model. This is also done based on the set of modeling parameters $\boldsymbol{\theta}^{\mathrm{M}}$.

All parts of the resulting geometry are displayed in figure 5.1b. The output of this modeling step is a united geometric model of the whole femur with inserted prosthesis.

5.2 Mesh generation

As a meshing tool for the resultant geometry from the last step, GMSH [Geuzaine and Remacle, 2009] was chosen. GMSH is an open-source 3D finite element mesh generator with its own in-build geometry kernel as well as access to OPEN CASCADE, but neither provides the same extend of functionality as provided by FREECAD. Interfacing with GMSH can be realized by using a proprietary scripting language, where features of the mesh, such as characteristic lengths of different parts of the geometry, can be conveniently configured. The resultant mesh for an exemplary discretization can be seen in figure 5.3, where different colors refer to separate physical entities of the mesh. Since all geometric operations are done within FREECAD this interface is

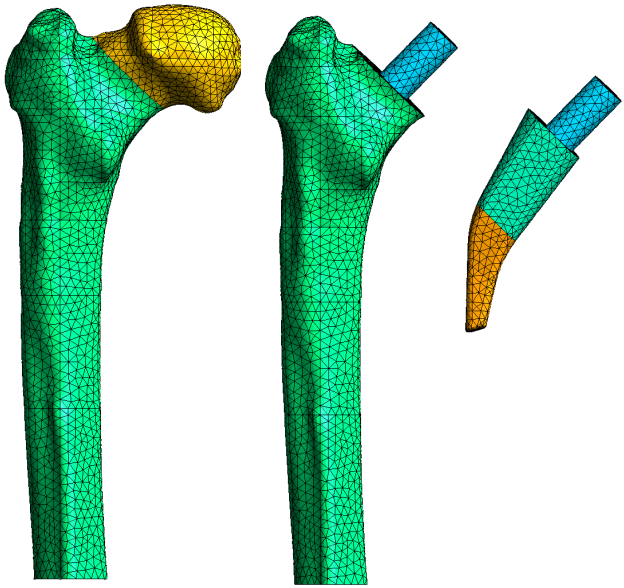

Figure 5.3: Resultant mesh.

mainly used to control the mesh size in different areas of the model.

It shall be stated here once again that the modeling approach proposed in this thesis relies only on freely accessible software and is, in fact, **fully automated**, while the input geometry, all parameters $\boldsymbol{\theta}$ as well as the mesh density at different locations within the geometry are exposed to the top level as user-definable inputs.

Chapter 6

Virtual X-ray imaging

Finite element analyses in orthopedic biomechanics provide deep insights into the physics of the human body. For such analyses to represent a meaningful complement to purely medical research, it can be helpful to transfer the results into a medical imaging format, such as a radiographic or tomographic image. In computational bone remodeling, there are two major advantages to this approach: (1) the internal bone mineral density distribution is hard to infer from finite element post-processing results since only the boundary of the specimen is immediately visible and (2) also people without a technical background in finite elements, e.g., medicines, can evaluate the results in that way.
The simulation of X-ray images from a polygonal mesh is a well-researched topic, and there are several simulation codes available, such as described in Freud et al. [2006], Baro et al. [1995] and Sujar et al. [2017], for example. Baro et al. [1995] use Monte Carlo simulation to generate realistic images, while Freud et al. [2006] and Sujar et al. [2017] use fast ray casting algorithms for that purpose. Whilst Sujar et al. [2017] account for density distribution with higher polynomial order, to the author's knowledge, there is no work available that operates directly onto finite element results and accounts for higher polynomial orders in both density distribution and geometry representation. For this purpose, a novel approach will be presented in this chapter.

6.1 Method description

To obtain an x-ray image of an arbitrary finite element result, the approved method of sending rays through the finite element mesh and subsequently integrating the quantity of interest along these rays will be used in this approach. Since the intersection test of each ray with every finite element is computationally expensive, as a first step and for a given ray, the number of finite element candidates for the intersection test has to be reduced. For this purpose, a tree structure of nested bounding boxes is employed, whereby the elements contained in a bounding box are bisected in the next hierarchical level. Since intersection tests with bounding boxes are very cheap, the tree of bounding boxes can be efficiently used to reduce the number of candidate elements. Since, even with this method, the determination of the exact points of intersection of the ray and the finite element will be computationally expensive if performed for a large number of rays or a huge finite element mesh, numerical integration is introduced at this point. Using this method, it is only necessary to test whether a discrete point is inside a finite element. As soon as the positional relationship of the point and the finite element is known in terms of element coordinates, it is simple to obtain the quantity of interest at the discrete point with the help of shape functions from an element-wise finite element post-processing result.

6.2 Hierarchical-structured oriented bounding boxes

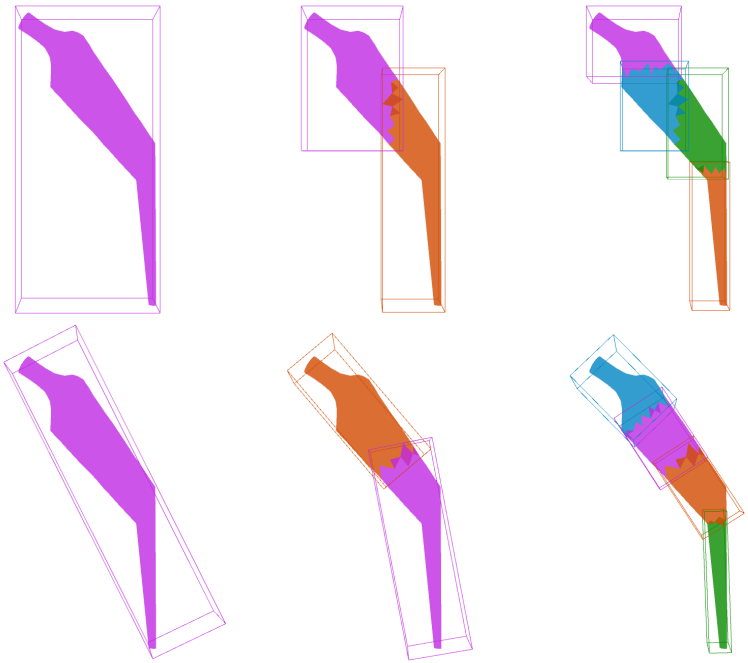

Figure 6.1: AABBs (upper pictures) vs. OBBs (lower pictures).

A bounding box for a collection of objects, such as an axis-aligned bounding box (AABB) or an oriented bounding box (OBB), is a closed volume that completely contains the collection of objects. In Gottschalk et al. [1996], a tree structure of hierarchical OBB's is introduced. Therein, principal component analysis [Jolliffe, 2011] is used to create a set of nested tight-fitting bounding boxes. This method could also be used efficiently for contact detection in the finite element method [Gottschalk et al., 1996].

6.2.1 Principal component analysis

Let $k = 1, ..., n$ and s_k be a linear triangle or so-called 2-simplex with vertices $\hat{\boldsymbol{p}}^k$, $\hat{\boldsymbol{q}}^k$, and $\hat{\boldsymbol{r}}^k$ in $\mathbb{R}^3$. The centroid and the area of each simplex s_k in $\mathbb{R}^3$ may be calculated by

$$\boldsymbol{c}^k = \frac{1}{3}\left(\hat{\boldsymbol{p}}^k + \hat{\boldsymbol{q}}^k + \hat{\boldsymbol{r}}^k\right) \quad \text{and} \tag{6.1}$$

$$A^k = \sqrt{\gamma^k \left(\gamma^k - ||\hat{\boldsymbol{p}}^k - \hat{\boldsymbol{q}}^k||\right)\left(\gamma^k - ||\hat{\boldsymbol{q}}^k - \hat{\boldsymbol{r}}^k||\right)\left(\gamma^k - ||\hat{\boldsymbol{r}}^k - \hat{\boldsymbol{p}}^k||\right)}, \tag{6.2}$$

subsequently, with

$$\gamma^k = \frac{1}{2}\left(||\hat{\boldsymbol{p}}^k - \hat{\boldsymbol{q}}^k|| + ||\hat{\boldsymbol{q}}^k - \hat{\boldsymbol{r}}^k|| + ||\hat{\boldsymbol{r}}^k - \hat{\boldsymbol{p}}^k||\right) . \tag{6.3}$$

The (area-)weighted center of all simplices s_k can then be given by

$$\boldsymbol{\mu} = \frac{\sum\limits_k A^k \boldsymbol{c}^k}{\sum\limits_k A^k} , \tag{6.4}$$

which is independent of the distribution of the vertices in space. Using zero-centered centroids

$$\bar{\boldsymbol{c}}^k = \sqrt{A^k}\left(\boldsymbol{c}^k - \boldsymbol{\mu}\right) , \tag{6.5}$$

the definition of the covariance matrix is given by

$$\mathcal{C}_{ij} = \frac{1}{n-1}\sum_k \bar{c}_i^k \bar{c}_j^k , \tag{6.6}$$

which is a symmetric positive (semi-)definite 3×3-matrix and thus owns real eigenvalues and, due to spectral theorem, an orthonormal basis $\mathcal{B}'$ in $\mathbb{R}^3$ consisting of the three eigenvectors out of which two point in the direction of maximum and minimum variance [Jolliffe, 2011]. A change of basis $\mathcal{T}^{\mathcal{B}}_{\mathcal{B}'}$ can be performed by

$$\mathcal{T}^{\mathcal{B}}_{\mathcal{B}'} = (\mathcal{B}')^{-1}\mathcal{B} = (\mathcal{B}')^{-1}\mathbf{I} = (\mathcal{B}')^{-1} = \mathcal{T}_{\mathcal{B}'} , \tag{6.7}$$

with identity matrix $\mathbf{I}$, since $\mathcal{B}$ is the standard basis for a Euclidean space. This procedure is easily extendable to higher dimensions or different primitives by specifying suitable definitions for $\mathbf{c}^k$ and A^k for the n-simplex with $n > 2$ or e.g., the n-cube.

6.2.2 Oriented bounding boxes

Let $S = \{s_k\}_{k=1,..,n}$ be a set of 2-simplices or triangles and

$$V = \bigcup_{s_k \in S} \left\{\hat{\boldsymbol{p}}^k, \hat{\boldsymbol{q}}^k, \hat{\boldsymbol{r}}^k\right\} \tag{6.8}$$

the set of 0-simplices or vertices contained in S. A convenient way to define a bounding box as an axis-aligned rectangular cuboid is given by the tuple

$$B(V) = \left(P^{\min}(V),\, P^{\max}(V)\right) , \quad \text{with} \tag{6.9}$$

$$P^{\min}(V) = (\min_{x_1}(V), \min_{x_2}(V), \min_{x_3}(V)) \quad \text{and} \tag{6.10}$$

$$P^{\max}(V) = (\max_{x_1}(V), \max_{x_2}(V), \max_{x_3}(V)) . \tag{6.11}$$

Obviously, $P_{\min}$ and $P_{\max}$ depend on the choice of the coordinate system. Choosing the standard basis in $\mathbb{R}^3$ leads to the class of axis-aligned bounding boxes (see figure 6.2). Allowing for different bases $\mathcal{B}'$, an oriented bounding box

$$B_{\mathcal{B}'}(V) = \left(P^{\min}(\mathcal{T}_{\mathcal{B}'}\, V),\, P^{\max}(\mathcal{T}_{\mathcal{B}'}\, V)\right) . \tag{6.12}$$

can be defined.
Applying principal component analysis, shown in section 6.2.1, to the triangulation $T = (V, S)$ of the convex hull [Barber et al., 1996] of a body in $\mathbb{R}^3$ and using the obtained basis $\mathcal{B}^T$ as an input for the orientated bounding box

$$B_{\mathcal{B}^T}(V) = \left(P^{\min}(\mathcal{T}_{\mathcal{B}^T}\, V),\, P^{\max}(\mathcal{T}_{\mathcal{B}^T}\, V)\right) , \tag{6.13}$$

the result will most likely fit the body tightly.

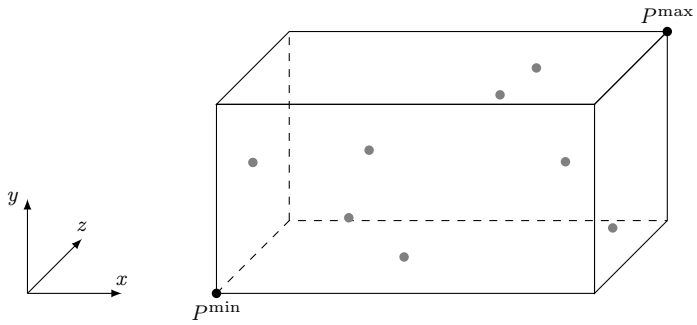

Figure 6.2: Axis aligned bounding box.

6.2.3 Hierarchical decomposition

In the latter, an algorithm was defined for the creation of tight-fitting OBBs around a body in $\mathbb{R}^3$. A top-down hierarchy is used for the generation of a series of nested OBBs with gradually smaller volumes. Therefore, a parent OBB $B^P_{(\star)}$ including the complete body, is computed. The subdivision rule implemented then splits the bounding box with a plane orthogonal to the longest axis of the box in the center of mass. If the longest axis cannot be subdivided, the second-longest axis is chosen. For the resulting two distinct regions, two children OBBs $B^{C_1}_{(\star)}$ and $B^{C_2}_{(\star)}$ can be computed. This procedure may be repeated as long as a dividable convex hull of the fraction of the underlying geometry can be calculated. The parent and child OBBs can be organized efficiently in a binary tree structure. In figure 6.1, two steps of this procedure for AABBs and OBBs are shown using the example of an endoprosthesis. As can been seen, the OBBs converge faster than AABBs to the shape of the underlying geometry.

6.3 Ray casting geometric primitives in $\mathbb{R}^3$

In computer graphics, the use of ray-surface or line-surface intersection tests, needed in a variety of related problems such as volume rendering, is termed ray casting [Pfister et al., 1999]. A Ray can be defined by the tuple

$$R = (\boldsymbol{o}, \boldsymbol{d}), \quad \boldsymbol{o}, \boldsymbol{d} \in \mathbb{R}^3, \tag{6.14}$$

with the origin $\boldsymbol{o}$ and the direction $\boldsymbol{d}$ of the Ray.
In the following section, the intersection of a ray with two different classes of geometric primitives is outlined: (1) the rectangular cuboid and (2) the tetrahedron.

6.3.1 Intersection of ray and rectangular cuboid

The class of rectangular cuboids is congruent with the class of oriented bounding boxes. Therefore we restrict ourselves to the determination of the intersection of a ray with an oriented bounding box. Via the map

$$R^\star = \mathcal{T}_{\mathcal{B}'} R = (\mathcal{T}_{\mathcal{B}'} \boldsymbol{o}, \mathcal{T}_{\mathcal{B}'} \boldsymbol{d}), \tag{6.15}$$

the ray R can easily be transformed into the coordinate system of the OBB, reducing the model problem to the collision of a ray $R^\star$ with an AABB. For this problem class, the slab method, first proposed in Kay and Kajiya [1986], is an easy and fast solution.

Slab method.

For the explanation of the slab method, the two-dimensional example shown in figure 6.3 will be used. However, the procedure itself can be easily extended to three or more dimensions. A ray R can also be expressed with the following equation

$$\boldsymbol{R}(t) = \boldsymbol{o} + t \cdot \boldsymbol{d}\,, \quad t \in \mathbb{R}^+\,, \tag{6.16}$$

which is a simple linear equation. The bounding box can be represented as the intersection of

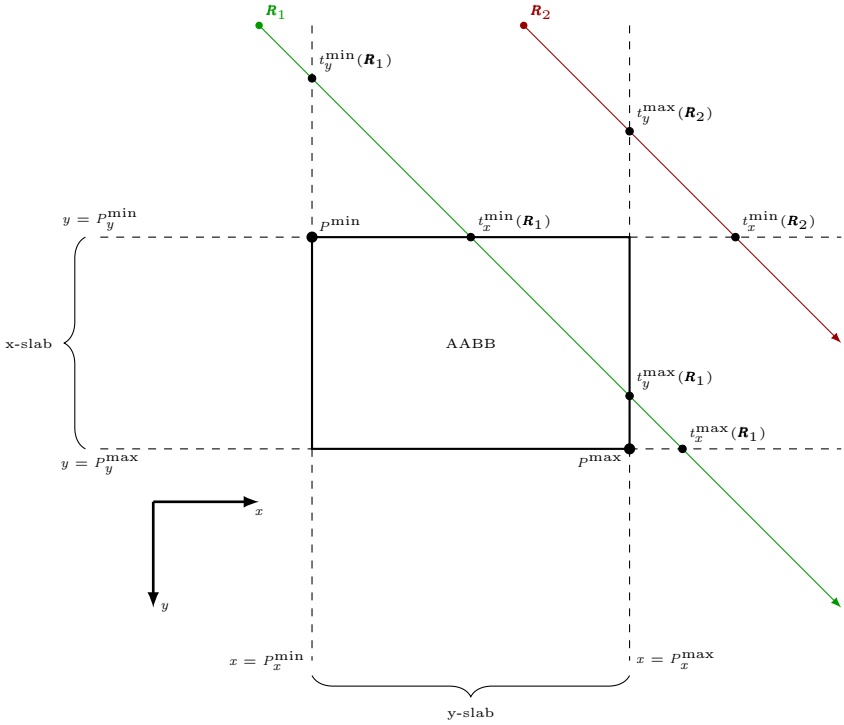

Figure 6.3: Intersection-test of two Rays $\boldsymbol{R}_1$ and $\boldsymbol{R}_2$ with a 2D-AABB.

two slabs, the x-slab, defined by two parallel lines $y = P_y^{\min}$ and $y = P_y^{\max}$, both perpendicular to the y-axis, and the y-slab, defined by two parallel lines $x = P_x^{\min}$ and $x = P_x^{\max}$, both perpendicular to the x-axis. The minimal and maximal points of intersection of the ray with the x-slab can be calculated by

$$t_x^{\min} = \frac{(P_y^{\min} - o_y)}{d_y} \quad \text{and} \quad t_x^{\max} = \frac{(P_y^{\max} - o_y)}{d_y}\,. \tag{6.17}$$

Accordingly, the intersection of the ray with the y-slab is calculated by

$$t_y^{\min} = \frac{(P_x^{\min} - o_x)}{d_x} \quad \text{and} \quad t_y^{\max} = \frac{(P_x^{\max} - o_x)}{d_x}\,. \tag{6.18}$$

The ray then intersects with the bounding box if and only if

$$\max(t_x^{\min}, t_y^{\min}) < \min(t_x^{\max}, t_y^{\max}) \tag{6.19}$$

the largest minimum is smaller than the smallest maximum, which holds for $\boldsymbol{R}_1$, and in contrast, does not hold for $\boldsymbol{R}_2$; both depicted in figure 6.3. Thus, this algorithm allocates no memory, and if $\frac{1}{d_i}$ is pre-computed, it is division-free, in addition.

6.3.2 Intersection of ray and tetrahedron

A tetrahedron can be decomposed into its set of four two-dimensional faces. Therefore we restrict ourselves to the intersection of a ray with a two-simplex. To determine the intersection of a ray with a two-simplex in $\mathbb{R}^3$, the Möller–Trumbore intersection algorithm [Möller and Trumbore, 2005] can be used as follows.

Möller–Trumbore intersection algorithm. A representation based on barycentric coordinates of a triangle s with vertices $\hat{\boldsymbol{p}}$, $\hat{\boldsymbol{q}}$, and $\hat{\boldsymbol{r}}$ can be given by the set of equations:

$$\begin{aligned} \mathbf{s}(u,v) = (1-u-v)\cdot\hat{\boldsymbol{p}} + u\cdot\hat{\boldsymbol{q}} + v\cdot\hat{\boldsymbol{r}}\,, \quad u,v\in\mathbb{R}\,, \\ u\geq 0\,, \quad v\geq 0\,, \quad \text{and} \quad u+v\leq 1\,. \end{aligned} \tag{6.20}$$

The intersection of a ray $\boldsymbol{R}(t)$ with a triangle $\mathbf{s}(u,v)$ can be found by solving the equation

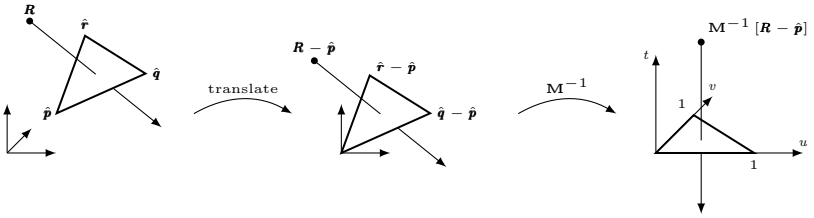

Figure 6.4: Translation and change of basis of the ray and the triangle [cf. Möller and Trumbore, 2005].

$$\begin{aligned} &\boldsymbol{R}(t) = \mathbf{s}(u,v) \\ \Rightarrow\ &\boldsymbol{o} + t\cdot\boldsymbol{d} = (1-u-v)\cdot\hat{\boldsymbol{p}} + u\cdot\hat{\boldsymbol{q}} + v\hat{\boldsymbol{r}}\,. \end{aligned} \tag{6.21}$$

Rearranging the terms

$$-t\cdot\boldsymbol{d} + u\cdot(\hat{\boldsymbol{q}}-\hat{\boldsymbol{p}}) + v\cdot(\hat{\boldsymbol{r}}-\hat{\boldsymbol{p}}) = \boldsymbol{o}-\hat{\boldsymbol{p}}\,, \tag{6.22}$$

which can be seen as the translation of $\hat{\boldsymbol{p}}$ to the origin (see figure 6.4), yields the linear system of equations

$$\underbrace{\left[-\boldsymbol{d}, \quad \hat{\boldsymbol{q}}-\hat{\boldsymbol{p}}, \quad \hat{\boldsymbol{r}}-\hat{\boldsymbol{p}}\right]}_{\mathbf{M}} \begin{bmatrix} t \\ u \\ v \end{bmatrix} = \boldsymbol{o}-\hat{\boldsymbol{p}}\,, \tag{6.23}$$

where $\mathbf{M}^{-1}$ can be seen as the transformation of $\boldsymbol{R}$ and $\mathbf{s}$, such that $\mathbf{s}$ is the unit-triangle shown in figure 6.4.

Denoting $\boldsymbol{E}_1 = \hat{\boldsymbol{q}} - \hat{\boldsymbol{p}}$, $\boldsymbol{E}_2 = \hat{\boldsymbol{r}} - \hat{\boldsymbol{p}}$ and $\boldsymbol{T} = \boldsymbol{o} - \hat{\boldsymbol{p}}$, the solution to (6.23) can be obtained using Cramer's rule

$$\begin{bmatrix} t \\ u \\ v \end{bmatrix} = \frac{1}{(\boldsymbol{d} \times \boldsymbol{E}_2) \cdot \boldsymbol{E}_1} \begin{bmatrix} (\boldsymbol{T} \times \boldsymbol{E}_1) \cdot \boldsymbol{E}_2 \\ (\boldsymbol{D} \times \boldsymbol{E}_2) \cdot \boldsymbol{T} \\ (\boldsymbol{T} \times \boldsymbol{E}_1) \cdot \boldsymbol{d} \end{bmatrix} . \tag{6.24}$$

The ray $\boldsymbol{R}(t)$ then intersects with the triangle $\mathbf{s}(u, v)$ at $\boldsymbol{o} + t \cdot \boldsymbol{d}$ if and only if $u > 0$, $v > 0$, $t > 0$, and $u + v \leq 1$.

6.4 Positional relationship of a discrete point with a finite element

Finding the points of intersection for a ray and a finite element with higher polynomial order is not trivial. Only a few sources are available that provide a solution. For example, Wiley et al. [2004] and Üffinger et al. [2010] describe ray casting algorithms for high-quality visualization of finite elements. Since we are not interested in visualizing finite elements in this work, the problem is reduced to the detection of the positional relationship of a discrete point $\boldsymbol{x}$ and a finite element, as mentioned earlier. With this simplification, the problem reduces to the search of the local coordinates $\boldsymbol{\xi}(\boldsymbol{x})$ dependent on the point $\boldsymbol{x}$, given in the global coordinate system.

6.4.1 Global-to-local iteration

For a given finite element with nodal coordinates $\hat{\boldsymbol{x}}^i$, $i = 1, ..., n_{\text{nodes}}$, associated shape functions $N_i(\boldsymbol{\xi})$, and a point $\boldsymbol{x}$, given in global coordinates, the element-local coordinates $\boldsymbol{\xi}$ need to be found, such that

$$\boldsymbol{f}(\boldsymbol{\xi}) = \mathbf{N}_i(\boldsymbol{\xi})\, \hat{\mathbf{x}}^i - \mathbf{x} = \mathbf{0} \,. \tag{6.25}$$

This problem can be solved by the Newton-Raphson algorithm

$$\boldsymbol{\xi}^{(n+1)} = \boldsymbol{\xi}^{(n)} - \mathbf{J}(\boldsymbol{\xi}^{(n)})^{-1} f(\boldsymbol{\xi}^{(n)}) \,, \tag{6.26}$$

with $\mathbf{J}$ being the Jacobian matrix with its components

$$\mathrm{J}_{ij} = \frac{\partial f_i}{\partial \xi_j}(\boldsymbol{\xi}) \,, \quad i = 1, \ldots, 3 \,,\, j = 1, \ldots, 3 \,, \tag{6.27}$$

an appropriate initial guess $\boldsymbol{\xi}_0$, and a convergence criterion

$$\frac{||\boldsymbol{\xi}^{(n+1)} - \boldsymbol{\xi}^{(n)}||}{||\boldsymbol{\xi}^{(1)}||} < \varepsilon_{\text{tol}} \,, \tag{6.28}$$

with a user-defined tolerance ε_{tol}.

6.4.2 In-hull test

Presuming $\boldsymbol{\xi}(\boldsymbol{x})$ is known, the quantity of interest q can be interpolated in terms of shape functions from an element-wise finite element post-processing result as $q(\boldsymbol{x}) = N_i(\boldsymbol{\xi}(\boldsymbol{x})) \cdot \hat{q}^i$. What remains is to check whether the local coordinates lie within the bounds of the reference element. Since all commonly used types of finite elements are usually convex, a simple test of whether $\boldsymbol{\xi}(\boldsymbol{x})$ lies within the convex hull of the reference finite element is sufficient. For the class of tetrahedral elements as used in this thesis, an in-hull test, taking advantage of the barycentric coordinate system, can be performed by

$$\sum_i \xi_i \leq 1 \quad \text{and} \quad \xi_i \geq 0 \,, \quad i = 1, \ldots, 3 \,, \tag{6.29}$$

for example.

6.5 Attenuation law

The initial intensity I_{in} of a beam of, e.g., electromagnetic radiation, decreases as it passes through a volume of matter. The *Beer-Lambert* law [Swinehart, 1962] relates this attenuation as

$$I_{\text{out}} = I_{\text{in}}\, e^{-\int \mu(\boldsymbol{x})\,\mathrm{d}x}\,, \tag{6.30}$$

where I_{out} is the resultant intensity and μ is the *linear attenuation coefficient*. For example, in Schneider et al. [1985], linear attenuation coefficients for compact and cancellous bone are stated as 2.251 cm^{-1} and 0.716 cm^{-1}, respectively.

6.6 X-ray generation

A relatively simple model is chosen with an orthographic projection and monochromatic X-ray beams for the X-ray setup. In an orthographic projection, the X-ray source is a plane with equally distributed parallel X-rays, while monochromatic means each X-ray beam shares the same energy. For more information about possible X-ray simulation setups, the reader is referred to Sujar et al. [2017], for example.
A summary of the X-ray simulation process can then be stated as follows:

1. An axis-aligned bounding box enclosing the complete finite element model is generated, whose surfaces can serve as emission plates.

2. A tree G of hierarchical-structured oriented boundary boxes is generated to subdivide the finite element model.

3. For every X-ray $\boldsymbol{R}_i$ sent through the model, the following steps are performed:

   (a) Find all leaves of G, which intersect with $\boldsymbol{R}_i$.

   (b) Introduce the numerical integration scheme $\bar{\boldsymbol{R}}_{ij} = \boldsymbol{o} + t_j \cdot \boldsymbol{d}$ by sampling the ray equidistantly with the desired resolution.

   (c) For each discrete point $\bar{\boldsymbol{R}}_{ij}$, perform the global-to-local iteration only on the finite elements inside the leaf bounding boxes.

   (d) Perform numerical integration on the quantity of interest, e.g.,

$$I_{\text{out}} = I_{\text{in}} \exp\left[-\sum_j w_j \mu(\varrho(\boldsymbol{R}_{ij}))\right]\,. \tag{6.31}$$

Although it is possible to introduce hierarchical levels in the tree G until each leaf is filled only with one finite element, it is not always sensible. It was found to be more efficient to create leaves with less than ten elements and then order them for each ray $\boldsymbol{R}_i$ by a linear guess performed by the Möller-Trumbore algorithm, introduced in 6.3.2.

6.7 Numerical examples

All methods described in this chapter were implemented within a self-developed framework, written in the julia language [Bezanson et al., 2017]. To demonstrate the functionality of the method and the implementation, two numerical examples are derived here. The first one is a coarsely discretized ball with constant density and the second one is a finer discretized disk with a quadratic density distribution.

6.7.1 Ball with constant density

As a first benchmark problem, a zero-centered ball $S : x^2 + y^2 + z^2 = r^2$, $x, y, z, r \in \mathbb{R}$ of radius $r = 1$ cm is discretized coarsely with 50 quadratic 10-node tetrahedral elements (see figure 6.5).

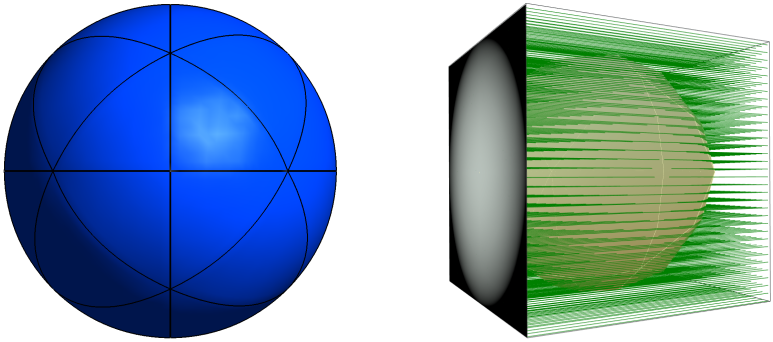

Figure 6.5: Ball discretized by 50 quadratic tetrahedral elements (left picture) and the model setup with a ball, initial bounding box, X-ray projection plane, and selected rays assembled in one scene (right picture).

A constant density of $\varrho = 1 \frac{\mathrm{g}}{\mathrm{cm}^3}$ is assigned to each element. An orthographic X-ray projection plane is set up, as shown in figure 6.5, using the X-ray algorithm to integrate the density of the discretized version of the ball. 23.668 rays per cm^2 are used to sample the discretized ball, resulting in 94.864 rays in total, while the density is sampled along each ray with the same frequency, resulting in 29.218.112 sample points in total. In figure 6.6, the resulting X-ray

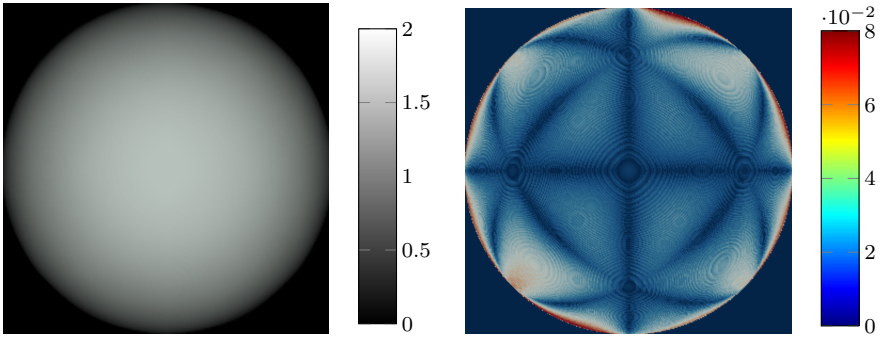

Figure 6.6: X-ray projection of the ball with density displayed in $\mathrm{g/cm}^2$ (left picture) and logscale plot of absolute error in $\mathrm{g/cm}^2$ (right picture).

image as well as the absolute error can be seen. The X-ray image looks as expected with a maximum density of 1.995 $\mathrm{g/cm}^2$ at the middle of the picture, as the X-ray passes the total diameter here. Integration once again over the projected density results in a mass of 4.135 g, which has a deviation of approximately 1.3 % compared to the analytically calculated mass $m = \varrho \frac{4}{3} \pi r^3 \approx 4.189\,\mathrm{g}$. The absolute error, which can be seen as the sum of the discretization

error of the ball and the discretization error of the rays, is measured at the location of each ray R_i by comparing the projected density with the integral $\int_{r_{i,\text{in}}}^{r_{i,\text{out}}} \varrho \, \mathrm{d}x$, where $r_{i,\text{in}}$ and $r_{i,\text{out}}$ are the intersection points of the ray with the analytical ball S. It can be seen that the error is the smallest where the vertices of the 10-node tetrahedral elements are clipped to the surface

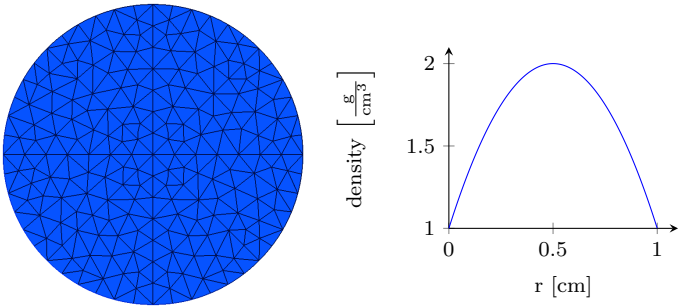

Figure 6.7: Cylinder discretized by 2143 quadratic tetrahedral elements (left picture) and density distribution depending on the radius r (right picture).

of the ball, followed by the edges and finally the faces. As expected, the most significant error occurs at the edge of the projected circle. In addition, concentric circles can be seen all over the picture, which can be interpreted as a sign of the depth discretization of the rays.

6.7.2 Cylinder with quadratic density distribution

As second test, a cylinder with radius $r = 1\,\text{cm}$ and height $h = 0.1\,\text{cm}$ is discretized with 2143 quadratic 10-node tetrahedral elements and a quadratic density distribution along the radius $\varrho(r) = -4(r-0.5)^2 + 2$ is assigned to the model (both shown in figure 6.7). The X-ray setup is

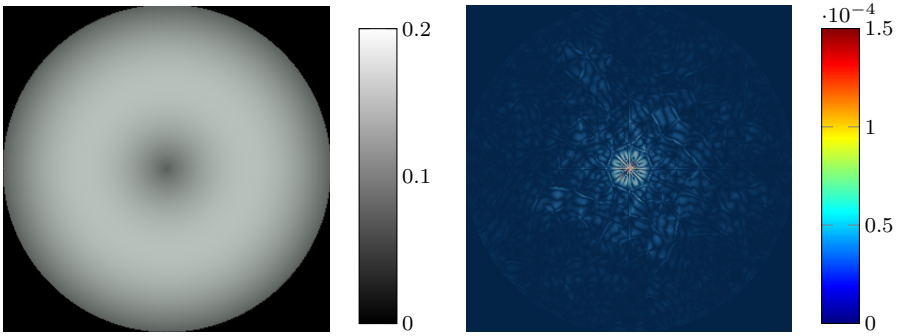

Figure 6.8: X-ray projection of the cylinder with density displayed in g/cm^2 (left picture) and plot of absolut error in g/cm^2 (right picture).

analogous to the latter example, except that there are fewer samples in the depth direction as the geometry and the density exhibit no variation in that direction. Therefore the integration is exact even with just one sample along each ray.

In figure 6.8, the projected density and the absolute error can be seen. The projected density looks as expected, which once again demonstrates the function of the X-ray simulation. However, the total error is at least two magnitudes lower as in the first example. This can be explained by the simplified geometry, which, as already mentioned, exhibits exact integration per ray, and by the finer mesh, which renders the discretization of the cylinder almost exactly.

Chapter 7

Numerical bone remodeling

Bone remodeling simulation using finite elements has been an active field of research in computational biomechanics for the last four decades. Starting from a one-dimensional finite element model in Woo et al. [1977], first attempts in two dimensions were carried out soon after that by, among others, Hayes and Snyder [1979] and Hayes et al. [1982]. The former example investigated the effect of an internal fixation plate on long bone remodeling, while the latter studied bone remodeling of trabecular bone of the patella.
Despite suffering from numerical instabilities, those early two-dimensional models, shown among others in the works of Carter et al. [1989], Beaupré et al. [1990a] and Weinans et al. [1992], were capable of reproducing the trabecular structure of bone and were in good agreement with experimental results. By this time, three prominent approaches for the remodeling stimulus were available in the literature: (1) the stress approach, (2) the fatigue damage approach, and (3) the strain energy density approach. Generalizing these ideas, Carter et al. [1987] (cf. Taber [1995]) defined a daily remodeling stimulus

$$\Psi_{\mathrm{d}} = K \left[\sum_{i=1}^{N} n_i \Psi_i^m \right] , \tag{7.1}$$

with N different daily loading cases i, each with n_i repetitions and associated stimulus Ψ_i, and constant K and m. Choosing an appropriate stimulus Ψ_i, the approaches (1), (2), and (3) can be recovered. Furthermore, it was shown that if Ψ is uniform in the bone, the three approaches lead to the same basic result. For more information, the reader is referred to the excellent review article by Taber [1995]. As already mentioned, all of the above methods suffer from numerical instabilities, in particular the occurrence of unphysical checkerboard patterns. Many different approaches have been tried to achieve stability. In Jacobs et al. [1995], a node-based method was introduced, which successfully suppressed the checkerboard modes for linear elements with the density held constant per volume by averaging, which is related to the *superconvergent patch recovery* method [Zienkiewicz and Zhu, 1992]. A problem related to the latter is the non-linear dependence of the bone mineral density to Young's modulus of the form

$$\frac{E}{E_0} = \left(\frac{\varrho}{\varrho_0} \right)^n , \quad E_0, \varrho_0, n \in \mathbb{R} . \tag{7.2}$$

It is easy to see that an exponent of, e.g., $n = 2$ results in intermediate densities $\varrho_{\min} \leq \varrho \leq \varrho_{\max}$ being undesired in a sense of energies. Such a formulation often generates a bone mineral density field where supporting points of the discretized bone mineral density either adopt $\varrho_{\min}$ or $\varrho_{\max}$, a result closely related to *zero-one integer programming*. Without stabilization, those formulations are strongly mesh-dependent; refinement of the mesh generates finer structures with subsequently smaller areas either adopting $\varrho_{\min}$ or $\varrho_{\max}$ instead of converging. Harrigan

and Hamilton [1992] showed the conditions under which bone remodeling with E-ϱ-relations of the form (7.2) own a stable and unique solution.
From the more recent past, two different approaches should be mentioned here as examples: Kuhl et al. [2003] and Garcia-Aznar et al. [2005]. The former models bone adaption processes built upon the theory of open thermodynamic systems, and the latter describes bone remodeling in analogy to damage mechanics.
In this thesis, the approach built upon the theory of open thermodynamic systems by Kuhl et al. [2003] is adopted. Beyond the latter, an attempt was made to model all steps in close analogy to material modeling as described in de Souza Neto et al. [2011].

7.1 The E-ϱ-relation

In numerous works, a relation between the bone mineral density and Young's modulus of cancellous bones, with the general form of equation (7.2) has been established [see, e.g., Carter and Hayes, 1977, Gibson and Ashby, 1982, Nackenhorst et al., 2000, Morgan et al., 2003]. Here, E_0, ϱ_0, and n are left to be identified by experimental investigations and physical reasoning, which is an ongoing issue in the scientific community. In Lutz [2011], the following basic material properties for the E-ϱ-relation have been proposed:

$$E_0 = 6500\,\frac{N}{mm^2}\,, \quad \varrho_0 = 1\,\frac{g}{cm^3}\,, \quad n = 2\,, \quad \text{and} \quad \varrho \in [0,2]\ \left[\frac{g}{cm^3}\right]\,. \tag{7.3}$$

It has been shown that this model fits experimental observations sufficiently and shall be used as a basis throughout this thesis.

7.2 Strain-energy density driven bone remodeling

In chapter 3, a thermodynamic consistent constitutive law describing bone remodeling has been proposed. As a result of this, the balance of mass was defined as

$$\mathrm{D}_t\,\varrho = \mathfrak{R}, \tag{7.4}$$

where $\mathfrak{R}$ is the mass source, which was left to be defined. According to the principle of thermodynamic determinism, $\mathfrak{R} = \mathfrak{R}(\varrho, \boldsymbol{\varepsilon})$ has to be a function of the state variables $\{\varrho, \boldsymbol{\varepsilon}\}$. As mentioned before, a strain-energy density driven bone remodeling approach should be adopted. Beaupré et al. [1990b] introduced a strain-energy density approach of the form

$$\mathfrak{R} = c\left(\Psi - \Psi^{\mathrm{ref}}\right)\,, \tag{7.5}$$

where

$$\Psi = \varrho\psi = \varrho\left(\frac{\varrho}{\varrho_0}\right)^n \psi^{\mathrm{LE}} \tag{7.6}$$

is the density-weighted strain-energy density for a linear elastic material restricted to small deformations (see equation 3.54)), Ψ^{ref} is a physiological target value which should be adopted by the density-weighted strain energy density, and c is an additional parameter with the unit time divided by area, which governs the speed of the bone remodeling process. Harrigan and Hamilton [1992] extended this approach

$$\mathfrak{R} = c\left(\left(\frac{\varrho}{\varrho_0}\right)^{-m}\Psi - \Psi^{\mathrm{ref}}\right) = c\left(\varrho\left(\frac{\varrho}{\varrho_0}\right)^{n-m}\psi^{\mathrm{LE}} - \Psi^{\mathrm{ref}}\right) \tag{7.7}$$

by an additional factor $(\varrho/\varrho_0)^{-m}$. By setting $m = 0$, the approach of Beaupré et al. [1990b] is recovered, while it has been shown that by choosing $m > n$, uniqueness and stability of the solution are guaranteed [Harrigan and Hamilton, 1992].

7.3 Bone remodeling as a material model

During the integration of the local stiffness matrix

$$\mathbf{K}^{e}_{(n+1)} = \int_{\mathcal{B}_e} \mathbf{B}^{\mathrm{T}}\, \bar{\tilde{\mathbb{C}}}_{(n+1)}\, \mathbf{B}\, \mathrm{d}V\,, \tag{7.8}$$

the algorithmic consistent tangent modulus is evaluated at the supporting points of the numerical integration scheme. Consequently, state variables $\{\varrho, \varepsilon\}$ are discretized and stored at the integration point level. Thus, the nature of bone remodeling only manifests itself in the material subroutine of the finite element framework.
Consider a global time-step $[t_{(n)}, t_{(n+1)}]$ and a Newton-Raphson iteration (k). At each integration point $\boldsymbol{X}_I$, the material subroutine is executed with the trial strains

$$\tilde{\boldsymbol{\varepsilon}}^{\mathrm{tr},(k)}_{(n+1)} = \hat{\boldsymbol{\varepsilon}}(\boldsymbol{X}_I, \tilde{\boldsymbol{\varepsilon}}(\boldsymbol{X}_I, t_{(n)}), \Delta\tilde{\boldsymbol{\varepsilon}}(\boldsymbol{X}_I, t_{(n)} + \sum_{i=1}^{k-1} \Delta t^{(i)})) \tag{7.9}$$

and the last converged state of the bone mineral density $\varrho_{(n)} = \varrho(\boldsymbol{X}_I, t_{(n)})$ as input arguments. By recalling that within the Newton-Raphson iteration of a time-step $[t_{(n)}, t_{(n+1)}]$ **only** the trial strains are allowed to be altered, it is clear that to obtain the iterative change in bone mineral density

$$\Delta\varrho^{(k)} = \Delta t \hat{\mathfrak{R}}(\varrho_{(n)}, \tilde{\boldsymbol{\varepsilon}}^{\mathrm{tr},(k)}_{(n+1)})\,, \tag{7.10}$$

only an evaluation of the function $\mathfrak{R}$ is necessary since the quantities $\varrho_{(n)}$ and $\tilde{\boldsymbol{\varepsilon}}^{\mathrm{tr},(k)}_{(n+1)}$ are known, and no internal Newton scheme is needed. If $\Delta\varrho^{(k)}$ is known, it is possible to determine the algorithmic consistent tangent modulus $\bar{\tilde{\mathbb{C}}}^{(k)}_{(n+1)}$. A detailed derivation of the tangent modulus can be found in section 7.4. The material subroutine is briefly summarized in Algorithm 1.

Algorithm 1 Material subroutine

1: **procedure** RESPONSE($\tilde{\boldsymbol{\varepsilon}}^{\mathrm{tr},(k)}_{(n+1)}$, $\varrho_{(n)}$)
2: $\quad\Delta\varrho^{(k)} \leftarrow \Delta t \mathfrak{R}(\varrho_{(n)}, \tilde{\boldsymbol{\varepsilon}}^{\mathrm{tr},(k)}_{(n+1)})$
3: $\quad\bar{\tilde{\mathbb{C}}}^{(k)}_{(n+1)} \leftarrow \left.\frac{\tilde{\mathbb{C}}(\varrho_{(n)}+\Delta\varrho^{(k)})}{\partial\tilde{\boldsymbol{\varepsilon}}^{*}_{(n+1)}}\right|_{\tilde{\boldsymbol{\varepsilon}}^{\mathrm{tr},(k)}_{(n+1)}} : \tilde{\boldsymbol{\varepsilon}}^{\mathrm{tr},(k)}_{(n+1)} + \tilde{\mathbb{C}}(\varrho_{(n)} + \Delta\varrho^{(k)})$
4: $\quad$**return** $(\bar{\tilde{\mathbb{C}}}^{(k)}_{(n+1)}, \Delta\varrho^{(k)})$

7.4 Algorithmic consistent tangent modulus

To achieve quadratic convergence within the Newton-Raphson scheme, it is necessary to implement the *algorithmic consistent incremental tangent modulus*

$$\bar{\tilde{\mathbb{C}}}_{(n+1)} = \frac{\partial\hat{\tilde{\boldsymbol{\sigma}}}_{(n+1)}}{\partial\tilde{\boldsymbol{\varepsilon}}_{(n+1)}}\,, \tag{7.11}$$

which can be denoted as the partial derivative of the incremental constitutive function $\partial\hat{\boldsymbol{\sigma}}_{(n+1)}$ with respect to the unknown strain $\tilde{\boldsymbol{\varepsilon}}_{(n+1)}$. Within a Newton-Raphson iteration, the above can be further specified as the *algorithmic consistent incremental iterative tangent modulus*

$$\bar{\tilde{\mathbb{C}}}^{(k)}_{(n+1)} = \left.\frac{\partial\hat{\boldsymbol{\sigma}}_{(n+1)}(\varrho_{(n)},\,\tilde{\boldsymbol{\varepsilon}}^{(k)}_{(n+1)})}{\partial\tilde{\boldsymbol{\varepsilon}}^{*}_{(n+1)}}\right|_{\tilde{\boldsymbol{\varepsilon}}^{\mathrm{tr},(k)}_{(n+1)}}, \tag{7.12}$$

the partial derivative of the *incremental iterative* constitutive function $\partial\hat{\boldsymbol{\sigma}}_{(n+1)}$ with respect to the unknown *trial* strains $\tilde{\boldsymbol{\varepsilon}}^{*}_{(n+1)}$, evaluated at the iterative trial strains $\tilde{\boldsymbol{\varepsilon}}^{\mathrm{tr},(k)}_{(n+1)} = \tilde{\boldsymbol{\varepsilon}}_{(n)} + \sum_{i=1}^{k-1}\Delta\tilde{\boldsymbol{\varepsilon}}^{(i)}$ known from the solution of the first $(k-1)$ Newton-Raphson iterations. Inserting equation (3.57) into the above and applying the chain rule yields

$$\bar{\tilde{\mathbb{C}}}^{(k)}_{(n+1)} = \left.\frac{\partial\tilde{\mathbb{C}}(\varrho_{(n)}+\Delta\varrho^{(k)})}{\partial\tilde{\boldsymbol{\varepsilon}}^{*}_{(n+1)}}\right|_{\tilde{\boldsymbol{\varepsilon}}^{\mathrm{tr},(k)}_{(n+1)}} : \tilde{\boldsymbol{\varepsilon}}^{\mathrm{tr},(k)}_{(n+1)} + \tilde{\mathbb{C}}(\varrho_{(n)}+\Delta\varrho^{(k)})\,, \tag{7.13}$$

where the partial derivative of the material tensor $\tilde{\mathbb{C}}$ with respect to the trial strains $\tilde{\boldsymbol{\varepsilon}}^{*}_{(n+1)}$ is left to be identified. A straightforward application of the rules for tensor derivations provides

$$\left.\frac{\partial\,\mathbb{C}(\varrho_{(n)}+\Delta\varrho^{(k)})}{\partial\boldsymbol{\varepsilon}^{*}_{(n+1)}}\right|_{\boldsymbol{\varepsilon}^{\mathrm{tr},(k)}_{(n+1)}} = n\varrho_0^{-n}\Delta t\cdot c\left(\frac{\varrho_{(n)}}{\varrho_0}\right)^{n-m}\boldsymbol{\sigma}^{\mathrm{LE}\,(k)}_{(n+1)}\otimes\mathbb{C}^{\mathrm{LE}}\,. \tag{7.14}$$

Note that the expressions have been converted back to tensor notation in the above since it is not trivial to multiply stresses and material tensors in Voigt notation. For more information on the algorithmic consistent tangent modulus, the reader is referred to de Souza Neto et al. [2011].

7.5 The Principle of static-equivalent forces and related biomechanical-equilibrated bone mineral density distribution

In this thesis, the assumption was made that bone remodeling is a *long-term process*, which takes place over a period of years. This justifies the omission of dynamic forces if the quantity of interest is a biomechanical-equilibrated bone mineral density distribution.
Now consider the quasi-static example for a linearized-weak form of type (4.25) for a non-linear but time-independent material: if the surface loads are held constant between two time steps $t_{(n)}$ and $t_{(n+1)}$, no Newton-Raphson iteration will take place, since the external forces $\boldsymbol{f}^{\mathrm{ext}}_{(n+1)}$ are already in balance with the internal force $\boldsymbol{f}^{\mathrm{int}}_{(n)}$. In bone remodeling, as described here, two (pseudo)-time constants were introduced: (1) Δt for the implicit Euler time integration and (2) c as a constant describing the process speed in equation (7.5). That possibly results in an out-of-balance right-hand side, although forces are held constant between two time steps. By that, it is possible to define the biomechanical-equilibrated bone mineral density distributions: assume $\boldsymbol{t} = \boldsymbol{t}(\boldsymbol{X})$ and $\varrho = \varrho(\boldsymbol{X})$ are a given surface load and a given bone mineral density distribution, respectively. $\varrho(\boldsymbol{X})$ is called biomechanical-equilibrated with respect to $\boldsymbol{t}$, if $\boldsymbol{\sigma}_{(n+1)} = \boldsymbol{\sigma}_{(n)}$ for $\boldsymbol{t}_{(n+1)} = \boldsymbol{t}_{(n)} = \boldsymbol{t}$.
It is noted here that, albeit unconditionally stable for many problems, the time discretization constant Δt in the backward Euler method cannot be chosen to be arbitrarily large for the Newton-Raphson procedure to converge.

What remains is a meaningful defintion of $\boldsymbol{t}$: in Lutz and Nackenhorst [2007] surface loads were computed by solving the inverse optimization problem

$$\min_{\boldsymbol{t}} \frac{1}{2} \sum_{I=1}^{\mathrm{n_{elems}}} \left(\varrho(\boldsymbol{X}_I, \boldsymbol{\varepsilon}) - \varrho^{\mathrm{ref}}(\boldsymbol{X}_I)\right)^2 , \tag{7.15}$$

where $\varrho^{\mathrm{ref}}(\boldsymbol{X}_I)$ has been obtained by projecting 3D-CT data from a human femur to an associated finite element mesh.

7.6 Numerical examples

All methods described in this chapter were implemented within a self-developed framework, written in the **julia** language [Bezanson et al., 2017]. In this section, some numerical examples shall demonstrate the function of the bone remodeling algorithm as well as its implementation. The first example is a thin plate where the variation of the parameter m shall be investigated. The second example is a human femur where the influence of the reference strain energy Ψ^{ref} is studied.
For both examples following assumptions are made: To define the bone material, the parameters introduced in equation (7.3) are used. Furthermore, Poisson's ratio is set to $\nu = 0.3$ and a combined parameter $\Delta t \cdot c = 100\,\mathrm{s} \cdot 1\,\mathrm{s/m^2} = 1\ \mathrm{s^2/mm^2}$ is used for controlling the speed of the adaption process. The force is held constant, and the maximum number of global time-steps is $(n_{\max}) = 120$. The algorithm is said to have converged if for some time-step $1 < k \leq n$: $|\varrho_{(k)}(\boldsymbol{X}_I) - \varrho_{(k-1)}(\boldsymbol{X}_I)| < \epsilon_{\mathrm{tol}}$ for all integration points $\boldsymbol{X}_I$. All results are transferred to X-ray images according to chapter 6.

7.6.1 Model 1: thin plate

As a first example, a thin three-dimensional plate with dimensions of 20cm × 20cm × 1cm is clamped on its left-hand side, and a shear force $q_y(y) = 1$ kN/mm, 9cm $\leq y \leq$ 11cm is applied at the right-hand side as displayed in figure 7.1. The reference strain-energy density is set

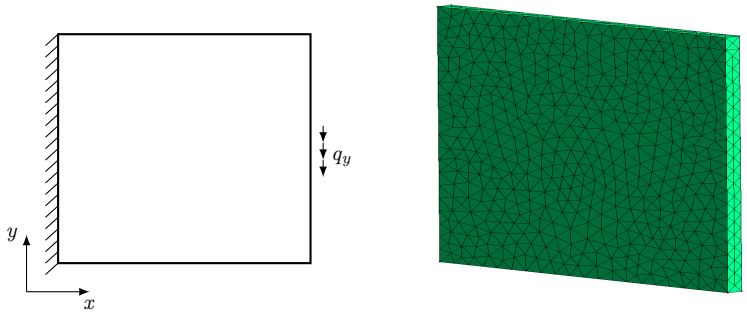

Figure 7.1: Thin plate model: schematic representation (left) and sample discretization (right).

to $\Psi^{\mathrm{ref}} = 10^{-3}\ \mathrm{N/mm^2}$. The exponent m is varied to study the influence of this parameter. The results of an X-ray simulation of the thin plate following the bone remodeling process are displayed in figure 7.3 for linear finite elements and in 7.4 for quadratic finite elements.

Linear finite elements. The thin plate model meshed by linear tetrahedron results in a mesh with 709 elements and 816 degrees of freedom by choosing a coarse discretization scheme or, if a finer discretization scheme is applied, in a mesh with 3081 elements and 3267 degrees of freedom.
For the exponent $m = 1$, it can be seen that a strong *checkerboarding* pattern occurs for both discretizations, the coarse one displayed in figure 7.3a and the finer one displayed in figure 7.3b. Therefore, the convergence of the global algorithm is not achieved, while quadratic convergence of the Newton-Raphson method is preserved, as shown in figure 7.2. While the exponent m increases, the bone mineral density distribution is getting smoother, as seen by comparing 7.3c and 7.3e or 7.3d and 7.3f, respectively, but unphysical checkerboard patterns are not fully suppressed. As all the results exhibit unphysical *checkerboard* patterns, it can be said that linear finite elements are not suitable to perform bone remodeling simulations without further treatment of the instabilities with the methods described here.

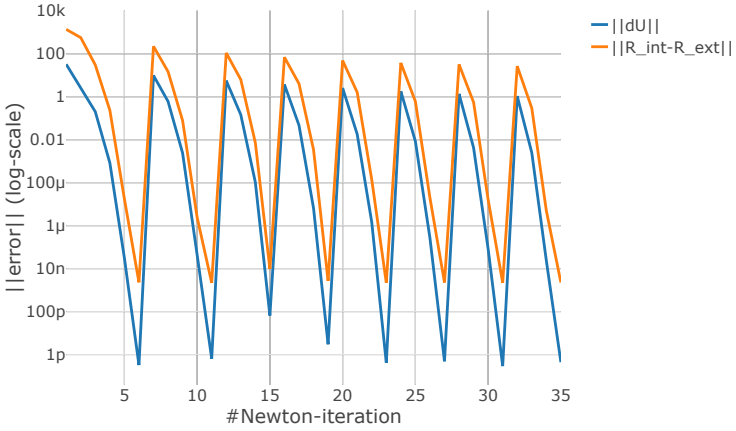

Figure 7.2: Convergence history of bone remodeling material model.

Quadratic finite elements. The thin plate model meshed by quadratic tetrahedrons results in a mesh with 709 elements and 4566 degrees of freedom by choosing a coarse discretization scheme or, if a finer discretization scheme is applied, in a mesh with 3081 elements and 19032 degrees of freedom. For simulations with $m = 1$ (not depicted), convergence of the global algorithm was not achieved, and unphysical patterns could be seen. For $m = 2$, the same unphysical patterns occur but are less prominent, and convergence of the global algorithm was achieved in 29 time-steps for the coarse mesh, depicted in figure 7.4a, and in 59 steps for the finer mesh, depicted in figure 7.4b. The case with exponent $m = 3$ is the first where no unphysical patterns are visible. In figure 7.4c, disturbances can be seen near the bearing and force application, but these phenomenons disappear if the mesh is refined, as seen in figure 7.4b. It can be observed that while m increases, global convergence is improved, in general. The Newton-Raphson scheme preserved quadratic convergence throughout all experiments, as shown for the linear elements in figure 7.2.

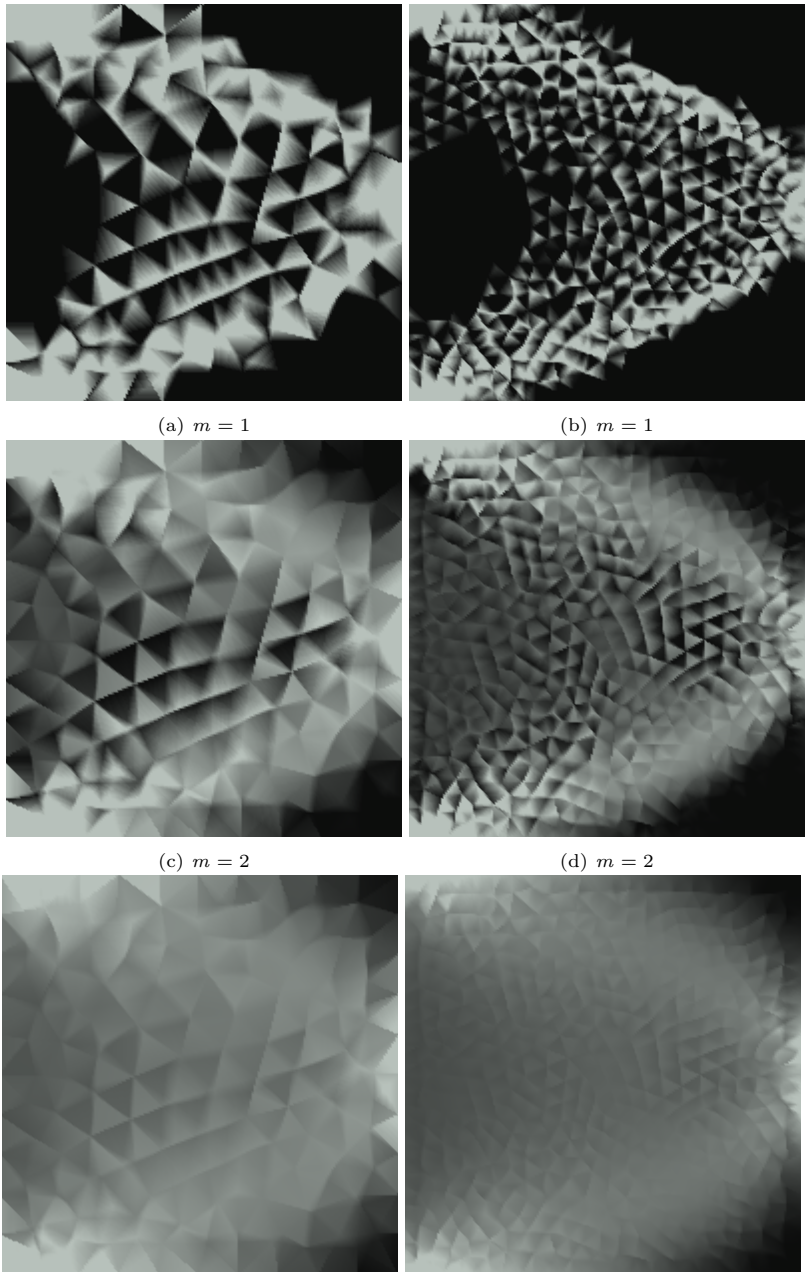

(a) $m = 1$ (b) $m = 1$

(c) $m = 2$ (d) $m = 2$

(e) $m = 3$ (f) $m = 3$

Figure 7.3: Bone remodeling followed by X-ray simulation of thin plate model meshed by linear tetrahedral elements. (a), (c), and (e) are derived from the coarse mesh; (b), (d), and (e) from the finer mesh.

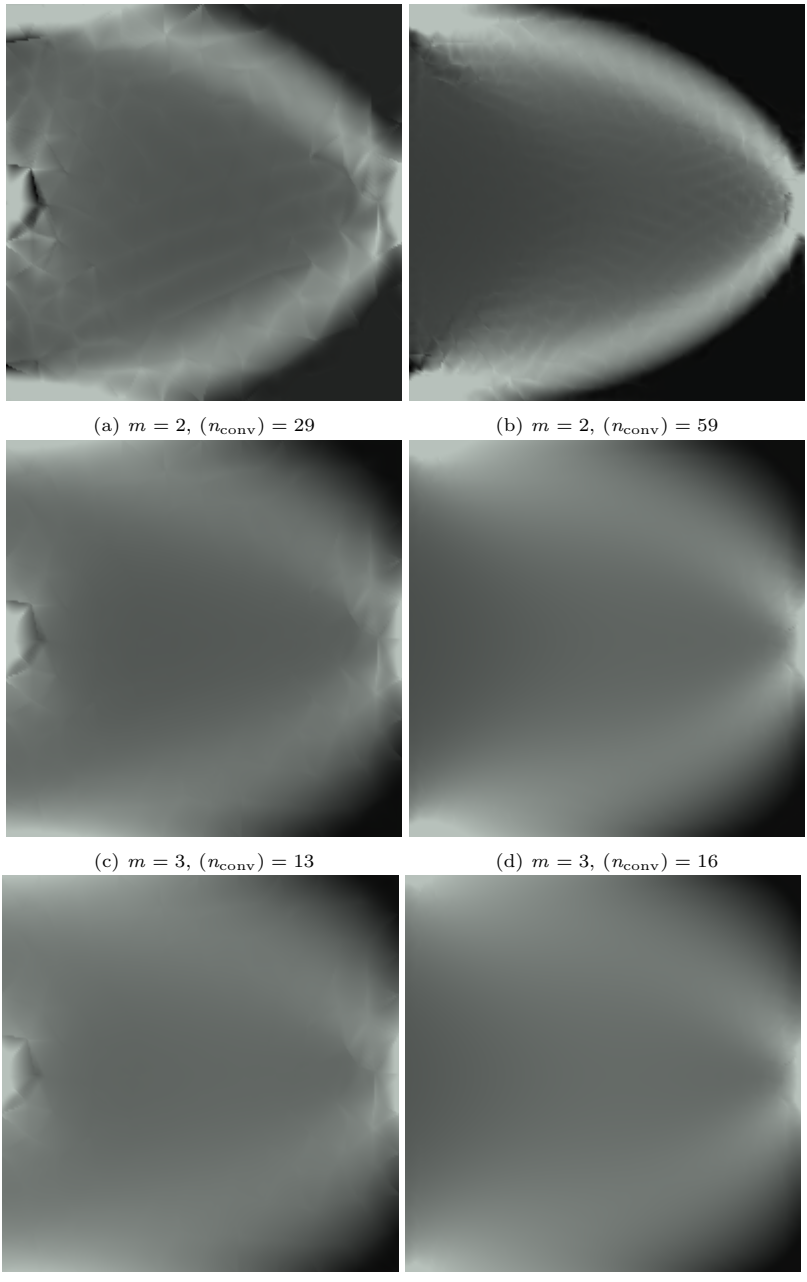

(a) $m = 2$, $(n_{\mathrm{conv}}) = 29$ (b) $m = 2$, $(n_{\mathrm{conv}}) = 59$

(c) $m = 3$, $(n_{\mathrm{conv}}) = 13$ (d) $m = 3$, $(n_{\mathrm{conv}}) = 16$

(e) $m = 4$, $(n_{\mathrm{conv}}) = 11$ (f) $m = 4$, $(n_{\mathrm{conv}}) = 11$

Figure 7.4: Bone remodeling followed by X-ray simulation of thin plate model meshed by quadratic tetrahedral elements. (a), (c), and (e) are derived from the coarse mesh; (b), (d), and (f) from the finer mesh.

7.6.2 Example 2: human femur

The human femur, displayed in figure 7.5, serves as a second example. Since linear finite elements did not perform sufficiently in the last example, the model is meshed solely by quadratic elements resulting in 21451 elements and 102048 degrees of freedom. For the depicted boundary conditions, which were adopted from Lutz and Nackenhorst [2007], it has already been shown that they are suitable to generate a physiological density distribution. The exponent m is set

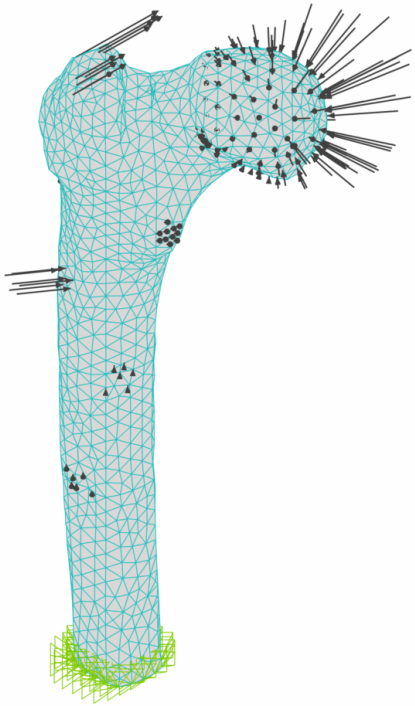

Figure 7.5: Finite element model of human femur with boundary conditions.

to $m = 2$, while in this example, the reference strain energy density is altered in order to study its influence. The results are transferred to an X-ray image and depicted in figure 7.6. In figure 7.6a, it can be seen that $\Psi^{\text{ref}} = 0.00001\ \text{N/mm}^2$ is too small as a reference strain energy density and leads to a bone mineral density distribution that is nearly uniform and doesn't develop visible zones of compact and cancellous bone. Increasing Ψ^{ref} leads to a bone mineral density distribution which can be considered more realistic as seen in figure 7.6b or, with even more prominent developed zones with compact and cancellous bone, in figure 7.6c. In figure 7.6d, it can be concluded that $\Psi^{\text{ref}} = 0.001\ \text{N/mm}^2$ is possibly too large since especially in the region of the femoral head, the bone mineral density seems to be underdeveloped. By that, it can be concluded that $0.0005\,\text{N/mm}^2 \leq \Psi^{\text{ref}} < 0.001\,\text{N/mm}^2$ can be considered an optimal reference strain energy concering the given model and boundary conditions. Finally, it can be noted that for this example, the Newton-Raphson algorithm preserved quadratic convergence for all cases considered here, and the global algorithm has converged in less than 20 time-steps.

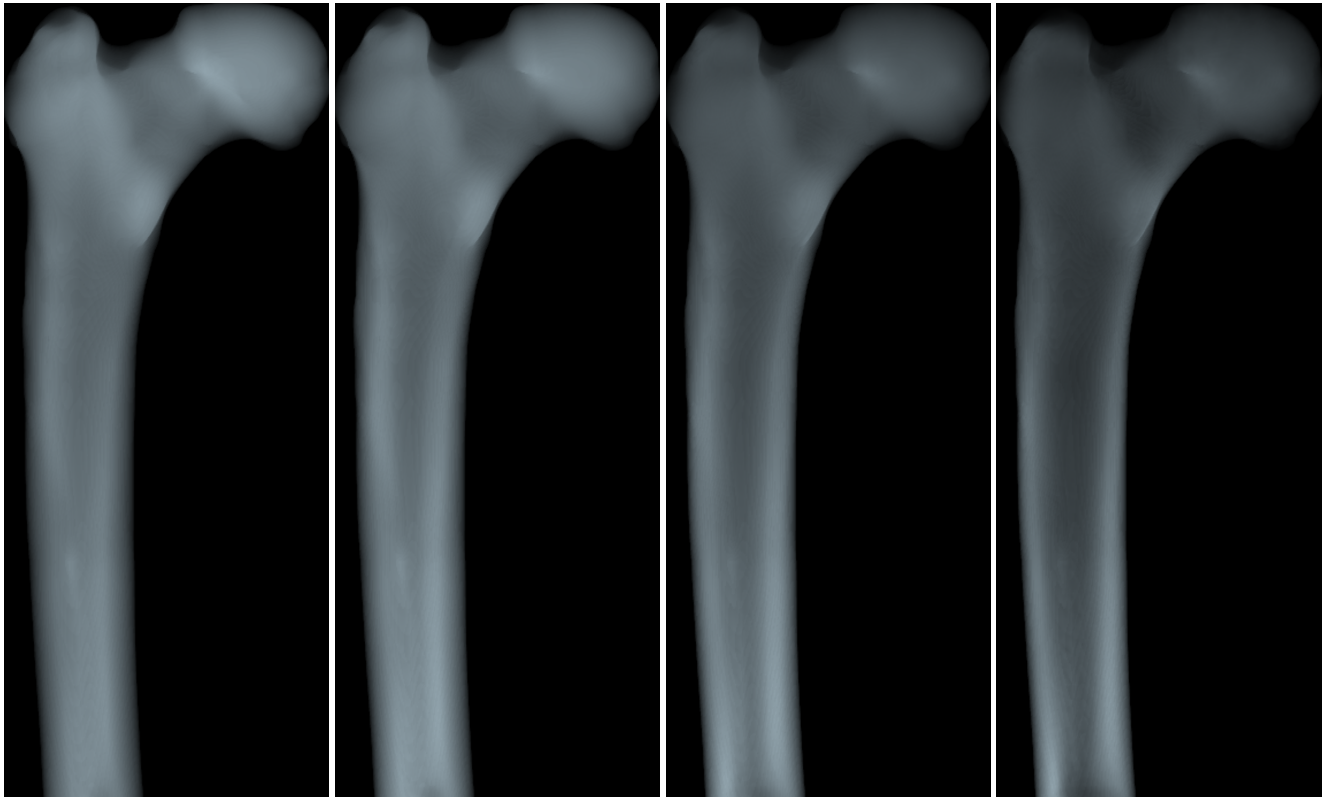

(a) $\Psi^{\text{ref}} = 0.00001\ {}^{\text{N}}/_{\text{mm}^2}$ (b) $\Psi^{\text{ref}} = 0.0001\ {}^{\text{N}}/_{\text{mm}^2}$ (c) $\Psi^{\text{ref}} = 0.0005\ {}^{\text{N}}/_{\text{mm}^2}$ (d) $\Psi^{\text{ref}} = 0.001\ {}^{\text{N}}/_{\text{mm}^2}$

Figure 7.6: Bone remodeling followed by X-ray simulation of a human femur with different reference strain energy densities Ψ^{ref}.

Chapter 8

Numerical simulation of osseointegration: a node-to-node contact interface approach

Simulating the process of osseointegration remains a challenge in biomechanical research. A reason for this is that there is little knowledge available about the process of osseointegration since it is hard to observe *in vivio*. As a result, only a few computational models are available. A first approach using finite element analysis is given in Natali et al. [1997], by which the process of osseointegration of dental implants was investigated by analyzing the dynamic response following impulse excitation. Moreo et al. [2007] provided a more elaborate attempt by modeling the bone-implant interface following the principles of continuum damage mechanics. This model was capable of reproducing osseointegration patterns that agreed with clinical observations qualitatively. Finally, a bio-active interface, analogous to modeling plasticity, is given in Lutz and Nackenhorst [2012]. Here, the bony ingrowth is depicted with a Drucker-Prager plasticity model, which merges into a von Mises model while osseointegration takes place.

8.1 Objectives of this approach

Medical researchers agree that micromotions are a driving factor for the process of osseointegration [see, e.g., Munzinger et al., 2004]. Furthermore, osseointegration is a process closely related to fracture healing or bone remodeling [see, e.g., Parithimarkalaignan and Padmanabhan, 2013]. Consequently, it seems quite natural to combine the strain-energy density driven approach from chapter 7 with a physically admissible *micro-motion threshold*.
To be able to display micro-motions, it is necessary to capture the relative kinematics of bone and prosthesis accurately. Thus, the introduction of an interface that allows for relative displacement of bone and prosthesis is required. A contact interface can naturally do this best. Despite this, it may be exhibiting various other problems in terms of numerical stability, algorithmic consistency, and the implementation of an evolutionary constitutive relation within the interface. However, most of these problems are solved by the simple restriction to small displacements in the interface, which fits well within the frame of the rest of this thesis. By that restriction, it is possible to model the contact as *node-to-node* contact. Hereby, the interface is introduced artificially by duplicating nodes of the finite element discretization, which are shared between the volume parts of bone and prosthesis. In the literature, this is also known as a *zero-thickness* contact element [see, e.g., Goodman et al., 1968, Day and Potts, 1994, Gaul and Mayer, 2008, Cerfontaine et al., 2015]. A zero-thickness interface seems to be physically favorable compared to previous approaches where the interface was realized with a thin layer of volume elements, since in locations where the interface exhibits compressive stresses, the bloody-bone-mixture by which the prosthesis is covered post-surgically is almost completely displaced, resulting in direct contact of bone and prosthesis in reality.

8.2 Multi-body weak form

Let $\mathcal{B}_0 = \mathcal{B}_0^1 \bigcup \mathcal{B}_0^2 \bigcup \partial\mathcal{B}_0^{\mathrm{c}}$ be a deformable body embedded in $\mathbb{R}^3$ with distinct regions $\mathcal{B}_0^1$ and $\mathcal{B}_0^2$ (see figure 8.1). We denote $\mathcal{B}_0^1$ the master body and $\mathcal{B}_0^2$ the slave body. The interface layer connecting $\mathcal{B}_0^1$ and $\mathcal{B}_0^2$ is termed $\partial\mathcal{B}_0^{\mathrm{c}}$ with associated boundary parts $\partial\mathcal{B}_0^{\mathrm{c},1} \subset \partial\mathcal{B}_0^1$ and $\partial\mathcal{B}_0^{\mathrm{c},2} \subset \partial\mathcal{B}_0^2$ (see figure 8.2). The interface allows for small relative displacements of $\mathcal{B}_0^1$ and $\mathcal{B}_0^2$ and the specification of a user-defined interface constitutive relation. The multi-body weak form, neglecting body forces, can then be stated as follows:

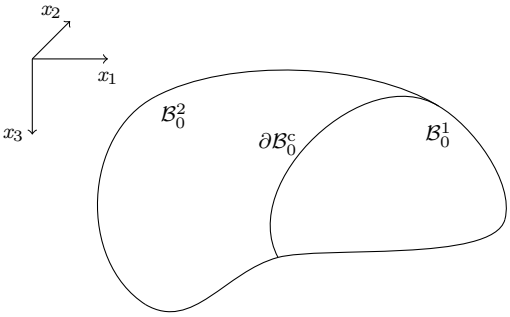

Figure 8.1: Deformable body $\mathcal{B}_0$.

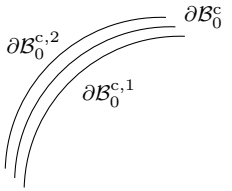

Figure 8.2: Interface layer $\partial\mathcal{B}_0^{\mathrm{c}}$.

$$\delta\Pi(\boldsymbol{u}^1, \boldsymbol{u}^2) = \sum_{\alpha=1}^{2} \left[\int_{\mathcal{B}_0^\alpha} \delta\left(\boldsymbol{\varepsilon}^\alpha : \boldsymbol{\sigma}(\boldsymbol{\varepsilon}^\alpha)\right) \mathrm{d}V - \int_{\partial\mathcal{B}_0^\alpha} \delta\boldsymbol{u}^\alpha \cdot \boldsymbol{t}^\alpha \, \mathrm{d}A \right] . \tag{8.1}$$

For each body, the surface contributions

$$\delta\Pi^{\partial\mathcal{B}_0} = \sum_{\alpha=1}^{2} \left[- \int_{\partial\mathcal{B}_0^\alpha} \delta\boldsymbol{u}^\alpha \cdot \boldsymbol{t}^\alpha \, \mathrm{d}A \right] \tag{8.2}$$

$$= \sum_{\alpha=1}^{2} \left[- \int_{\partial\mathcal{B}_0^\alpha \setminus \partial\mathcal{B}_0^{\mathrm{c},\alpha}} \delta\boldsymbol{u}^\alpha \cdot \boldsymbol{t}^{\alpha,\mathrm{ext}} \, \mathrm{d}A - \int_{\partial\mathcal{B}_0^{\mathrm{c},\alpha}} \delta\boldsymbol{u}^\alpha \cdot \boldsymbol{C}^\alpha \, \mathrm{d}A \right] \tag{8.3}$$

can be divided into a part accounting for surface tractions $\boldsymbol{t}^{\alpha,\mathrm{ext}}$ on $\partial\mathcal{B}_0^\alpha \setminus \partial\mathcal{B}_0^{\mathrm{c},\alpha}$ and a part accounting for interface tractions $\boldsymbol{C}^\alpha$ on $\partial\mathcal{B}_0^{\mathrm{c},\alpha}$. Since this approach is restricted to the geometric linear case and allows only for small relative displacements, it can be stated that

$$\partial\mathcal{B}_0^{\mathrm{c}} \subseteq \partial\mathcal{B}_0^{\mathrm{c},1} \subseteq \partial\mathcal{B}_0^{\mathrm{c},2} \subseteq \partial\mathcal{B}_0^{\mathrm{c}} , \tag{8.4}$$

which allows integration of the surface tractions over the master body $\partial\mathcal{B}_0^{\mathrm{c},1}$. In the following, the terms master boundary $\partial\mathcal{B}_0^{\mathrm{c},1}$ and interface layer $\partial\mathcal{B}_0^{\mathrm{c}}$ will be used synonymously. By

writing out solely the interface tractions

$$\delta\Pi^C = -\int_{\partial\mathcal{B}_0^c} \delta\boldsymbol{u}^1 \cdot \boldsymbol{C}^1 \,\mathrm{d}A - \int_{\partial\mathcal{B}_0^c} \delta\boldsymbol{u}^2 \cdot \boldsymbol{C}^2 \,\mathrm{d}A\,, \tag{8.5}$$

and enforcing mechanical equilibrium within the interface

$$\boldsymbol{C}\,\mathrm{d}A = -\boldsymbol{C}^1\,\mathrm{d}A = \boldsymbol{C}^2\,\mathrm{d}A\,, \tag{8.6}$$

the interface contribution to the total virtual work can be stated as

$$-\int_{\partial\mathcal{B}_0^c} \delta\boldsymbol{u}^1 \cdot \boldsymbol{C}^1 \,\mathrm{d}A - \int_{\partial\mathcal{B}_0^c} \delta\boldsymbol{u}^2 \cdot \boldsymbol{C}^2 \,\mathrm{d}A = -\int_{\partial\mathcal{B}_0^c} \left(\delta\boldsymbol{u}^2 - \delta\boldsymbol{u}^1\right) \cdot \boldsymbol{C}\,\mathrm{d}A\,. \tag{8.7}$$

Subsequently, the interface tractions

$$-\int_{\partial\mathcal{B}_0^c} \left(\delta\boldsymbol{u}^2 - \delta\boldsymbol{u}^1\right) \cdot \boldsymbol{C}\,\mathrm{d}A = -\int_{\partial\mathcal{B}_0^c} \left(\delta\boldsymbol{u}^2 - \delta\boldsymbol{u}^1\right) \cdot \left(\boldsymbol{C}_\mathrm{N} + \boldsymbol{C}_\mathrm{T}\right)\,\mathrm{d}A \tag{8.8}$$

may be split into their normal parts $\boldsymbol{C}_\mathrm{N}$ and their tangential parts $\boldsymbol{C}_\mathrm{T}$. Here it is emphasized that the subindices N and T only indicate the normal and tangential contribution, and no summation is implied if they appear twice in an expression coincidentally.

8.3 Non-penetration condition in the interface: the normal gap function

In order to allow relative displacement but suppress interpenetration of $\partial\mathcal{B}_0^{c,1}$ and $\partial\mathcal{B}_0^{c,2}$, the non-penetration condition

$$\left(\boldsymbol{x}^2 - \bar{\boldsymbol{x}}^1\right) \cdot \bar{\boldsymbol{n}}_\mathrm{N}^1 \geq 0 \tag{8.9}$$

has to be fulfilled for each pair $(\boldsymbol{x}^2, \bar{\boldsymbol{x}}^1)$, where $\boldsymbol{x}^2 \in \partial\mathcal{B}_0^{c,2}$ is a material point on the slave surface, and $\bar{\boldsymbol{x}}^1 \in \partial\mathcal{B}_0^{c,1}$ is its related point on the master surface. If $\boldsymbol{\xi}^1 = (\xi_1, \xi_2)$ denotes the parametrization of $\partial\mathcal{B}_0^{c,1}$, in a general approach, the point $\bar{\boldsymbol{x}}^1 = \boldsymbol{x}^1(\bar{\boldsymbol{\xi}})$ can be found by solving the closest point projection problem, for example, providing the minimizing parameters $\bar{\boldsymbol{\xi}}$. Here, since a *node-to-node* approach is used, the pair $(\boldsymbol{x}^2, \bar{\boldsymbol{x}}^1)$ is known a priori at the nodes $(\hat{\boldsymbol{x}}_i^2, \hat{\bar{\boldsymbol{x}}}_i^1)$ of the finite element discretization of the interface and can provide for the definition of a nodal gap $\hat{\boldsymbol{g}}_i = \hat{\boldsymbol{x}}_i^2 - \hat{\bar{\boldsymbol{x}}}_i^1$, as seen in figure 8.3. This leads to the definition of an interpolatory gap function

$$\boldsymbol{g}(\boldsymbol{x}^2, \boldsymbol{x}^1, \boldsymbol{\xi}) = \sum_{i=1}^{n_\mathrm{nodes}} N_i(\boldsymbol{\xi})\, \hat{\boldsymbol{g}}_i(\hat{\boldsymbol{x}}_i^2, \hat{\bar{\boldsymbol{x}}}_i^1)\,, \tag{8.10}$$

where $N_i(\boldsymbol{\xi})$ is the i-th shape function of the element. Furthermore, the normals $\hat{\boldsymbol{n}}_i$ have to be defined at the nodes of the interface to guarantee continuity over element borders. The associated surface normal $\bar{\boldsymbol{n}}_\mathrm{N}^1 = \boldsymbol{n}_\mathrm{N}^1(\bar{\boldsymbol{\xi}})$ can be defined as

$$\boldsymbol{n}_\mathrm{N}(\boldsymbol{\xi}) = \boldsymbol{n}_\mathrm{N}^1(\boldsymbol{\xi}) = \sum_{i=1}^{n_\mathrm{nodes}} N_i(\boldsymbol{\xi})\, \hat{\boldsymbol{n}}_i\,. \tag{8.11}$$

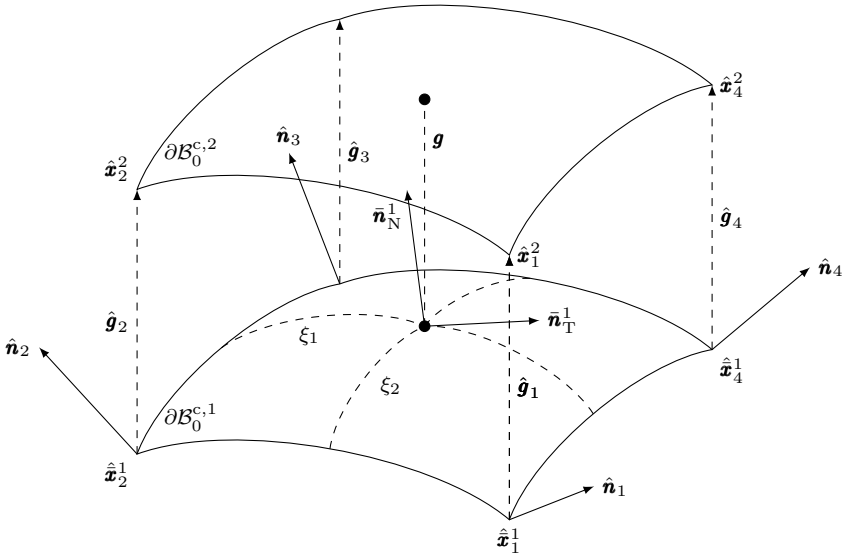

Figure 8.3: Interpolatory gap function $\boldsymbol{g}$ defined by slave material points $\hat{\boldsymbol{x}}_i^2$ and related master material points $\hat{\bar{\boldsymbol{x}}}_i^1$.

This provides for a redefinition of the normal gap function given in (8.9) as

$$\boldsymbol{g}(\boldsymbol{x}^2, \boldsymbol{x}^1, \boldsymbol{\xi}) \cdot \boldsymbol{n}_N(\boldsymbol{\xi}) \geq 0\,. \tag{8.12}$$

$\boldsymbol{x}^\alpha$ is stated in the current configuration and can be expressed as $\boldsymbol{x}^\alpha = \boldsymbol{x}^\alpha + \boldsymbol{u}^\alpha$, where $\boldsymbol{x}^\alpha$ relates to the initial configuration and $\boldsymbol{u}^\alpha$ denotes the displacement field. In the initial configuration, it can be stated that $\boldsymbol{x}^2(\boldsymbol{\xi}) = \boldsymbol{x}^1(\boldsymbol{\xi})$. From this it follows

$$\begin{aligned} \boldsymbol{g}\left(\boldsymbol{x}^2, \boldsymbol{x}^1, \boldsymbol{\xi}\right) \cdot \boldsymbol{n}_N(\boldsymbol{\xi}) &= \boldsymbol{g}\left(\boldsymbol{x}^2 + \boldsymbol{u}^2, \boldsymbol{x}^1 - \boldsymbol{u}^1, \boldsymbol{\xi}\right) \cdot \boldsymbol{n}_N(\boldsymbol{\xi}) && (8.13)\\ &= \boldsymbol{g}\left(\boldsymbol{u}^2, \boldsymbol{u}^1, \boldsymbol{\xi}\right) \cdot \boldsymbol{n}_N(\boldsymbol{\xi})\,, && (8.14) \end{aligned}$$

since $\boldsymbol{g}$ is a linear function, which leads to the definition of the so-called normal gap function

$$g_N(\boldsymbol{g}, \boldsymbol{\xi}) = g_N(\boldsymbol{u}^2, \boldsymbol{u}^1, \boldsymbol{\xi}) = \boldsymbol{g}(\boldsymbol{u}^2, \boldsymbol{u}^1, \boldsymbol{\xi}) \cdot \boldsymbol{n}_N(\boldsymbol{\xi}). \tag{8.15}$$

Finally, the contact indicator function

$$g_N^-(\boldsymbol{g}, \boldsymbol{\xi}) = \begin{cases} g_N(\boldsymbol{g}, \boldsymbol{\xi}) & \text{if } g_N < 0\,, \\ 0 & \text{else} \end{cases} \tag{8.16}$$

is introduced, which takes negative values if the non-penetration condition (8.9) is violated and is zero in the case of no contact.

8.4 Relative displacement in the interface: the tangential gap function

A projector onto the tangential space can be defined as

$$\boldsymbol{a}_\alpha(\boldsymbol{\xi}) \otimes \boldsymbol{a}_\alpha(\boldsymbol{\xi}) = \mathbf{I} - \boldsymbol{n}_\mathrm{N}(\boldsymbol{\xi}) \otimes \boldsymbol{n}_\mathrm{N}(\boldsymbol{\xi})\,, \tag{8.17}$$

which leads to the definition of the tangential gap vector

$$\boldsymbol{g}_\mathrm{T}(\boldsymbol{g}, \boldsymbol{\xi}) = \boldsymbol{g}_\mathrm{T}(\boldsymbol{u}^2, \boldsymbol{u}^1, \boldsymbol{\xi}) = \boldsymbol{g}\left(\boldsymbol{u}^2, \boldsymbol{u}^1, \boldsymbol{\xi}\right) \cdot \left(\boldsymbol{a}_\alpha(\boldsymbol{\xi}) \otimes \boldsymbol{a}_\alpha(\boldsymbol{\xi})\right)\,. \tag{8.18}$$

The tangential gap function

$$g_\mathrm{T}(\boldsymbol{g}, \boldsymbol{\xi}) = ||\boldsymbol{g}_\mathrm{T}(\boldsymbol{g}, \boldsymbol{\xi})|| \tag{8.19}$$

is then just the norm of the tangential gap vector. Finally, a slip-normal

$$\boldsymbol{n}_\mathrm{T}(\boldsymbol{g}, \boldsymbol{\xi}) = \frac{\boldsymbol{g}_\mathrm{T}(\boldsymbol{g}, \boldsymbol{\xi})}{||\boldsymbol{g}_\mathrm{T}(\boldsymbol{g}, \boldsymbol{\xi})||} = \frac{\boldsymbol{g}_\mathrm{T}(\boldsymbol{g}, \boldsymbol{\xi})}{g_\mathrm{T}(\boldsymbol{g}, \boldsymbol{\xi})} \tag{8.20}$$

can be defined, pointing in the direction of the tangential displacement.

8.5 An approach towards a thermodynamical consistent osseointegration contact interface

The osseointegration degree

$$\rho = \rho(\boldsymbol{X}, t)\,, \quad \boldsymbol{X} \in \partial\mathcal{B}_0^\mathrm{c}\,, \rho \in [0, 1] \tag{8.21}$$

is introduced as a dimensionless scalar field to depict the process of osseointegration within the contact interface. If $\rho = 0$, no osseointegration has taken place, and the interface solely transmits compressive stresses. If $\rho = 1$, osseointegration has taken place to the full extent, and a firm bond exists between prosthesis and bone. The definition of a linear function represents the increase of adhesive strength during the process of osseointegration.

$$c(\rho) = c_0 + \rho \cdot c_\rho\,. \tag{8.22}$$

This provides for the definition of the constitutive normal gap function as

$$g_\mathrm{N}^c(\rho, \boldsymbol{g}) = \begin{cases} g_\mathrm{N}(\boldsymbol{g}) & \text{if } g_\mathrm{N}(\boldsymbol{g}) < c(\rho) - r\,, \\ c(\rho) - \frac{1}{2}r & \text{if } g_\mathrm{N}(\boldsymbol{g}) > c(\rho)\,, \\ -\frac{1}{2}r \cdot \left(\frac{g_\mathrm{N}(\boldsymbol{g}) - c(\rho)}{r}\right)^2 + c(\rho) - \frac{1}{2}r & \text{else,} \end{cases} \tag{8.23}$$

which will be used in the following instead of g_N, resulting in an adhesive behavior of the interface depending on ρ. Hereby $r \leq c_0$ is a regularization parameter. Furthermore, a constitutive version of Coulomb's law of friction

$$|\boldsymbol{C}_\mathrm{T}| \leq \mu(\rho)\,|\boldsymbol{C}_\mathrm{N}| \tag{8.24}$$

shall be satisfied in the interface. Hereby, the linear function

$$\mu(\rho) = \mu_0 + \rho \cdot \mu_\rho \tag{8.25}$$

represents the increase in static friction during the process of osseointegration. In order to fulfill Coulomb's law of friction implicitly, a constitutive tangential gap function

$$g_{\mathrm{T}}^{\mu}(\rho, \boldsymbol{g}) = \begin{cases} \mu(\rho)\,|g_{\mathrm{N}}^{c}| & \text{if } g_{\mathrm{T}} > \mu(\rho)\,|g_{\mathrm{N}}^{c}|\,, \\ g_{\mathrm{T}} & \text{else} \end{cases} \tag{8.26}$$

is defined. Using (8.23) and (8.67), the gap function

$$\boldsymbol{g} = g_{\mathrm{N}}^{c}\boldsymbol{n}_{\mathrm{N}} + g_{\mathrm{T}}^{\mu}\boldsymbol{n}_{\mathrm{T}} + \boldsymbol{g}^{\mathrm{p}} = \boldsymbol{g}_{\mathrm{N}}^{\mathrm{e}} + \boldsymbol{g}_{\mathrm{T}}^{\mathrm{e}} + \boldsymbol{g}^{\mathrm{p}} = \boldsymbol{g}^{\mathrm{e}} + \boldsymbol{g}^{\mathrm{p}} \tag{8.27}$$

can be split into an *elastic* part $\boldsymbol{g}^{\mathrm{e}}$ and a *plastic* part $\boldsymbol{g}^{\mathrm{p}}$. Similar to section 3.5.1, it will be assumed that the set of state variables

$$\{\rho, \boldsymbol{g}, \boldsymbol{g}^{\mathrm{p}}\} \tag{8.28}$$

determines the thermodynamical state for any time t at a point $\boldsymbol{X} \in \partial\mathcal{B}_0^{\mathrm{c}}$.

8.5.1 Dissipation inequality for contact interfaces

Following Laursen [2013] and Dittmann [2017], it is possible to extend the Helmholtz specific free energy

$$\bar{\psi} = \psi(\varrho, \boldsymbol{\varepsilon}) + \psi^{\mathrm{C}}(\rho, \boldsymbol{g}) = \psi(\varrho, \boldsymbol{\varepsilon}) + \psi^{\mathrm{C_e}}(\rho, \boldsymbol{g}^{\mathrm{e}}) + \psi^{\mathrm{C_p}}(\rho, \boldsymbol{g}^{\mathrm{p}}) \tag{8.29}$$

in the presence of a contact interface by an interface part $\psi^{\mathrm{C}}(\rho, \boldsymbol{g}^{\mathrm{e}})$, which depends on the osseointegration state ρ and the gap vector $\boldsymbol{g}$. Furthermore, an interface version of the Clausius-Duhem inequality, stated in equation 3.46, can be formulated as

$$d^{\mathrm{C,loc}} = -\boldsymbol{C} \cdot \mathrm{D}_t\boldsymbol{g}^{\mathrm{e}} - \rho \mathrm{D}_t\psi^{\mathrm{C}} - \rho(S^{\mathrm{C}} + \mathrm{D}_\theta\psi^{\mathrm{C}}) - \mathcal{S}^{\mathrm{C}}\theta \geq 0\,, \tag{8.30}$$

where S^{C} is the entropy in the interface and $\mathcal{S}^{\mathrm{C}}$ is the additional interface entropy source due to the theory of open systems thermodynamics. The negative sign in the first term was introduced artificially since the gap vector $\boldsymbol{g}$ and the interface tractions $\boldsymbol{C}$ point in opposite directions by construction. For more information about interface balance laws, the reader is referred to Laursen [2013].

8.5.2 An osseointegration constitutive interface-model

Analogous to section 3.5, the time derivative of the interface Helmholtz specific energy function can be stated as

$$\mathrm{D}_t\psi^{\mathrm{C}}(\rho, \boldsymbol{g}) = \partial_\rho\psi^{\mathrm{C}}\,\mathrm{D}_t\rho + \partial_{\boldsymbol{g}^{\mathrm{e}}}\psi^{\mathrm{C_e}} \cdot \mathrm{D}_t\boldsymbol{g}^{\mathrm{e}} + \partial_{\boldsymbol{g}^{\mathrm{p}}}\psi^{\mathrm{C_p}} \cdot \mathrm{D}_t\boldsymbol{g}^{\mathrm{p}}\,. \tag{8.31}$$

Furthermore, an interface evolution law can be stated in close analogy to (3.29) as

$$\mathrm{D}_t\rho = \mathfrak{R}^{\mathrm{C}}\,. \tag{8.32}$$

Inserting equation (8.31) and (8.32) into (3.29) yields

$$\begin{aligned} d^{\mathrm{C,loc}} = {} & (\boldsymbol{C} - \rho\partial_{\boldsymbol{g}^{\mathrm{e}}}\psi^{\mathrm{C_e}}) \cdot \mathrm{D}_t\boldsymbol{g}^{\mathrm{e}} - \rho\partial_\rho\psi^{\mathrm{C}}\mathfrak{R}^{\mathrm{C}} - \rho(S^{\mathrm{C}} + \mathrm{D}_\theta\psi^{\mathrm{C}}) - \mathcal{S}^{\mathrm{C}}\theta \\ & - \rho\partial_{\boldsymbol{g}^{\mathrm{p}}}\psi^{\mathrm{C_p}} \cdot \mathrm{D}_t\boldsymbol{g}^{\mathrm{p}} \geq 0\,, \end{aligned} \tag{8.33}$$

from which the constitutive equations

$$\begin{cases} \psi^{\mathrm{C}} = \psi^{\mathrm{C}}(\rho, \boldsymbol{g}^{\mathrm{e}}) \\ \boldsymbol{C} = -\rho \partial_{\boldsymbol{g}^{\mathrm{e}}} \psi^{\mathrm{C}} \\ \mathrm{D}_t \rho = \mathfrak{R}^{\mathrm{C}} \\ |\boldsymbol{C}_{\mathrm{T}}| \leq \mu(\rho)\, |\boldsymbol{C}_{\mathrm{N}}| \\ \mathcal{S}^{\mathrm{C}} = \frac{1}{\theta} \rho \partial_{\rho} \psi^{\mathrm{C}} \mathfrak{R}^{\mathrm{C}} \\ -\rho \partial_{\boldsymbol{g}^{\mathrm{P}}} \psi^{\mathrm{C}_{\mathrm{P}}} \cdot \mathrm{D}_t \boldsymbol{g}^{\mathrm{P}} \geq 0 \end{cases} \tag{8.34}$$

can be derived. Furthermore, $S^{\mathrm{C}} = \mathrm{D}_{\theta} \psi^{\mathrm{C}} = 0$ was implied since no actual heat generation takes place in this model. By that procedure, thermodynamical consistency is guaranteed *a priori*. Finally, the constitutive *initial value problem for osseointegration interfaces* can be stated as follows: presuming the history of the gap function $\boldsymbol{g}(t)$, $t \in [t_0, T]$, the initial value of the osseointegration degree $\varrho(t_0)$, and the plastic gap vector $\boldsymbol{g}^{\mathrm{P}}(t_0)$ are known, find the history of $\boldsymbol{C}(t)$, $\varrho(t)$, and $\boldsymbol{g}^{\mathrm{P}}(t)$, such that the constitutive equations

$$\begin{cases} \boldsymbol{C}(t) = \rho(t)\, \partial_{\boldsymbol{g}^{\mathrm{e}}} \psi^{\mathrm{C_e}}(\rho(t), \boldsymbol{g}^{\mathrm{e}}(t)) \\ \mathrm{D}_t \rho(t) = \mathfrak{R}^{\mathrm{C}}(\rho(t), \boldsymbol{g}^{\mathrm{e}}(t)) \\ |\boldsymbol{C}_{\mathrm{T}}(t)| \leq \mu(\rho(t))\, |\boldsymbol{C}_{\mathrm{N}}(t)| \end{cases} \tag{8.35}$$

hold for every $t \in [t_{(0)}, T]$.

8.5.3 Evolution law for osseointegration contact interfaces

Similar to bone remodeling, a predefined reference strain energy density $\psi^{\mathrm{C_e}}_{\mathrm{ref}}$ is adopted by the interface. The rate of change of degree of osseointegration can be defined as follows

$$\mathrm{D}_t \rho = \mathfrak{R}^{\mathrm{C}}(\rho, \boldsymbol{g}, \boldsymbol{g}^{\mathrm{P}}) = k \cdot \left(\frac{\ln(\psi^{\mathrm{C_e}}_{\mathrm{ref}})}{\ln(S_2(||\boldsymbol{g}^{\mathrm{P}}||) \cdot \psi^{\mathrm{C_e}})} - 1 \right), \tag{8.36}$$

where k is an auxiliary parameter governing the speed of the adaption process, and S_2 is an indicator function for the admissible plastic displacements in the interface, as seen in figure 8.4. Osseointegration shall only take place if the relative displacement is in an admissible range $[g^{\mathrm{P}}_{\mathrm{min}}, g^{\mathrm{P}}_{\mathrm{max}}]$ with an optimum at $g^{\mathrm{P}}_{\mathrm{opt}} = (g^{\mathrm{P}}_{\mathrm{min}} + g^{\mathrm{P}}_{\mathrm{max}})/2$. Therefore, the admissible tangential slip indicator function

$$S_2(g^{\mathrm{P}} = ||\boldsymbol{g}^{\mathrm{P}}||) = \begin{cases} S_2^*(s(g^{\mathrm{P}}, g^{\mathrm{P}}_{\mathrm{min}}, g^{\mathrm{P}}_{\mathrm{opt}})) & \text{if } g^{\mathrm{P}}_{\mathrm{min}} < g^{\mathrm{P}} \leq g^{\mathrm{P}}_{\mathrm{opt}}\,, \\ S_2^*(s(g^{\mathrm{P}}, g^{\mathrm{P}}_{\mathrm{opt}}, g^{\mathrm{P}}_{\mathrm{max}})) & \text{if } g^{\mathrm{P}}_{\mathrm{opt}} < g^{\mathrm{P}} \leq g^{\mathrm{P}}_{\mathrm{max}}\,, \\ 0 & \text{else} \end{cases} \tag{8.37}$$

is defined with the help of the so-called *smootherstep*-function

$$S_2^*(x) = 6x^5 - 15x^4 + 10x^3 \tag{8.38}$$

and a linear scaling function

$$s(x, a, b) = \frac{1}{b-a}\, x + \frac{a}{a-b}\,. \tag{8.39}$$

An implicit Euler scheme

$$\mathrm{D}_t \rho = \frac{\rho_{n+1} - \rho_n}{\Delta t} \tag{8.40}$$

discretizes time integration of (8.36)

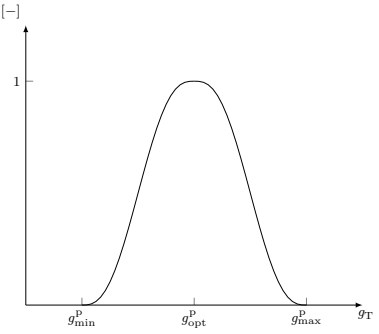

Figure 8.4: Admissible tangential slip indicator function S_2

8.5.4 The specific interface Helmholtz free energy function

For the osseointegration interface, a specific interface Helmholtz free energy function is chosen as

$$\psi^{\mathrm{Ce}}(\rho, \boldsymbol{g}^{\mathrm{e}}) = \frac{\varepsilon_{\mathrm{p}}}{2\rho}(\boldsymbol{g}^{\mathrm{e}})^{\mathrm{T}}(\boldsymbol{g}^{\mathrm{e}}) = \frac{\varepsilon_{\mathrm{p}}}{2\rho}(\boldsymbol{g} - \boldsymbol{g}^{\mathrm{p}})^{\mathrm{T}}(\boldsymbol{g} - \boldsymbol{g}^{\mathrm{p}})\,, \tag{8.41}$$

with a penalty parameter ε_{p} from which the interface tractions can be derived as

$$\boldsymbol{C} = \boldsymbol{C}_{\mathrm{N}} + \boldsymbol{C}_{\mathrm{T}} = -\rho\partial_{\boldsymbol{g}^{\mathrm{e}}}\psi^{\mathrm{Ce}} = -\varepsilon_{\mathrm{p}}\,\boldsymbol{g}^{\mathrm{e}} = -\varepsilon_{\mathrm{p}}(\boldsymbol{g} - \boldsymbol{g}^{\mathrm{p}})\,. \tag{8.42}$$

It is remarked that with the introduction of the penalty parameter ε_{p}, the non-penetration condition is only fulfilled approximatively.

8.6 The interface tractions $\boldsymbol{C}_{\mathrm{N}}$

The weak form of the normal part of the interface traction is given by

$$\delta\Pi^{\mathrm{C_N}} = -\int_{\partial\mathcal{B}^{\mathrm{c}}_0} \delta\boldsymbol{g}\cdot\boldsymbol{C}_{\mathrm{N}}\,\mathrm{d}A\,. \tag{8.43}$$

To derive the normal interface traction, the interface Helmholtz free energy can be written as

$$\begin{aligned}\psi^{\mathrm{Ce}}(\rho, \boldsymbol{g}^{\mathrm{e}}) &= \frac{\varepsilon_{\mathrm{p}}}{2\rho}(\boldsymbol{g}^{\mathrm{e}})^{\mathrm{T}}(\boldsymbol{g}^{\mathrm{e}}) = \left(\frac{\varepsilon_{\mathrm{p}}}{2\rho}(g^{c}_{\mathrm{N}}\boldsymbol{n}_{\mathrm{N}} + g^{\mu}_{\mathrm{T}}\boldsymbol{n}_{\mathrm{T}})^{\mathrm{T}}(g^{c}_{\mathrm{N}}\boldsymbol{n}_{\mathrm{N}} + g^{\mu}_{\mathrm{T}}\boldsymbol{n}_{\mathrm{T}})\right)\\ &= \frac{\varepsilon_{\mathrm{p}}}{2\rho}\left((g^{c}_{\mathrm{N}}\boldsymbol{n}_{\mathrm{N}})^{\mathrm{T}}(g^{c}_{\mathrm{N}}\boldsymbol{n}_{\mathrm{N}}) + (g^{\mu}_{\mathrm{T}}\boldsymbol{n}_{\mathrm{T}})^{\mathrm{T}}(g^{\mu}_{\mathrm{T}}\boldsymbol{n}_{\mathrm{T}})\right)\,,\end{aligned} \tag{8.44}$$

since $\boldsymbol{n}_{\mathrm{N}}\cdot\boldsymbol{n}_{\mathrm{T}} = 0$. The partial derivative of the interface Helmholtz free energy can identify the normal contact traction with respect to the elastic normal gap vector as

$$\boldsymbol{C}_{\mathrm{N}} = -\rho\partial_{\boldsymbol{g}^{\mathrm{e}}_{\mathrm{N}}}\psi^{\mathrm{Ce}} = -\varepsilon_{\mathrm{p}}\,g^{c}_{\mathrm{N}}\boldsymbol{n}_{\mathrm{N}}\,. \tag{8.45}$$

With the above the normal contact pressure can be identified as

$$P^{c}_{\mathrm{N}} = -\varepsilon_{\mathrm{p}}\cdot g^{\mathrm{c}}_{\mathrm{N}}\,. \tag{8.46}$$

In figure (8.5), the contact pressure P^{c}_{N} is shown for different degrees of osseointegration, illustrating the desired behavior in the interface.

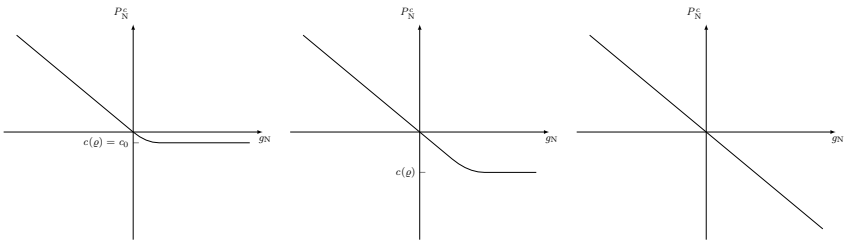

Figure 8.5: Contact pressure $P_{\mathrm{N}}^{\mathrm{c}}$ for different degrees of osseointegration.

8.7 The interface tractions $\boldsymbol{C}_{\mathbf{T}}$

The tangential part of the interface traction is given by:

$$\delta\Pi^{\mathrm{C_T}} = -\int_{\partial\mathcal{B}_0^{\mathrm{c}}} \delta\boldsymbol{g} \cdot \boldsymbol{C}_{\mathrm{T}}\, \mathrm{d}A\,. \tag{8.47}$$

Similar to the normal interface tractions, a vector-valued elastic tangental gap function $\boldsymbol{g}_{\mathrm{N}}^{\mathrm{e}} =$

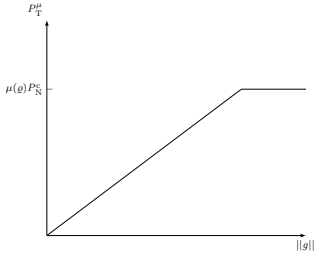

Figure 8.6: Tangential contact pressure P_{T}^{μ}.

$g_{\mathrm{T}}^{\mu}\boldsymbol{n}_{\mathrm{T}}$ is defined. Consequently, the tangential contact tractions can be derived by the partial derivative of the interface Helmholtz free energy with respect to the elastic tangential gap vector as

$$\boldsymbol{C}_{\mathrm{T}} = -\rho\partial_{\boldsymbol{g}_{\mathrm{T}}^{\mathrm{e}}}\psi^{\mathrm{C_e}} = -\varepsilon_{\mathrm{P}}\, g_{\mathrm{T}}^{\mu}\boldsymbol{n}_{\mathrm{T}}\,. \tag{8.48}$$

In figure 8.6, the tangential contact pressure

$$P_{\mathrm{T}}^{\mu} = -\varepsilon_{\mathrm{P}} \cdot g_{\mathrm{T}}^{\mu} \tag{8.49}$$

is displayed.

8.8 Material non-linearities

The initial boundary value problem for osseointegration contact interfaces

$$\begin{cases} \delta\Pi^{\mathrm{C}}(\rho(t), \boldsymbol{g}^{\mathrm{e}}(t)) & = 0 \\ \Phi_{\rho}(\rho(t), \boldsymbol{g}^{\mathrm{e}}(t)) & = 0 = \mathrm{D}_t\rho(t) - \mathfrak{R}^{\mathrm{C}}(\rho(t), \boldsymbol{g}^{\mathrm{e}}(t)) \\ \Phi_{\boldsymbol{g}^{\mathrm{e}}}(\rho(t), \boldsymbol{g}^{\mathrm{e}}(t)) & = 0 = \boldsymbol{g}^{\mathrm{e}}(t) - g^{c}_{\mathrm{N}}(\rho(t), \boldsymbol{g}(t))\boldsymbol{n}_{\mathrm{N}} - g^{\mu}_{\mathrm{T}}(\rho(t), \boldsymbol{g}(t))\boldsymbol{n}_{\mathrm{T}} \end{cases} \tag{8.50}$$

can be stated as the fulfillment of (1) the weak form contribution of the interface $\delta\Pi = 0$, (2) the evolution law for osseointegration interfaces $\Phi_{\rho} = 0$, and (3) retrieving the elastic gap function by $\Phi_{\boldsymbol{g}^{\mathrm{e}}} = \boldsymbol{0}$. Therefore, an incremental evolution law

$$\rho_{(n+1)} = \rho_{(n)} + \Delta t \hat{\mathfrak{R}}^{\mathrm{C}}(\rho_{(n)}, \boldsymbol{g}^{\mathrm{e}}_{(n+1)}) = \rho_{(n)} + \Delta\rho \tag{8.51}$$

and an incremental elastic law

$$\begin{aligned} \boldsymbol{g}^{\mathrm{e}}_{(n+1)} &= \hat{\boldsymbol{g}}^{\mathrm{e}}(\rho_{(n)} + \Delta\rho, \boldsymbol{g}^{*}_{(n+1)}) \\ &= g^{c}_{\mathrm{N}}(\rho_{(n)} + \Delta\rho, \boldsymbol{g}^{*}_{(n+1)})\boldsymbol{n}_{\mathrm{N}} + g^{\mu}_{\mathrm{T}}(\rho_{(n)} + \Delta\rho, \boldsymbol{g}^{*}_{(n+1)})\boldsymbol{n}_{\mathrm{T}} \end{aligned} \tag{8.52}$$

can be defined to solve this generally non-linear problem within the global Newton-Raphson iteration. In the above, the implicit Euler scheme, introduced in (8.40), was used, and a trial gap $\boldsymbol{g}^{*}_{(n+1)} = \boldsymbol{g}_{(n)} - \boldsymbol{g}^{\mathrm{p}}_{(n)} + \Delta\boldsymbol{g}$ has been defined. Note that the incremental mass source $\hat{\mathfrak{R}}^{\mathrm{C}}$ and the incremental elastic gap function $\hat{\boldsymbol{g}}^{\mathrm{e}}$ only exhibit variation in $\boldsymbol{g}$. The interface tractions can then be identified as

$$\boldsymbol{C}_{(n+1)} = -\varepsilon_{\mathrm{p}}\, \hat{\boldsymbol{g}}^{\mathrm{e}}(\rho_{(n)} + \Delta\rho, \boldsymbol{g}^{*}_{(n+1)})\,. \tag{8.53}$$

Finally, the resultant weak form contribution of the osseointegration contact interface can be stated as

$$\delta\Pi^{\mathrm{C}}_{(n+1)} = -\int_{\partial\mathcal{B}^{c}_{0}} \delta\boldsymbol{g} \cdot \boldsymbol{C}_{(n+1)}\, \mathrm{d}A\,. \tag{8.54}$$

8.9 Linearization of the interface contributions

Similarly to section 4.3, the contribution of the contact interface to the equations arising from the linearization of (8.1) can be written as

$$\delta\Pi^{\mathrm{C}}_{(n+1)} = \delta\Pi^{\mathrm{C}}(\boldsymbol{g}_{(n+1)}) \approx \delta\Pi^{\mathrm{C}}(\rho_{(n)}, \boldsymbol{g}^{\mathrm{p}}_{(n)}, \boldsymbol{g}_{(n)}) + \Delta\delta\Pi^{\mathrm{C}}(\rho_{(n)}, \boldsymbol{g}^{\mathrm{p}}_{(n)}, \boldsymbol{g}_{(n)}, \Delta\boldsymbol{g})\,. \tag{8.55}$$

The first variation $\delta\Pi^{\mathrm{C}} = \delta\Pi^{\mathrm{C_N}} + \delta\Pi^{\mathrm{C_T}}$ is given in (8.43) and (8.47), respectively. The second variation of the normal interface contributions

$$\Delta\delta\Pi^{\mathrm{C}} = -\int_{\partial\mathcal{B}^{c}_{0}} \Delta\delta\boldsymbol{g} \cdot \boldsymbol{C}\, \mathrm{d}A - \int_{\partial\mathcal{B}^{c}_{0}} \delta\boldsymbol{g} \cdot \Delta\boldsymbol{C}\, \mathrm{d}A \tag{8.56}$$

can be simplified to

$$\Delta\delta\Pi^{\mathrm{C}} = -\int_{\partial\mathcal{B}^{c}_{0}} \delta\boldsymbol{g} \cdot \Delta\boldsymbol{C}\, \mathrm{d}A = \varepsilon_{\mathrm{p}} \int_{\partial\mathcal{B}^{c}_{0}} \delta\boldsymbol{g} \cdot \Delta\hat{\boldsymbol{g}}^{\mathrm{e}}(\rho_{(n)} + \Delta\rho, \boldsymbol{g}^{*}_{(n+1)})\, \mathrm{d}A\,, \tag{8.57}$$

due to the fact that the second variation $\Delta\delta\boldsymbol{g}$ of the gap function vanishes.

8.9.1 First variation $\delta \boldsymbol{g}$ of the gap function

Due to the defintion (8.10) of $\boldsymbol{g}$ in terms of shape functions, the first variation of the gap function is simply

$$\delta \boldsymbol{g}(\boldsymbol{u}^2, \boldsymbol{u}^1, \boldsymbol{\xi}) = \sum_{i=1}^{n_{\text{nodes}}} N_i(\boldsymbol{\xi})\, \delta \hat{\boldsymbol{g}}_i(\hat{\boldsymbol{u}}_i^2, \hat{\boldsymbol{u}}_i^1) = \sum_{i=1}^{n_{\text{nodes}}} N_i(\boldsymbol{\xi})\, \left(\delta \hat{\boldsymbol{u}}_i^2 - \delta \hat{\boldsymbol{u}}_i^1\right) . \tag{8.58}$$

8.9.2 Linearization Δg_{N} of the normal gap function

To find the first variation Δg_{N} of the normal gap given in (8.15), the chain rule can be stated as

$$\Delta g_{\mathrm{N}} = \boldsymbol{n}_{\mathrm{N}} \Delta \boldsymbol{g} + \boldsymbol{g} \Delta \boldsymbol{n}_{\mathrm{N}} . \tag{8.59}$$

Since $\boldsymbol{n}_{\mathrm{N}}$ is held constant, only the term $\boldsymbol{n}_{\mathrm{N}} \Delta \boldsymbol{g}$ needs to be derived. The variation of $\Delta \boldsymbol{g}$ is known from equation (8.58), hence the first variation of the normal gap function is given by

$$\Delta g_{\mathrm{N}} = \boldsymbol{n}_{\mathrm{N}}\, \Delta \boldsymbol{g} . \tag{8.60}$$

8.9.3 Linearization Δg_{T} of the tangential gap function

The first variation of the tangential gap function given in (8.19) is stated as

$$\Delta g_{\mathrm{T}} = \Delta \left(||\boldsymbol{g}_{\mathrm{T}}|| \right) = \frac{\boldsymbol{g}_{\mathrm{T}}}{||\boldsymbol{g}_{\mathrm{T}}||}\, \Delta \boldsymbol{g}_{\mathrm{T}} = \boldsymbol{n}_{\mathrm{T}}\, \Delta \boldsymbol{g}_{\mathrm{T}} . \tag{8.61}$$

8.9.4 Linearization $\Delta \boldsymbol{g}_{\mathrm{T}}$ of the tangential gap vector.

The tangential projector $\boldsymbol{a}_\alpha(\boldsymbol{\xi}) \otimes \boldsymbol{a}_\alpha(\boldsymbol{\xi})$ exhibits no variation because it is defined by the normal vector $\boldsymbol{n}_{\mathrm{N}}$, hence

$$\Delta \boldsymbol{g}_{\mathrm{T}} = \Delta \left(\boldsymbol{a}_\alpha(\boldsymbol{\xi}) \otimes \boldsymbol{a}_\alpha(\boldsymbol{\xi})\, \boldsymbol{g} \right) = \left(\boldsymbol{a}_\alpha(\boldsymbol{\xi}) \otimes \boldsymbol{a}_\alpha(\boldsymbol{\xi}) \right) \Delta \boldsymbol{g} . \tag{8.62}$$

8.9.5 Linearization $\Delta \boldsymbol{n}_{\mathrm{T}}$ of the slip normal.

In contrast to $\boldsymbol{n}_{\mathrm{N}}$, the slip normal does vary with changes in $\boldsymbol{g}$ and therefore needs to be linearized. It can be found by the following derivation:

$$\begin{aligned}
\Delta \boldsymbol{n}_{\mathrm{T}} &= \frac{\partial \boldsymbol{n}_{\mathrm{T}}}{\partial \boldsymbol{g}^*_{(n+1)}} \Delta \boldsymbol{g} = \Delta \left(\frac{\boldsymbol{g}_{\mathrm{T}}}{||\boldsymbol{g}_{\mathrm{T}}||} \right) = \frac{\Delta \boldsymbol{g}_{\mathrm{T}}}{||\boldsymbol{g}_{\mathrm{T}}||} + \Delta(||\boldsymbol{g}_{\mathrm{T}}||)^{-1} \boldsymbol{g}_{\mathrm{T}} \\
&= \frac{\Delta \boldsymbol{g}_{\mathrm{T}}}{||\boldsymbol{g}_{\mathrm{T}}||} - \frac{1}{2}\, (\boldsymbol{g}_{\mathrm{T}} \cdot \boldsymbol{g}_{\mathrm{T}})^{-3/2}\, \Delta \left(\boldsymbol{g}_{\mathrm{T}} \cdot \boldsymbol{g}_{\mathrm{T}} \right) \boldsymbol{g}_{\mathrm{T}} \\
&= \frac{\Delta \boldsymbol{g}_{\mathrm{T}}}{||\boldsymbol{g}_{\mathrm{T}}||} - \frac{(\boldsymbol{g}_{\mathrm{T}} \otimes \boldsymbol{g}_{\mathrm{T}})\, \Delta \boldsymbol{g}_{\mathrm{T}}}{||\boldsymbol{g}_{\mathrm{T}}||^3} = \frac{\Delta \boldsymbol{g}_{\mathrm{T}}}{||\boldsymbol{g}_{\mathrm{T}}||} - \frac{(\boldsymbol{n}_{\mathrm{T}} \otimes \boldsymbol{n}_{\mathrm{T}})\, \Delta \boldsymbol{g}_{\mathrm{T}}}{||\boldsymbol{g}_{\mathrm{T}}||} \\
&= \frac{\mathbb{I} - (\boldsymbol{n}_{\mathrm{T}} \otimes \boldsymbol{n}_{\mathrm{T}})}{||\boldsymbol{g}_{\mathrm{T}}||}\, \left(\boldsymbol{a}_\alpha(\boldsymbol{\xi}) \otimes \boldsymbol{a}_\alpha(\boldsymbol{\xi}) \right) \Delta \boldsymbol{g} .
\end{aligned} \tag{8.63}$$

8.9.6 Linearization $\Delta g^{\mathrm{c}}_{\mathrm{N}}$ of the constitutive normal gap function

Recalling the trial gap $\boldsymbol{g}^{*}_{(n+1)} = \boldsymbol{g}^{\mathrm{e}}_{(n)} + \Delta\boldsymbol{g}$ and defining a trial osseointegration state $\rho^{*} = \rho_{(n)} + \Delta\rho$, the incremental constitutive normal gap can be derived as

$$\Delta g^{c}_{\mathrm{N}} = \frac{\partial g^{c}_{\mathrm{N}}}{\partial \boldsymbol{g}^{*}_{(n+1)}} \Delta\boldsymbol{g} \tag{8.64}$$

the partial derivative of g^{c}_{N} with respect to the trial gap $\boldsymbol{g}^{*}_{(n+1)}$. Here, the partial derivative of the constitutive normal gap can be stated as

$$\frac{\partial g^{c}_{\mathrm{N}}}{\partial \boldsymbol{g}^{*}_{(n+1)}} = \begin{cases} (\boldsymbol{n}_{\mathrm{N}})^{\mathrm{T}} & \text{if } g_{\mathrm{N}}(\boldsymbol{g}^{*}_{(n+1)}) < c(\rho^{*}) - r\,, \\ 0 \cdot (\boldsymbol{n}_{\mathrm{N}})^{\mathrm{T}} & \text{if } g_{\mathrm{N}}(\boldsymbol{g}^{*}_{(n+1)}) > c(\rho^{*})\,, \\ \frac{-(g_{\mathrm{N}}(\boldsymbol{g}^{*}_{(n+1)}) - c(\rho^{*}))}{r} (\boldsymbol{n}_{\mathrm{N}})^{\mathrm{T}} & \text{else}\,. \end{cases} \tag{8.65}$$

8.9.7 Linearization $\Delta g^{\mu}_{\mathrm{T}}$ of the constitutive tangential gap function

The linearization of the constitutive tangential gap can be stated as

$$\Delta g^{\mu}_{\mathrm{T}} = \frac{\partial g^{\mu}_{\mathrm{T}}}{\partial \boldsymbol{g}^{*}_{(n+1)}} \Delta\boldsymbol{g} \tag{8.66}$$

the partial derivative of g^{μ}_{T} with respect to the trial gap $\boldsymbol{g}^{*}_{(n+1)}$. In the latter, the partial derivative can be expressed as follows:

$$\frac{\partial g^{\mu}_{\mathrm{T}}}{\partial \boldsymbol{g}^{*}_{(n+1)}} = \begin{cases} \mu(\rho^{*}) \frac{g^{c}_{\mathrm{N}}(\rho^{*}, \boldsymbol{g}^{*}_{(n+1)})}{|g^{c}_{\mathrm{N}}(\rho^{*}, \boldsymbol{g}^{*}_{(n+1)})|} \frac{\partial g^{c}_{\mathrm{N}}}{\partial \boldsymbol{g}^{*}_{(n+1)}} & \text{if } g_{\mathrm{T}}(\boldsymbol{g}^{*}_{(n+1)}) > \mu(\rho^{*})\,|g^{c}_{\mathrm{N}}(\rho^{*}, \boldsymbol{g}^{*}_{(n+1)})|\,, \\ (\boldsymbol{n}_{\mathrm{T}}(\boldsymbol{g}^{*}_{(n+1)}))^{\mathrm{T}} (\boldsymbol{a}_{\alpha} \otimes \boldsymbol{a}_{\alpha}) & \text{else}\,. \end{cases} \tag{8.67}$$

8.9.8 Linearization $\Delta \boldsymbol{C}$ of the interface tractions and resultant weak form contribution

Equations for $\boldsymbol{C}$ and $\hat{\boldsymbol{g}}^{\mathrm{e}}$ are given in (8.53) and (8.52), respectively. A straightforward application of derivation rules yields the linearization of the interface tractions as

$$\Delta \boldsymbol{C} = -\varepsilon_{\mathrm{p}}\, \Delta\hat{\boldsymbol{g}}^{\mathrm{e}} = -\varepsilon_{\mathrm{p}} (\boldsymbol{n}^{1}_{\mathrm{N}} \Delta g^{c}_{\mathrm{N}} + \boldsymbol{n}^{1}_{\mathrm{T}} \Delta g^{\mu}_{\mathrm{T}} + g^{\mu}_{\mathrm{T}} \Delta \boldsymbol{n}^{1}_{\mathrm{T}}) \tag{8.68}$$

$$= -\varepsilon_{\mathrm{p}} \underbrace{(\boldsymbol{n}^{1}_{\mathrm{N}} \frac{\partial g^{c}_{\mathrm{N}}}{\partial \boldsymbol{g}^{*}_{(n+1)}} + \boldsymbol{n}^{1}_{\mathrm{T}} \frac{\partial g^{\mu}_{\mathrm{T}}}{\partial \boldsymbol{g}^{*}_{(n+1)}} + g^{\mu}_{\mathrm{T}} \frac{\partial \boldsymbol{n}_{\mathrm{T}}}{\partial \boldsymbol{g}^{*}_{(n+1)}})}_{=:\, \mathfrak{C}_{(n+1)}} \Delta\boldsymbol{g} \tag{8.69}$$

$$= -\varepsilon_{\mathrm{p}}\, \mathfrak{C}_{(n+1)}\, \Delta\boldsymbol{g}\,, \tag{8.70}$$

where $\mathfrak{C}_{(n+1)}$ is a 3×3-matrix. Concluding the above, the contribution of the contact interface to the linearized weak form, can be stated as

$$\delta\Pi^{\mathrm{C}}_{(n+1)} = \varepsilon_{\mathrm{p}} \int_{\partial\mathcal{B}^{c}_{0}} \delta\boldsymbol{g} \cdot \mathfrak{C}_{(n+1)}\, \Delta\boldsymbol{g}\, \mathrm{d}A + \varepsilon_{\mathrm{p}} \int_{\partial\mathcal{B}^{c}_{0}} \delta\boldsymbol{g} \cdot \boldsymbol{g}^{\mathrm{e}}_{(n)}\, \mathrm{d}A\,. \tag{8.71}$$

8.10 Discretization

In the following, the discretization strategy to the osseointegration interface is stated. The overall model is discretized with 10-node quadratic tetrahedral elements, the interface is solely described for quadratic triangular elements. Still, all the definitions made below could be altered for arbitrary finite element formulations.

8.10.1 Zero-thickness contact elements

To implement zero-thickness contact elements [Goodman et al., 1968], nodes shared between the volume part of the bone and the volume part of the prosthesis are selected, and subsequently, these nodes are artificially duplicated. This procedure results in the creation of a new element

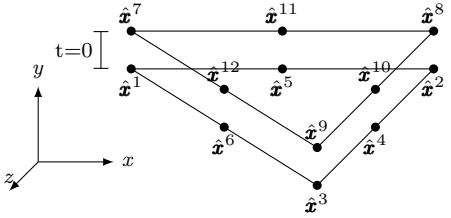

Figure 8.7: A triangular zero-thickness contact element.

that consists out of two parallel triangular faces with a distance of $t = 0$ cm, as can be seen in figure 8.7. As mentioned before, this simple procedure could be done with arbitrary element types.

8.10.2 Definition of the contact normals

From equation (8.11), it is evident that the normals have to be defined at the nodal positions. It is noted that there exist different methods for the definition of normals at nodal positions. For example, Wriggers and Zavarise [2004] propose a smooth spline interpolation of the contact surfaces. By that, it is possible to derive *smoothed* normals at the nodes. For simplicity, in this

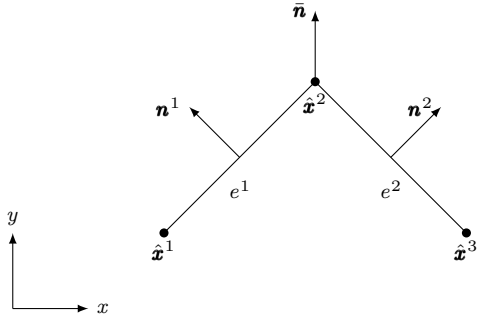

Figure 8.8: Average interface normal.

approach, vertex normals are derived by the weighted average of the normals at all integration points $\boldsymbol{X}_I$ of all adjacent elements e_i, $i = 1, ..., n_{\mathrm{adj}}$ to a node $\hat{\boldsymbol{x}}^j$ as

$$\hat{\boldsymbol{n}}^j = \frac{\sum_{i=1}^{n_{\mathrm{adj}}} \sum_{I=1}^{n_{\mathrm{ip}}} w_I \cdot \boldsymbol{n}(\boldsymbol{X}_I)}{\sum_{i=1}^{n_{\mathrm{adj}}} \sum_{I=1}^{n_{\mathrm{ip}}} w_I}\,, \tag{8.72}$$

with the weights

$$w_I = \frac{1}{||\hat{\boldsymbol{x}}^j - \boldsymbol{X}_I||} \tag{8.73}$$

being defined as the inverse of the distance between a node $\hat{\boldsymbol{x}}^j$ and a integration point $\boldsymbol{X}_I$. An exemplary illustration of an average vertex normal is displayed in figure 8.8.

8.10.3 Discretized weak form contribution of the osseointegration interface

As a first step, the zero-thickness element displacement vector is introduced as

$$\hat{\tilde{\boldsymbol{u}}}^{\mathrm{e}} = \begin{bmatrix} \tilde{u}_1^1 & \tilde{u}_2^1 & \tilde{u}_3^1 & \dots & \tilde{u}_1^{12} & \tilde{u}_2^{12} & \tilde{u}_3^{12} \end{bmatrix}^{\mathrm{T}}. \tag{8.74}$$

A definition of the gap function $\boldsymbol{g}$ was introduced in equation (8.10) in terms of shape functions, so the known gap $\boldsymbol{g}_{(n)}$ from the previous time-step can be conveniently discretized as

$$\boldsymbol{g}_{(n)} = \bar{\mathbf{H}}\, \hat{\tilde{\boldsymbol{u}}}^{\mathrm{e}}_{(n)}\,, \tag{8.75}$$

with the help of an altered interface $\mathbf{H}$-matrix as

$$\bar{\mathbf{H}} = \begin{bmatrix} \mathbf{N}_1 & 0 & 0 & \cdots & \mathbf{N}_6 & 0 & 0 & -\mathbf{N}_7 & 0 & 0 & \cdots & -\mathbf{N}_{12} & 0 & 0 \\ 0 & \mathbf{N}_1 & 0 & \cdots & 0 & \mathbf{N}_6 & 0 & 0 & -\mathbf{N}_7 & 0 & \cdots & 0 & -\mathbf{N}_{12} & 0 \\ 0 & 0 & \mathbf{N}_1 & \cdots & 0 & 0 & \mathbf{N}_6 & 0 & 0 & -\mathbf{N}_7 & \cdots & 0 & 0 & -\mathbf{N}_{12} \end{bmatrix}. \tag{8.76}$$

The first variation and the increment of the gap function then simply follow as

$$\delta\boldsymbol{g} = \bar{\mathbf{H}}\, \delta\boldsymbol{u}^{\mathrm{e}} \quad \text{and} \quad \Delta\boldsymbol{g} = \bar{\mathbf{H}}\, \Delta\hat{\tilde{\boldsymbol{u}}}^{\mathrm{e}}\,, \tag{8.77}$$

respectively. Inserting the above into (8.78) yields the discretized weak form contribution of the osseointegration interface as

$$\delta\Pi^{\mathrm{C}}_{(n+1)} = (\delta\boldsymbol{u}^{\mathrm{e}})^{\mathrm{T}} \varepsilon_{\mathrm{p}} \int_{\partial\mathcal{B}_0^{\mathrm{c}}} \bar{\mathbf{H}}^{\mathrm{T}} \mathfrak{C}_{(n+1)}\, \bar{\mathbf{H}}\, \mathrm{d}A\, \Delta\hat{\tilde{\boldsymbol{u}}}^{\mathrm{e}} + (\delta\boldsymbol{u}^{\mathrm{e}})^{\mathrm{T}} \varepsilon_{\mathrm{p}} \int_{\partial\mathcal{B}_0^{\mathrm{c}}} \bar{\mathbf{H}}^{\mathrm{T}} (\boldsymbol{g}_{(n)} - \boldsymbol{g}^{\mathrm{p}}_{(n)})\, \mathrm{d}A\,. \tag{8.78}$$

8.11 Embedding the interface contribution into the global Newton-Raphson scheme

In section 4.6, the global Newton-Raphson scheme was introduced. In this section, the linearized interface contributions shall be embedded into the global Newton-Raphson procedure. Therefore it is convenient to assume that for a Newton-Raphson iteration step (k), all increments of the gap function $\sum_{i=1}^{k-1} \Delta\boldsymbol{g}^{(i)}$, the osseointegration state $\rho_{(n)}$, the plastic gap $\boldsymbol{g}^{\mathrm{p}}_{(n)}$,

and the gap function $\boldsymbol{g}_{(n)}$, known from the last converged solution, are given. That enables the definition of the iterative trial gap as

$$\boldsymbol{g}_{(n+1)}^{\mathrm{tr},(k)} = \boldsymbol{g}_{(n)} - \boldsymbol{g}_{(n)}^{\mathrm{p}} + \sum_{i=1}^{k-1} \Delta \boldsymbol{g}^{(i)} \,. \tag{8.79}$$

In analogy to (4.44), an incremental version of the weak form contribution (8.78), linearized at $\bar{t} = t_{(n)} + \sum_{i=1}^{k-1} \Delta t^{(i)}$, can be stated as

$$\delta \Pi_{(n+1)}^{\mathrm{C}} = (\delta \boldsymbol{u}^{\mathrm{e}})^{\mathrm{T}} \varepsilon_{\mathrm{p}} \int_{\partial \mathcal{B}_0^{\mathrm{c}}} \bar{\mathbf{H}}^{\mathrm{T}} \mathfrak{C}_{(n+1)}^{(k)} \bar{\mathbf{H}} \, \mathrm{d}A \, \Delta \hat{\boldsymbol{u}}^{\mathrm{e}(k)} + (\delta \boldsymbol{u}^{\mathrm{e}})^{\mathrm{T}} \varepsilon_{\mathrm{p}} \int_{\partial \mathcal{B}_0^{\mathrm{c}}} \bar{\mathbf{H}}^{\mathrm{T}} \boldsymbol{g}_{(n+1)}^{\mathrm{e,tr},(k)} \, \mathrm{d}A \,. \tag{8.80}$$

8.11.1 Derivation of $\Delta\rho$ and $\Delta\boldsymbol{g}^{\mathrm{p}}$ within a global Newton-Raphson iteration

Recall that for computing the elastic trial gap

$$\boldsymbol{g}_{(n+1)}^{\mathrm{e,tr},(k)} = \hat{\boldsymbol{g}}^{\mathrm{e}}(\rho_{(n)} + \Delta\rho^{(k)}, \boldsymbol{g}_{(n+1)}^{\mathrm{tr},(k)}) \tag{8.81}$$

at time $\bar{t}$, the increment of the osseointegration state

$$\Delta\rho^{(k)} = \Delta t \hat{\mathfrak{R}}(\rho_{(n)}, \boldsymbol{g}_{(n+1)}^{\mathrm{e,tr},(k)}) \tag{8.82}$$

at time $\bar{t}$ must be known and vise versa. This assembles an *incremental-iterative* version of the constitutive initial boundary value problem for osseointegration contact interfaces $(8.50)_{2,3}$ as

$$\hat{\Phi} = \begin{pmatrix} \hat{\Phi}_{\rho} \\ \hat{\Phi}_{\boldsymbol{g}^{\mathrm{e}}} \end{pmatrix} = \begin{cases} \Delta\rho^{(k)} - \Delta t \hat{\mathfrak{R}}^{\mathrm{C}}(\rho_{(n)}, \boldsymbol{g}_{(n+1)}^{\mathrm{e,tr},(k)}) & = 0 \\ \boldsymbol{g}_{(n+1)}^{\mathrm{e,tr},(k)} - \hat{\boldsymbol{g}}^{\mathrm{e}}(\rho_{(n)} + \Delta\rho^{(k)}, \boldsymbol{g}_{(n+1)}^{\mathrm{tr},(k)}) & = \boldsymbol{0} \end{cases} . \tag{8.83}$$

This system of equations can be solved by an additional inner Newton-Raphson procedure as described in de Souza Neto et al. [2011] for the increment of the osseointegration state $\Delta\rho^{(k)}$ and the elastic trial gap $\boldsymbol{g}_{(n+1)}^{\mathrm{e,tr},(k)}$. Only after the global Newton-Raphson has converged for some time-step (m), it is allowed to update the osseointegration state

$$\rho_{(n+1)} = \rho_{(n)} + \Delta\rho^{(m)} \tag{8.84}$$

and the plastic gap

$$\boldsymbol{g}_{(n+1)}^{\mathrm{p}} = \boldsymbol{g}_{(n)}^{\mathrm{p}} + \Delta \boldsymbol{g}^{\mathrm{p}(m)} \,, \tag{8.85}$$

where the increment of the plastic gap can be defined as

$$\Delta \boldsymbol{g}^{\mathrm{p}(m)} = (g_{\mathrm{T}(n+1)}^{(m)} - g_{\mathrm{T}(n+1)}^{\mu(m)}) \cdot \boldsymbol{n}_{\mathrm{T}(n+1)}^{(m)} \tag{8.86}$$

since plastic deformations only take place in the tangential plane.

8.12 Numerical examples

All methods described in this chapter were implemented within a self-developed framework, written in the **julia** language [Bezanson et al., 2017]. In the following, two different numerical examples shall be conducted to prove the correctness of the methods described and their implementation. The first example performed on a reference geometry serves as a verification for the implemented methods. The second example is performed on a model of a bone with implanted prosthesis demonstrating the applicability of the methods developed for simulation of osseointegration after total hip replacement.

8.12.1 Model 1: fiber-reinforced composite

To verify the contact implementation, a patch-test, equipped with a contact surface as general as possible, shall be derived as a first example. Therefore, a quarter circle is inlaid into the lower

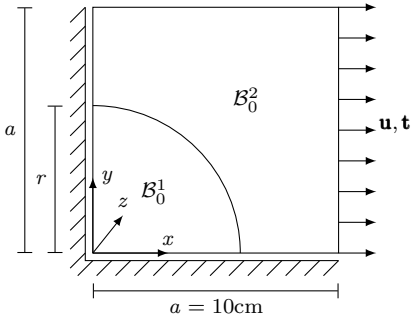

(a) patch-test model

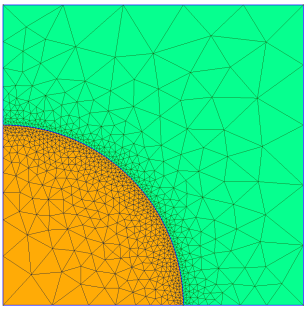

(b) generated mesh

Figure 8.9: Zero-thickness contact patch-test.

left edge of a three-dimensional cuboid-domain with dimensions $10 \times 10 \times 1$ mm^3. Symmetry boundary conditions are applied: the left edge is clamped in the x-direction $u_x(x = 0) = 0$, the lower edge is clamped in the y-direction $u_y(y = 0) = 0$, and the rear side is clamped in the z-direction $u_z(z = 1) = 0$. At the right-hand side ($x = 10$), constant displacement or constant traction is applied. The circular inlay and the exterior domain are named $\mathcal{B}_0^1$ and $\mathcal{B}_0^2$, respectively. A schematic representation of the patch-test model can be found in figure 8.9a. A mesh consisting of 18206 quadratic tetrahedral elements was generated according to the latter specifications and can be seen in figure 8.9b. In the contact interface, 4515 nodes were duplicated artificially, and 2152 zero-thickness elements were created.

No composite material, no plastic slip, and no osseointegration. As a first computational example, the same stiff material is chosen for both domains. More precisely, Young's modulus and Poisson's ratio can be stated as $E(\boldsymbol{X}) = 500\,\text{GPa}$ and $\nu(\boldsymbol{X}) = 0.3$, $\boldsymbol{X} \in \mathcal{B}_0^1 \cup \mathcal{B}_0^2$. Furthermore, a constant displacement of $2.5 \cdot 10^{-4}$ mm is applied at the right-hand side. In this example, no plastic slip will be considered ($\boldsymbol{g}^\text{p} \equiv \boldsymbol{0}$, $\boldsymbol{g}^\text{e} \equiv \boldsymbol{g}^*$), and no evolution of the osseointegration degree will occur ($\Delta\rho \equiv 0$). What can then be expected from that example is, due to the homogeneous boundary condition, a homogeneous stress field and a linear displacement field will be present, only disturbed by the gap in the contact interface, which depends on the introduced penalty parameter. In figure 8.10, the result of calculations performed as described above with penalty parameter $\varepsilon_\text{p} = 10^4$ MPa/mm and $\varepsilon_\text{p} = 10^6$ MPa/mm are displayed. Note that no color scale is indicated since we are only interested in identifying the displacement and stress field, respectively. In figure 8.10a, it is readily apparent that the usage of a penalty parameter of $\varepsilon_\text{p} = 10^4$ MPa/mm results in a disturbed displacement field, more precisely at $y = 0$, the gap in the interface amounts to $1.77 \cdot 10^{-4}$ mm, that is around 70 percent of the total applied displacement. In figure 8.10b, a penalty of $\varepsilon_\text{p} = 10^6$ MPa/mm was used, and in this example, a linear displacement field can be identified in the x-direction. The resulting gap at $y = 0$ in the interface amounts to $6.092 \cdot 10^{-6}$ mm, which corresponds to around 2 percent of the total applied displacement. In figure 8.10c, the stress $\boldsymbol{\sigma}_{22}$ is displayed for the penalty parameter $\varepsilon_\text{p} = 10^6$ MPa/mm. Due to the homogenous boundary condition, this component of

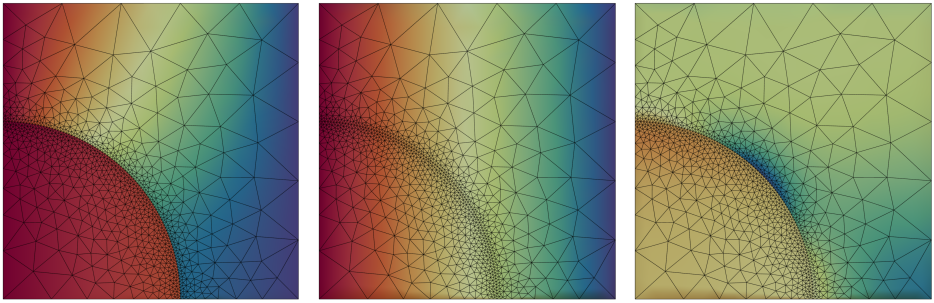

(a) displacement u_1, $\varepsilon_\mathrm{p} = 10^4$ (b) displacement u_3, $\varepsilon_\mathrm{p} = 10^6$ (c) stress $\boldsymbol{\sigma}_{22}$, $\varepsilon_\mathrm{p} = 10^6$

Figure 8.10: Exemplary results for two different penalty coefficients.

the stress tensor should be vanishing in the hole domain ($\boldsymbol{\sigma}_{22} \equiv 0$) in theory. Nevertheless, a maximum stress $\boldsymbol{\sigma}_{22}^{\max} = 9.914 \cdot 10^{-2}$ N/mm^2 can be identified, demonstrating the magnitude of the introduced error due to the contact interface for a very stiff material, which can serve as a worst-case scenario.

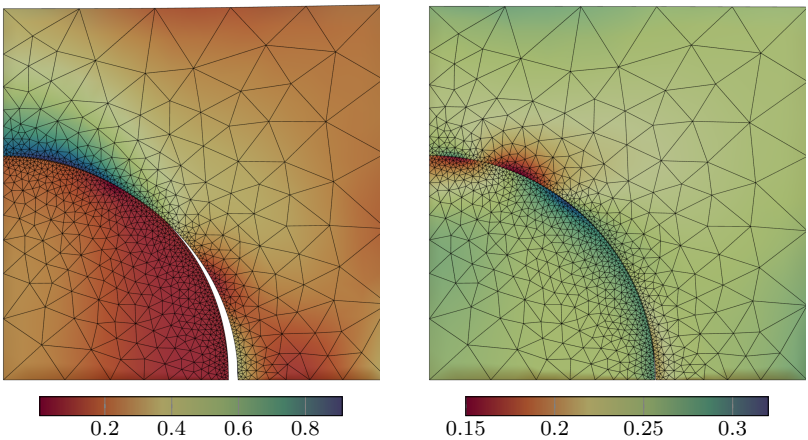

(a) $\rho = 0.01$ (b) $\rho = 1.0$

Figure 8.11: Von Mises stress [N/mm^2].

Composite material. As a second computational example, a composite material is now considered. Plastic slip is included while the osseointegration degree is fixed $\rho = 0.01$ for experiment one and at $\rho = 1.00$ for experiment two. Young's modulus of the fiber ($E(\boldsymbol{X}) = 200\,\mathrm{GPa}$, $\boldsymbol{X} \in \mathcal{B}_0^1$) is chosen to be four times higher than Young's modulus of the matrix ($E(\boldsymbol{X}) = 50\,\mathrm{GPa}$, $\boldsymbol{X} \in \mathcal{B}_0^2$), while both materials share the exact Poisson's ratio ($\nu(\boldsymbol{X}) = 0.3$,

$\boldsymbol{X} \in \mathcal{B}_0^1 \cup \mathcal{B}_0^2$). The constitutive adhesive function can be stated as

$$c(\rho) = 5 \cdot 10^{-6} + 2 \cdot 10^{-5} \cdot \rho \quad [\text{mm}]\,, \tag{8.87}$$

the constitutive frictional function as

$$\mu(\rho) = 0.1 + 1.25 \cdot \rho\,, \tag{8.88}$$

the penalty parameter is chosen as $\varepsilon_\text{p} = 10^4$ MPa/mm, and the regularization parameter as $r = 10^{-9}$ mm. In this example, Neumann boundary conditions are applied: a total force of 2.5 N is distributed equally to boundary faces of all elements at the right-hand side, following the concept of equivalent nodal forces. Figure 8.11 shows the von Mises stress for both osseointegration states, while the displacement is amplified by a factor of 2000 to make the interface behavior visible. In figure 8.11a, debonding of the interface can be observed, while in 8.11b, the gap is closed. Furthermore, in 8.11a, a peak in stress can be observed where the matrix rests on the fiber, while in 8.11a, this peak has vanished while remaining peaks in stress near the interface are caused by different transverse contractions. The tractions within

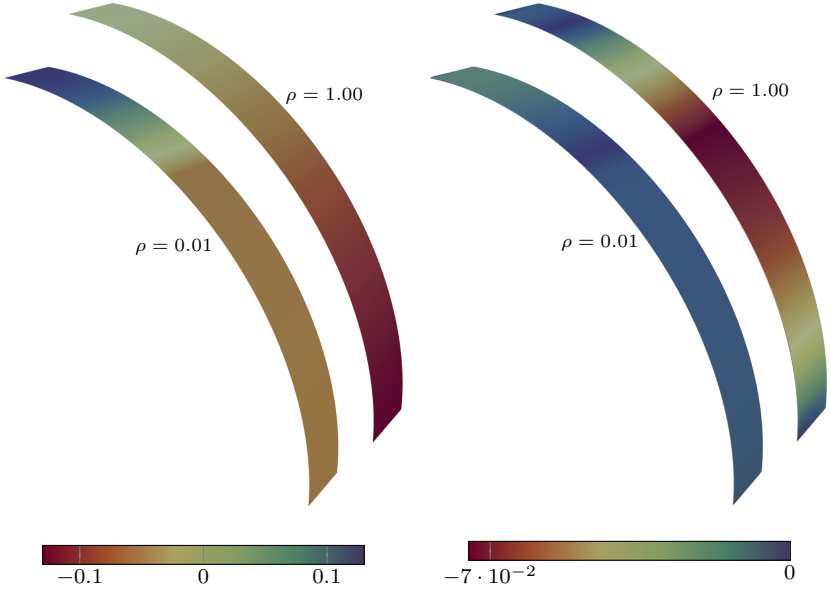

(a) $||\boldsymbol{C}_\text{N}||$ (b) $||\boldsymbol{C}_\text{T}||$

Figure 8.12: Interface tractions $||\boldsymbol{C}_\text{N}||$ and $||\boldsymbol{C}_\text{N}||$ [N].

the interface are shown in figures 8.12a and 8.12b for the normal interface traction and the tangential interface tractions, respectively. Note that the displacements are again amplified by a factor of 2000. Figure 8.12a illustrates the difference in normal interface tractions for the initial osseointegration state with $\rho = 0.01$ and the full osseointegrated state with $\rho = 1.0$. In the former osseointegration state, the interface transmits only a small amount of tension as described by the adhesive function $c(\rho = 0.01)$, while in the latter osseointegration state, the

interface can transmit tensions to the full extent. The tangential interface tractions, shown in figure 8.12b, are limited due to the constitutive version of Coulomb's law as stated in equation (8.24) for the initial osseointegration state and can be transferred to the full extent in the final osseointegration state. However, the amount of tangential tractions is small in this example and only results from different transversal contraction, as already mentioned.

8.12.2 Model 2: bone with implanted prosthesis

Finally, the contact interface shall be applied to the bone with an implanted prosthesis. The model was generated according to chapter 5, whereas the model was chosen to be discretized coarsely overall except for the surface of the prosthesis, where a finer discretization was chosen (cf. figure 8.13). All elements associated with the femoral head and all nodes solely associated with the femoral head have been erased. The same procedure has been applied to the top part of the prosthesis since it does not contribute to the simulation results in any way and is therefore not needed. Nodes within the bone-prosthesis interface have been doubled artificially

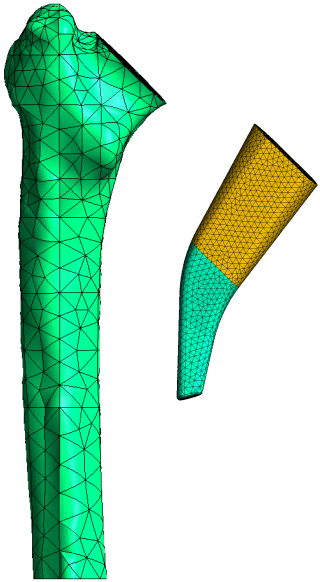

Figure 8.13: Resultant mesh.

to create the contact interface. This ultimately results in a mesh with 53334 and 240210 degrees of freedom. The set of boundary conditions defined in section 7.6.2, resulting in a physiological bone mineral density distribution within the bone, were adopted and transferred to the top part of the prosthesis accordingly. A detailed explanation of how this can be done for the femoral head is provided in section 11.1.3. This time the full osseointegration model, displaying plastic slip and change in the osseointegration state within the contact interface, is applied.
The set of parameters used in this computation is displayed in table 8.1. If the simulation has started, plastic slip is prevalent since the interface does not admit tension substantially. If the plastic slip is within the bounds of the defined admissible plastic slip, osseointegration

will occur proportional to the logarithmic osseointegration law, defined in equation (8.36). The simulation is said to be converged if the increment of plastic slip and, therefore, the increment of the osseointegration state within the contact interface is below a certain threshold. In figure

parameter	value	unit	parameter	value	unit
ε_{p}	500	$[\mathrm{MPa}/\mathrm{mm}]$	$g^{\mathrm{p}}_{\mathrm{min}}$	$-2.5 \cdot 10^{-6}$	[mm]
c_0	10^{-6}	[mm]	$g^{\mathrm{p}}_{\mathrm{opt}}$	$4.75 \cdot 10^{-4}$	[mm]
c_ρ	10^{-5}	[mm]	$g^{\mathrm{p}}_{\mathrm{max}}$	$1.75 \cdot 10^{-3}$	[mm]
μ_0	0.5	[−]	r	10^{-8}	[mm]
μ_ρ	20	[−]	$\psi^{\mathrm{Ce}}_{\mathrm{ref}}$	10^{-9}	$[\mathrm{MPa}/\mathrm{mm}]$
ρ_0	0.1	[−]	Δt	0.5	[s]
k	1	$[1/\mathrm{s}]$			

Table 8.1: Parameters for simulation of osseointegration.

8.14, the final osseointegration state is displayed. It can be seen that a partial ingrowth, as observed in clinical studies, can be displayed. The interface tractions in the initial as well as in the final state are shown in figure 8.15. A logarithmic color scale is applied since the different interface tractions between a non-osseointegrated and an osseointegrated area is in the range of several magnitudes. For the contact algorithm, including plastic slip, to converge sufficiently,

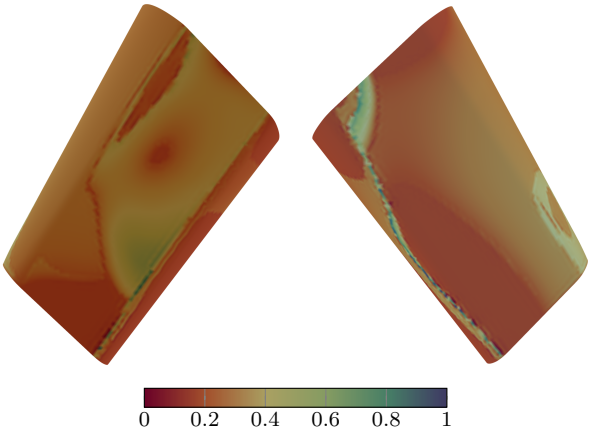

Figure 8.14: Final osseointegration state [−].

an active set iteration had to be introduced. This is necessary since otherwise integration points, which we know are currently not slipping, begin to slip nonetheless within the Newton-Raphson procedure because of the trial gap. An illustration of the convergence behavior of an entire simulation of an osseointegration procedure, including the active set iteration, can be found in image 8.16.

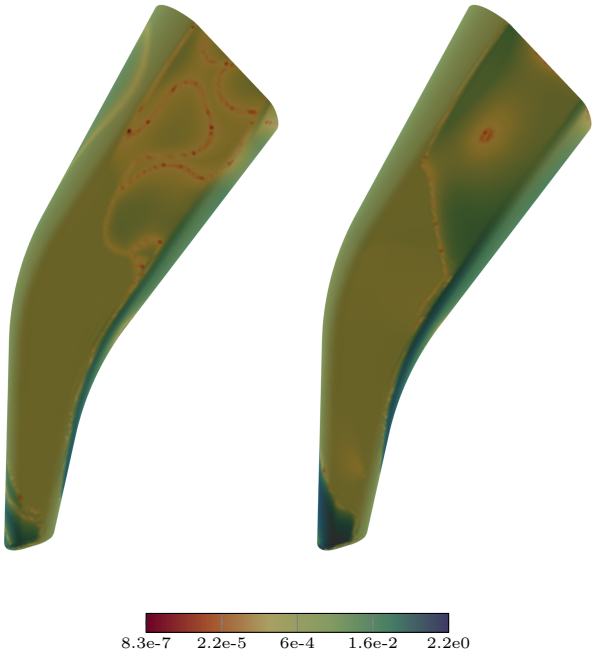

Figure 8.15: Interface tractions $||\boldsymbol{C}||$ [N/mm²] in the initial (left) and final (right) osseointegration state.

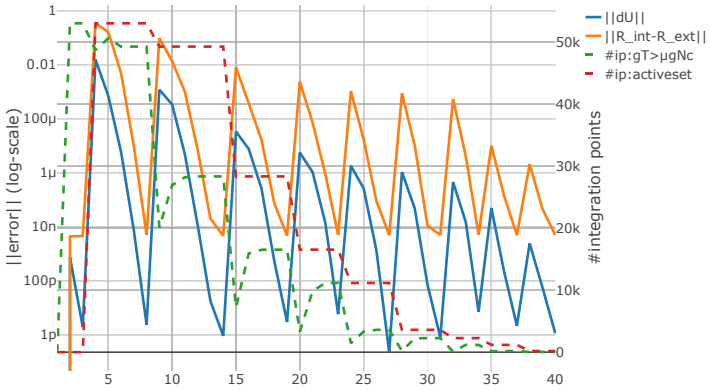

Figure 8.16: Convergence behavior of the osseointegration interface including active set iteration.

Chapter 9

Adaptive sparse grid collocation method

In this chapter, the adaptive sparse grid collocation method will be introduced. This is to be used in the following to build a surrogate model. We will start with an introductory example to illustrate the origin and idea of the method.
Let Ω be an open subset of $\mathbb{R}^n$ and $f : \Omega \to \mathbb{R}$ a real-valued function. Consider the example of a linear differential equation of form

$$\mathcal{L}y(x) = f(x) \quad x \in \Omega\,, \tag{9.1}$$

where $\mathcal{L} : C^k(\Omega) \to C^0(\Omega)$ is an abstract bounded *linear differential operator* of order k. For the approximative solution of equations of type (9.1), there exists a multitude of methods, most prominent the method of weighted residuals [see, e.g., Finlayson, 2013] and its derivatives, such as the Galerkin method. Hereby, the unknown solution is approximated by a function

$$y(x) \approx y'(x) = \sum_{i=1}^{n} c_i \phi_i(x)\,, \tag{9.2}$$

where $c_i \in \mathbb{R}$ are coefficients and the set $\{\phi_i\}_{i=1,\dots,n}$ assembles a basis for a finite-dimensional subspace of $C^0(\Omega)$. Accounting for the linearity of $\mathcal{L}$, substituting the latter into (9.1) enables the definition of a *residual*:

$$R(x) = \mathcal{L}y'(x) - f(x)\,, \tag{9.3}$$

with $|R(x)| > 0$. The method of weighted residuals then states that by choosing $(n-k)$ appropriate weight functions $w_i : \Omega \to \mathbb{R}$ together with k boundary conditions, it is possible to force the residual to vanish in the sense of integrals:

$$\int_\Omega R(x) w_i(x)\,\mathrm{d}\Omega = 0 \quad \forall w_i\,, i = 1, \dots, n-k\,. \tag{9.4}$$

The latter yields a system of equations and can be solved for the unknown coefficients c_i. Variations of the method of weighted residuals differ primarily in the choice of weight functions. Following Kajotoni [2008], it is possible to derive the collocation method from selecting the *Dirac delta distribution* for the weights w_i as

$$w_i(x) = \delta(x - x_i) \quad \text{with} \quad \delta(x - x_i) = \begin{cases} 1 & \text{if } x = x_i\,, \\ 0 & \text{otherwise.} \end{cases} \tag{9.5}$$

Substituting the latter into (9.4) yields

$$R(x_i) = \int_{\Omega} R(x)\delta(x - x_i)\,\mathrm{d}\Omega = 0\,, \tag{9.6}$$

demonstrating that the residual is in fact zero at the *collocation points* x_i. An interpolatory basis, such as a Lagrange basis, is used to obtain intermediate values between collocation points. It can be shown that as more points are included, the solution converges to the analytic solution. The collocation method was first proposed in Frazer et al. [1937], while first investigations in an error-efficient distribution of collocation points in space were carried out by Kadner [1960]. Wright [1964] and Villadsen and Stewart [1967] were among the first to use the roots of orthogonal Chebyshev polynomials as collocation points to achieve better convergence. Because of its easy and efficient application to the numerical solution of integral equations, the collocation method had been widely used in the following years [see, e.g., Schapery, 1962, Newman, 1971, Russell and Shampine, 1972, Douglas and Dupont, 1973, Hsiao et al., 1980, Yang and Peet, 1988]. Sparse tensor product quadrature rules, mitigating the *curse of dimensions* occurring in full tensor grid constructions, were provided early by Smolyak [1963]. Still, it has taken some time before Zenger and Hackbusch [1990] introduced that concept into collocation methods, while sparse grids with underlying Chebyshev nodes were first studied in Poplau [1995] and Sprengel [1997]. In the last two decades, collocation methods were prominent in the solution of *stochastic partial differential equations*, as shown in Babuška et al. [2007] and Nobile et al. [2008]. Ma and Zabaras [2009] were able to once again increase the efficiency of the collocation approach by introducing an error-adaptive formulation of the method, which will serve as a basis for the collocation method described in this thesis. Finally, it can be noted that Gates and Bittens [2015] provided an extension of the latter by the introduction of a hierarchy of successively finer spatial discretizations, an idea adopted from the multilevel Monte Carlo method [see, e.g., Heinrich, 2001].
Below, one-dimensional sparse grid construction and a corresponding one-dimensional Lagrangian basis are derived first. Hereafter, it will be shown how this concept easily translates to higher dimensions.

9.1 Hierarchical grid construction in one dimension

Consider the construction of a one-dimensional collocation grid $\mathcal{G}$ on an interval $[-1, 1]$. Then, the total amount n of collocation points up to level l can be determined by the nested Clenshaw-Curtis rule:

$$n(l) = \begin{cases} 1 & \text{if } l = 1\,, \\ 2^{l-1} + 1 & \text{if } l > 1\,. \end{cases} \tag{9.7}$$

The tuple $(m, l) \in \mathbb{N}_+ \times \mathbb{N}_+$ can serve as an abstract identifier for a collocation point, where $m \leq n(l)$ is an ordinal number, and l is the level of the collocation point's first occurrence. Due to the nested structure, it is possible to re-identify each collocation point (m, l) on level $l + 1$ by

$$m^{\uparrow}(m, l) = \begin{cases} 2 & \text{if } l = 1\,, \\ 2m - 1 & \text{if } l > 1\,. \end{cases} \tag{9.8}$$

It is emphasized that collocation points (m, l) only *exist* on level l, while all possible level transitions by the $m^{\uparrow}$ operator only refer to a *placeholder* needed to construct the basis, as

shown in the next section. Furthermore, it is possible to state the position $\hat{\xi}$ of each collocation point (m, l) with the help of the rule

$$\hat{\xi}_l^m = \hat{\xi}(m,l) = \begin{cases} 0 & \text{if } n(l) = 1\,, \\ -1 + \frac{2(m-1)}{n(l)-1} & \text{if otherwise}\,. \end{cases} \tag{9.9}$$

By (9.7),(9.8), and (9.9), it is possible to identify a *parent-child relationship* between a collocation point (m, l) and its at most two child collocation points

$$\mathcal{C}(m,l) = \begin{cases} \{\mathcal{C}_l\} = \left\{(m^{\uparrow}+1, l+1)\right\} & \text{if } m = 1\,, \\ \{\mathcal{C}_r\} = \left\{(m^{\uparrow}-1, l+1)\right\} & \text{if } m = n(l)\,, \\ \{\mathcal{C}_l, \mathcal{C}_r\} = \left\{(m^{\uparrow}-1, l+1), (m^{\uparrow}+1, l+1)\right\} & \text{if otherwise}\,. \end{cases} \tag{9.10}$$

To make this construct viable, the definition of a *root point* $(m, l) = (1, 1)$ is sufficient. An

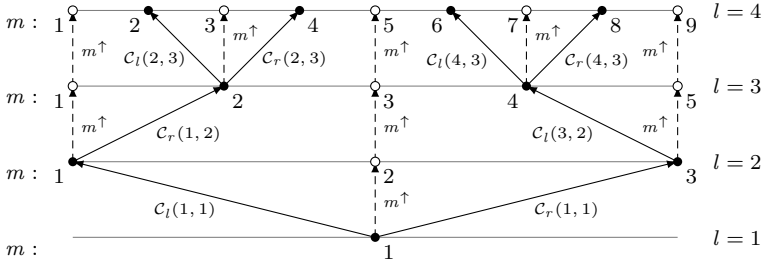

Figure 9.1: Grid construction in one dimension.

illustration of this approach to collocation grids in one dimension can be found in figure 9.1.

9.2 Lagrangian bases for one-dimensional collocation grids

There are several choices for Lagrangian bases for sparse grids, including the global Lagrangian basis (see figure 9.2a) and the local Lagrangian basis (see figure 9.2b). A one-dimensional stochastic sparse grid with k collocation points, equipped with the well-known global Lagrangian basis

$$\mathcal{I}^{\mathrm{g}}(x) = \sum_{i=1}^{k} c_i l_i(x)\,, \quad c_i \in \mathbb{R}\,, \quad l_i(x) = \prod_{\substack{1 \le m \le k \\ m \neq i}} \frac{x - x_m}{x_i - x_m}\,, \tag{9.11}$$

was shown to retain the exponential convergence rate of the *probability error* in the stochastic state-space that was first established for the spectral stochastic Galerkin approach [Babuška et al., 2007]. But, this result holds only if relatively strict assumptions for the smoothness of the input data are made, i.e., the occurrence of steep gradients in the stochastic state-space can lead to *Runge's phenomenon*. Therefore, for non-smooth problems, the local Lagrangian basis with compact support seems favorable, despite its slower convergence. To obtain superior efficiency, Ma and Zabaras [2009] introduced a hierarchical local Lagrangian basis into sparse

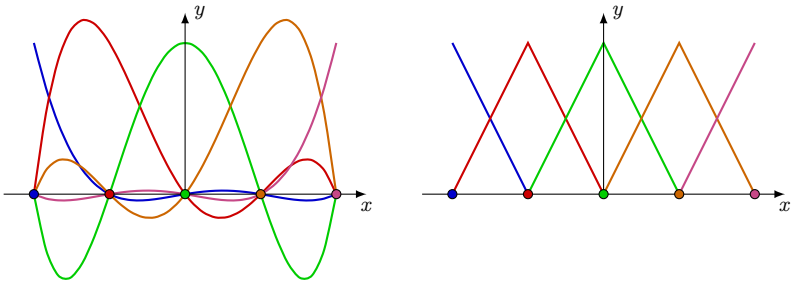

(a) Global Lagrangian basis. (b) Local linear Lagrangian basis.

Figure 9.2: Interpolatory bases in one dimension.

grid collocation, enabling for *local refinement* of collocation points instead of the common *level-wise refinement* approach. To construct the latter basis, the *local support* of a collocation point in one dimension shall be defined first as

$$\operatorname{supp}(m,l) = \begin{cases} [-1,1] & \text{if } l = 1\,, \\ [-1,\hat{\xi}_l^{m+1}] & \text{if } l > 1 \wedge m = 1\,, \\ [\hat{\xi}_l^{m-1},1] & \text{if } l > 1 \wedge m = n(l)\,, \\ [\hat{\xi}_l^{m-1},\hat{\xi}_l^{m+1}] & \text{else.} \end{cases} \tag{9.12}$$

The hierarchical basis

$$\mathcal{I}^k(x) = \sum_{\substack{(m,l)\in\mathcal{G} \\ l\leq k}} c(m,l)\,a(m,l,x) = \sum_{\substack{(m,l)\in\mathcal{G} \\ l\leq k}} c_l^m\,a_l^m(x)\,, \quad x, c_l^m \in \mathbb{R}\,, \tag{9.13}$$

or, in other words, the *hierarchical interpolator* up to level k, is constructed starting with the definition of a *constant* basis function $a_1^1 = 1$, for the root point. Assuming the sparse grid shall

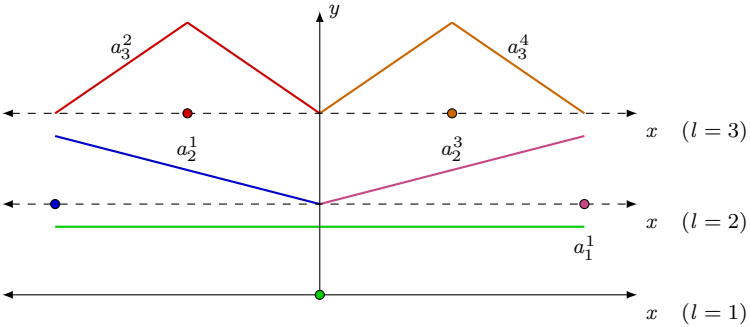

Figure 9.3: Hierarchical local Lagrangian basis in one dimension.

interpolate a function f, the coefficient $c_1^1 = f(\hat{\xi}_1^1)$ follows from a simple function evaluation. For points on a hierarchical level $l > 1$, the basis function can be stated as

$$a_l^m(x) = \begin{cases} \frac{x - \hat{\xi}_l^{m-1}}{\hat{\xi}_l^m - \hat{\xi}_l^{m-1}} & \text{if } x \leq \hat{\xi}_l^m \ \wedge \ x \in \text{supp}(m,l)\,, \\ \frac{x - \hat{\xi}_l^{m+1}}{\hat{\xi}_l^m - \hat{\xi}_l^{m+1}} & \text{if } x > \hat{\xi}_l^m \ \wedge \ x \in \text{supp}(m,l)\,, \\ 0 & \text{else.} \end{cases} \tag{9.14}$$

Consequently, coefficients c_l^m, $l > 1$ can be found with the help of the hierarchical interpolator of the underlying level $l-1$, i.e., $c_l^m = f(\hat{\xi}_l^m) - \mathcal{I}^{l-1}(\hat{\xi}_l^m)$. Such a hierarchical basis for three hierarchical levels can be seen in figure 9.3. Its application in interpolating an exemplary function

$$f(x) = \frac{1}{1 + e^{-5*x}} - \frac{2}{5}\,, \tag{9.15}$$

along with the three *level interpolators* $\mathcal{I}^1$, $\mathcal{I}^2$, and $\mathcal{I}^3$, is displayed in figure 9.4.

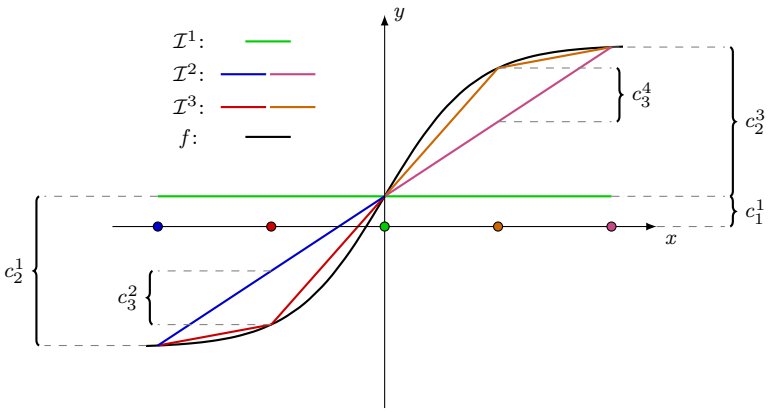

Figure 9.4: Hierarchical interpolation in one dimension.

9.3 Adaptive local refinement

The coefficients c_l^m can be interpreted as a *hierarchical surplus* providing a local improvement prediction for the next level interpolator $\mathcal{I}^{l+1}$. Consequently, a refinement strategy can be defined: Consider a sparse grid $\mathcal{G}$ with l levels and level interpolator $\mathcal{I}^l$. Then collocation points (m,l) spawn their hierarchical children $\mathcal{C}(m,l)$, as described in equation 9.10, only if their hierarchical surplus is larger than some predefined threshold $c_l^m > \epsilon^{\text{ref}}$.

It has to be stated that this procedure fails if a function value $f(\hat{\xi}_l^m)$ coincidentally meets the interpolant $\mathcal{I}^{l-1}(\hat{\xi}_l^m) - f(\hat{\xi}_l^m) = 0$ but exhibits a difference $\mathcal{I}^{l-1}(\hat{\xi}_l^m + \varepsilon) - f(\hat{\xi}_l^m + \varepsilon) > \epsilon^{\text{ref}}$ elsewhere in its near surrounding. However, for physical problems, the risk can be considered negligible if the initial level l_{init} of the sparse grid is sufficiently high.

9.4 Sparse grid construction

From a one-dimensional grid $\mathcal{G}$ on $[-1,1]$, the full grid in e.g. two dimensions $\mathcal{G}\otimes\mathcal{G}$ on $[-1,1]\otimes[-1,1]$ can be constructed via crosswise tensor products of all one-dimensional entities, resulting in a dense grid as shown in figure 9.5(a) for three hierarchical levels. For a d-dimensional sparse

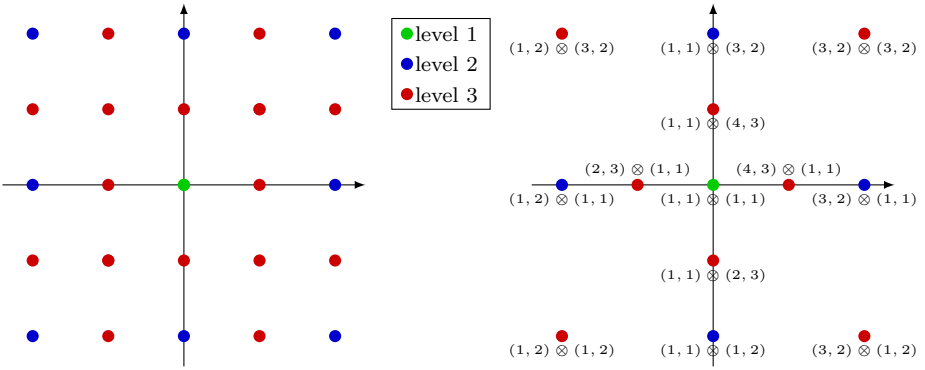

(a) full grid (b) sparse grid

Figure 9.5: Full grid and sparse grid in two dimensions.

grid, we can rather think of the construction as the tensor product extension of the abstract identifier (m,l) to d-dimension and the subsequent execution of one-dimensional rules onto each factor therein. We will make this idea concise in the following, starting by introducing the d-dimensional abstract identifier for collocation points as

$$(\boldsymbol{m},\boldsymbol{l}) = (m_1,l_1)\otimes\cdots\otimes(m_d,l_d)\,,\quad \boldsymbol{m},\boldsymbol{l}\in\mathbb{N}_+^d\,, \tag{9.16}$$

which for the root-point results in $(1,1)\otimes\cdots\otimes(1,1)$. A d-dimensional collocation point then spawns at most $2d$ hierarchical children by the subsequent application of (9.10) onto each factor as

$$\begin{aligned}\mathcal{C}(\boldsymbol{m},\boldsymbol{l}) =&\{\mathcal{C}(m_1,l_1)\otimes(m_2,l_2)\otimes\cdots\otimes(m_d,l_d)\cup\cdots\\ &\cdots\cup(m_1,l_1)\otimes\cdots\otimes(m_{d-1},l_{d-1})\otimes\mathcal{C}(m_d,l_d)\}\,.\end{aligned} \tag{9.17}$$

Note that collocation points that spawn multiple times within a hierarchical refinement step can be eliminated by set-builder notation, e.g., all unique collocation points arising from a complete level transition from level k to $k+1$ can be gathered by

$$\bigcup_{\substack{(\boldsymbol{m},\boldsymbol{l})\in\mathcal{G}\\ 1-d+|\boldsymbol{l}|=k}}\mathcal{C}(\boldsymbol{m},\boldsymbol{l})\,. \tag{9.18}$$

The result thereof for three hierarchical levels is displayed in figure 9.5(b), illustrating the sparse characteristic compared to the full tensor grid. The construction of the support then follows as

$$\operatorname{supp}(\boldsymbol{m},\boldsymbol{l}) = \operatorname{supp}(m_1,l_1)\otimes\cdots\otimes\operatorname{supp}(m_d,l_d)\,, \tag{9.19}$$

and the construction of the basis functions follows by simple multiplication

$$a_{\boldsymbol{l}}^{\boldsymbol{m}}(\boldsymbol{x}) = \prod_{i=1}^{d} a_{l_i}^{m_i}(x_i)\,, \tag{9.20}$$

resulting in the level interpolator

$$\mathcal{I}^k(\boldsymbol{x}) = \sum_{\substack{(\boldsymbol{m},\boldsymbol{l})\in\mathcal{G}\\ 1-d+|\boldsymbol{l}|\le k}} c_{\boldsymbol{l}}^{\boldsymbol{m}}\, a_{\boldsymbol{l}}^{\boldsymbol{m}}(\boldsymbol{x})\,, \quad \boldsymbol{x}\in\mathbb{R}^d\,, \quad c_{\boldsymbol{l}}^{\boldsymbol{m}}\in\mathbb{R}\,. \tag{9.21}$$

9.5 Numerical example

The methods described above lend themselves readily to efficient and straightforward implementation, carried out in the julia language [Bezanson et al., 2017]. Proof shall be provided by the example of a non-smooth two-dimensional function

$$f(\boldsymbol{x}) = \frac{1}{|\sqrt{2} - (x_1-1)^2 - (x_2-1)^2 + \frac{1}{2}|}, \quad f\in \mathrm{C}^0\,, \quad \boldsymbol{x}\in\mathbb{R}^2 \tag{9.22}$$

on $[1,1]^2$, where the non-smoothness is a curved kink. The grid is generated by setting the tolerance to $\epsilon^{\mathrm{ref}} = 10^{-4}$ and the maximum number of grid levels is set to 25. In figure 9.6,

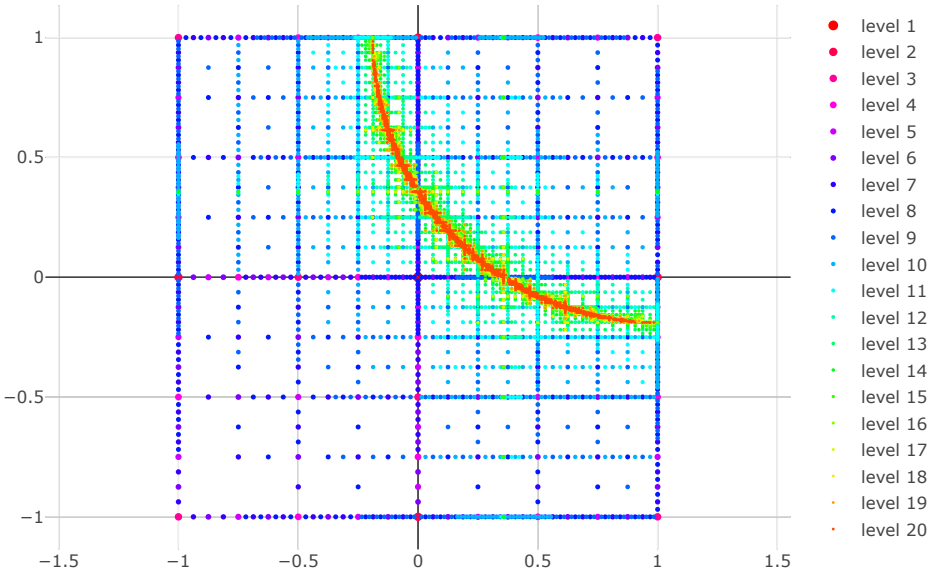

Figure 9.6: Refinement pattern for sample non-smooth function in two dimensions.

the first 20 levels of the grid, consisting of a total of 9392 collocation points, are displayed, illustrating the adaptive refinement. The sampled function is displayed in figure 9.7a, and

the relative error in comparison to Monte Carlo sampling is displayed in figure 9.7b. For the Monte Carlo convergence plot, the function (9.22) was integrated with three different sample sizes: (1) 10,000, (2) 100,000 and (3) 1,000,000 sample points. For each sample size, the numerical integration was carried out 1000 times. The result is visualized as a *box plot*. For more information on box plots, the reader is referred to Williamson et al. [1989]. Note that as dimensions in state-space are added, the convergence of Monte Carlo sampling will catch up to the convergence rate of the collocation grid.

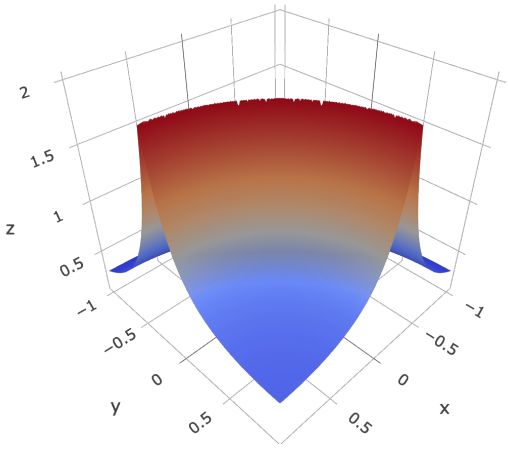

(a) Sampled response surface on $[-1, 1] \otimes [-1, 1]$.

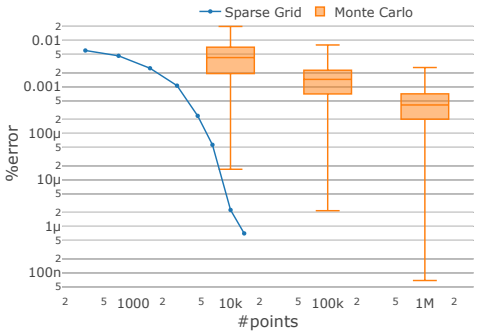

(b) Relative error compared to Monte Carlo sampling.

Figure 9.7: Non-smooth examplary two-dimensional function.

Chapter 10

A comprehensive approach in prediction of biomechanical compatibility in total hip arthroplasty

In the previous chapters, all necessary methods were laid out to describe the evolution of bone mineral density following total hip replacement. The result of the osseointegration process, described in chapter 8, is an indicator for secondary stability, while consecutive simulation of bone remodeling, as described in chapter 7, can serve as an indicator for long-term stability.
As a first step, different abstract computational models $\mathcal{M}^{(\cdot)}$ will be described, defined by their sets of inputs and outputs, considering the models themselves as black boxes. By that, the need for *surrogate modeling* will be demonstrated. A surrogate is a simplified model of the *outcome*, which can be used whenever the behavior of a system should be investigated but cannot be measured directly because of the computational complexity of the original system. Nowadays, a large number of methods are subsumed under the term surrogate modeling. Following Asher et al. [2015], surrogate models can be divided into three basic categories: (1) Data-driven models, which are built upon empirical evaluation of a complex model, (2) projection-based models, where the governing equations are projected onto a reduced dimensional subspace and (3) multi-fidelity based models, where the underlying physics is simplified, or the numerical resolution is reduced. Examples of data-driven models are *kringing* [Dubourg et al., 2011, Han and Görtz, 2012] or the *response surface methodology* [Jones, 2001, Khuri and Mukhopadhyay, 2010]. Prominent projection-based methods are, among others, *proper orthogonal decomposition* [Willcox and Peraire, 2002, Rowley, 2005] or the *Karhunen-Loève expansion* [see, e.g., Kim, 1998]. Multifidelity-based models are especially interesting if multiple information sources with different fidelities are available [Lam et al., 2015]. For more information about surrogate modeling, the reader is referred to Queipo et al. [2005], Razavi et al. [2012], or Roy and Datta [2018], for example.

10.1 Black box modeling

In the following, different computation models $\mathcal{M}^{(\cdot)}$ shall be defined by their differences in inputs and outputs. The model itself is left as a black box in this section, assuming that each model applies the same basic operations to their inputs to generate their correspondent version of the output. That is, the models, in fact, solely differ in inputs and outputs. To create common ground, inputs shared by all models are a CAD model $\mathcal{D}$ of the human femur and a CAD model $\mathcal{P}$ of the prosthesis equipped with an initial position within the human femur. Different outputs y for each model are conceivable and also feasible: $y = \varrho(\boldsymbol{X})$ could be a scalar field of bone mineral density, $y = \int_{\mathcal{B}} \varrho(\boldsymbol{X}) \,\mathrm{d}V$ (alternatively $y = \int_{\partial\mathcal{B}^c} \rho(\boldsymbol{X}) \,\mathrm{d}A$) could be some scalar-valued reference number, or $\boldsymbol{y} = \{\hat{y}_i\}_{i=1,\dots,n_{\text{nodes}}}$ could be a vector-valued output assembled from nodal data of a post-processed finite element result. It is also possible to define $\boldsymbol{y} = \{y_i\}_{i=1,\dots,n_{\text{outputs}}}$ a ordered set of different outputs. For notational convenience, only

a common abstract output y shall be defined here for all models, which is left to be further specified using concrete applications at a later stage.

10.1.1 The deterministic model $\mathcal{M}^{\mathrm{D}}$

A deterministic model $\mathcal{M}^{\mathrm{D}}$ is a classical model, which yields a deterministic output for a given set of deterministic inputs:

$$y = \mathcal{M}^{\mathrm{D}}(\mathcal{D}, \mathcal{P}, \boldsymbol{\theta}^{\mathrm{M}}, \boldsymbol{\theta}^{\mathrm{P}}) \,, \tag{10.1}$$

where $\boldsymbol{\theta}^{\mathrm{M}} \in \boldsymbol{\mathcal{I}}^{\mathrm{M}}$ is the set of parameters describing a specific physical admissible prosthesis position (see chapter 5), while in $\boldsymbol{\theta}^{\mathrm{P}}$ different patient-specific parameters could be assembled as well as all parameters needed for each single simulation step.

10.1.2 The full model $\mathcal{M}^{\mathrm{F}}$

As a preliminary remark, the designation as *the full model* is not rigorous and was only made to indicate where a reduced model shall be derived from in the next stage. The full model $\mathcal{M}^{\mathrm{F}}$ is no longer deterministic as it includes all physical admissible prostheses positions $\boldsymbol{\mathcal{I}}^{\mathrm{M}}$ as an input parameter. In $\boldsymbol{\mathcal{I}}^{\mathrm{M}}$, all intervals $\mathcal{I}_i$, defined in chapter 5, are assembled. As a result, the output

$$y(\boldsymbol{\mathcal{I}}^{\mathrm{M}}) = \mathcal{M}^{\mathrm{F}}(\mathcal{D}, \mathcal{P}, \boldsymbol{\mathcal{I}}^{\mathrm{M}}, \boldsymbol{\theta}^{\mathrm{P}}) \tag{10.2}$$

depends on $\boldsymbol{\mathcal{I}}^{\mathrm{M}}$ as well, a concept which would be called the *forward propagation of uncertainty* in a probabilistic framework. In fact, the approach taken here could be a probabilistic framework if a suitable probability space (Ω, F, P) was defined, where Ω is a sample space, F is a σ-*algebra*, and P is a probability measure. It can be pointed out that $\boldsymbol{\mathcal{I}}^{\mathrm{M}}$ is not a well-defined sample space for arbitrary rotations since the prosthesis position as described in chapter 5 is defined by Euler-angles. There are several approaches available [among others Downs, 1972, Mardia, 1975, Habeck, 2009] describing the statistics of the orientation of bodies embedded in $\mathbb{R}^3$, which could potentially be applied here to achieve a well-defined sample space. Consequently, assigning an appropriate *probability density function*, which for example, renders larger deviation from the initial position as less likely, would result in a probabilistic framework. The result of such a probabilistic calculation could be an *expected* bone mineral density distribution that takes implantation inaccuracies made by the surgeon into account. While this is a promising approach, it is stated to be beyond the scope of this thesis and could be seen as a natural extension thereof.

By analogy with the probabilistic framework, it can be easily demonstrated that the full model is not computable in full complexity: consider $y = y_t$ to be a *random process* with finite variance, then it can be shown that a spectral representation [cf. Chien and Fu, 1967, Le Gratiet et al., 2017] exists as the infinite series

$$y_t = \sum_{i=1}^{\infty} \sqrt{\lambda_i} \xi_i \phi_i(t) \,, \tag{10.3}$$

where ξ_i are pairwise uncorrelated random variables, ϕ_i are real-valued eigenfunctions on $\mathcal{B}$, which are pairwise orthogonal in $L^2(\mathcal{B})$, and λ_i are their correspondent eigenvalues.

Finally, it can be stated that by including parametric representations for $\mathcal{D}$ and $\mathcal{P}$, as described in Dopico-González et al. [2009], Mehrez and Browne [2012], or Ro et al. [2018], and by defining admissible ranges for patient-individual characteristics in $\boldsymbol{\theta}^{\mathrm{P}}$, it would also be possible to define a fully parametric approach, which could make *model-specific* predictions on biomechanical compatibility for a larger set of individuals.

10.1.3 The surrogate model $\mathcal{M}^{\mathrm{SG}}$

In the last section, it was demonstrated that the full model could not be computed. As a result, *model order reduction* has to be introduced at this point. In this thesis, the use of the response surface methodology is preferable because of its inherent interpolation property. More precisely, the *adaptive hierarchical sparse grid collocation method* proposed in Ma and Zabaras [2009] will be used. However, all response surface methods are based on a so-called *experimental design*

$$\mathcal{X} = \{\boldsymbol{\theta}^{\mathrm{M},(\boldsymbol{\alpha}_1)=(1,\dots,1)}, \dots, \boldsymbol{\theta}^{\mathrm{M},(\boldsymbol{\alpha}_m)=(n,\dots,n)}\}\,, \tag{10.4}$$

which is based on a limited number of *realizations*

$$\mathcal{X}_i = \boldsymbol{\theta}^{\mathrm{M},(\boldsymbol{\alpha}_i)} = [\theta_1^{\alpha_{i1}}, \theta_2^{\alpha_{i2}}, \theta_3^{\alpha_{i3}}, \theta_4^{\alpha_{i4}}, \theta_5^{\alpha_{i5}}, \theta_6^{\alpha_{i6}}, \theta_7^{\alpha_{i7}}] \tag{10.5}$$

from all physically admissible prosthesis positions $\boldsymbol{\mathcal{I}}^{\mathrm{M}}$. By notational abuse, the superscript $(\boldsymbol{\alpha}_i)$ in $\boldsymbol{\theta}^{\mathrm{M},(\boldsymbol{\alpha}_i)}$, $i = 1, \dots, 7$ is a *multi-index* and is not referring to a time-step. The latter enables the definition of an approximate model of the outcome as

$$y \approx y' = \mathcal{M}^{\mathrm{SG}}(\mathcal{D}, \mathcal{P}, \mathcal{X}, \boldsymbol{\theta}^{\mathrm{P}})\,. \tag{10.6}$$

Recalling the assumption as mentioned above that all models proposed here perform the same basic operations and only differ in their inputs and outputs, for each realization $\mathcal{X}_i$ of the experimental design, a deterministic simulation run

$$y_i = \mathcal{M}^{\mathrm{D}}(\mathcal{D}, \mathcal{P}, \mathcal{X}_i, \boldsymbol{\theta}^{\mathrm{P}}) \tag{10.7}$$

is performed with the help of which the model of the outcome is generated. Hence, it is possible to re-write (10.6) as

$$y' = \mathcal{M}^{\mathrm{SG}}(y_1, \dots, y_m)\,. \tag{10.8}$$

It can be shown that this is equivalent to truncating the infinite series in equation (10.9) after p terms, resulting in

$$y_t = \sum_{i=1}^{p} \sqrt{\lambda_i}\xi_i\phi_i(t)\,, \tag{10.9}$$

which renders the problem computationally feasible. Note that the coefficients in the latter equations are determined explicitly in a Karhunen-Loeve expansion. By choosing these p terms with the largest eigenvalues λ_i, optimality of the reduced basis is guaranteed for problems with fast decaying eigenvalues. In response surface methods, this property is not preserved, rendering the selection of realizations from the experimental design highly relevant.

10.2 White box modeling

In delimitation from the previous section's black box modeling approach, in this section, the computational models are defined by their internal program flow. This will serve to define and illustrate the simulation process for the deterministic computational model $\mathcal{M}^{\mathrm{D}}$ and the reduced computational model $\mathcal{M}^{\mathrm{SG}}$. The full model $\mathcal{M}^{\mathrm{F}}$ is discontinued since it was only an abstract concept to derive the reduced model. In the last section, it was demonstrated that the deterministic model serves as an input to the reduced model in the form of simulation results of realizations $\mathcal{X}_i$ of the experimental design $\mathcal{X}$. It is therefore sensible to define the deterministic model $\mathcal{M}^{\mathrm{D}}$ as a modeling approach in predicting secondary and long-term stability in total hip arthroplasty, including different patient individual characteristics for a *specific* prosthesis position and the reduced model $\mathcal{M}^{\mathrm{SG}}$ as the subsequent non-intrusive extension thereof to *all* physically admissible prosthesis position, which fulfills the objective of this thesis.

10.2.1 The deterministic model $\mathcal{M}^{\mathrm{D}}$

The deterministic model, previously defined by its inputs $(\mathcal{D}, \mathcal{P}, \boldsymbol{\theta}^{\mathrm{M}}, \boldsymbol{\theta}^{\mathrm{P}})$, shall now be further specified by its internal program sequence. Despite differences in the chosen methods for single simulation steps, the overall modeling approach of Lutz [2011] was adopted here. An illustration thereof can be found in figure 10.1, where each simulation step and its input parameter are indicated.
The first simulation step is the automatic model and mesh generation, introduced in chapter 5, in which the full model of the femur with the head (1) and the model of the femur with an implanted prosthesis (2) are generated and meshed. In the next step (3), a biomechanical equilibrated bone mineral density distribution for the femur with the head is generated. Therefore, bone remodeling following the principle of static-equivalent forces and related biomechanical equilibrated bone mineral density distribution, as described in chapter 7, is applied. The forces used herein, adopted from Lutz and Nackenhorst [2007], were shown to produce realistic bone mineral density distributions in section 7.6.2. As a next step, the bone mineral density distri-

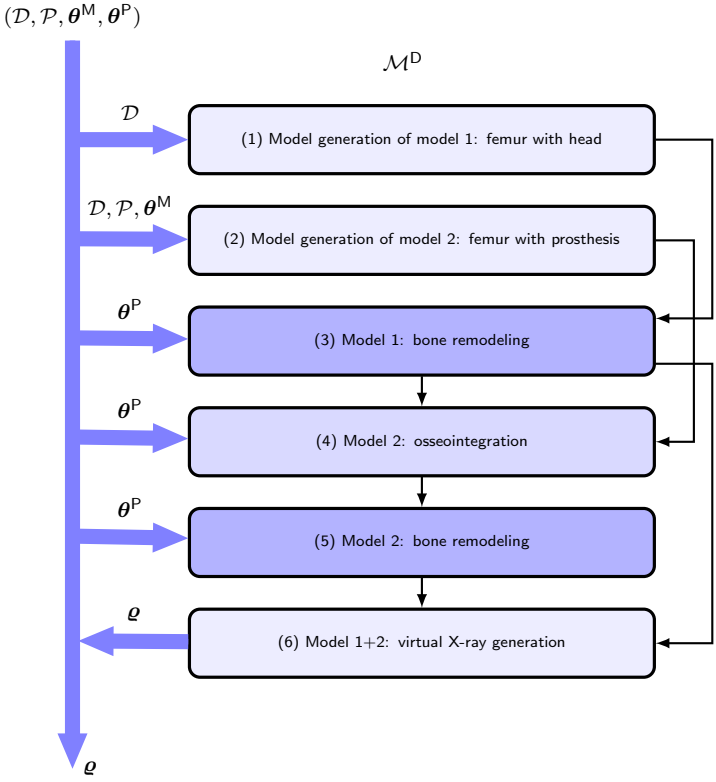

Figure 10.1: Program sequence for a simulation call of the deterministic model $\mathcal{M}^{\mathrm{D}}$.

bution from (3) is transferred to the model with an implanted prosthesis, which is trivial since

both models share the same mesh topology in their overlapping parts due to the meshing procedure. Consequently, simulation of osseointegration (4) is performed, as described in chapter 8. During the simulation of osseointegration, the internal bone mineral density distribution is assumed to remain unchanged. After that, bone remodeling (5) is applied once again, this time to the prosthesis with an implanted femur and converged osseointegration result, which results in a biomechanical equilibrated bone mineral density distribution for the altered conditions. In this simulation step, the osseointegration result is assumed to remain unchanged. Finally, virtual X-ray imaging (6), as described in chapter 6, is applied to both the model resultant from steps (3) and (5).

10.2.2 The surrogate model $\mathcal{M}^{\mathrm{SG}}$

Finally, the program sequence for the surrogate model $\mathcal{M}^{\mathrm{SG}}(\mathcal{D}, \mathcal{P}, \mathcal{X}, \boldsymbol{\theta}^{\mathrm{P}})$ is determined and

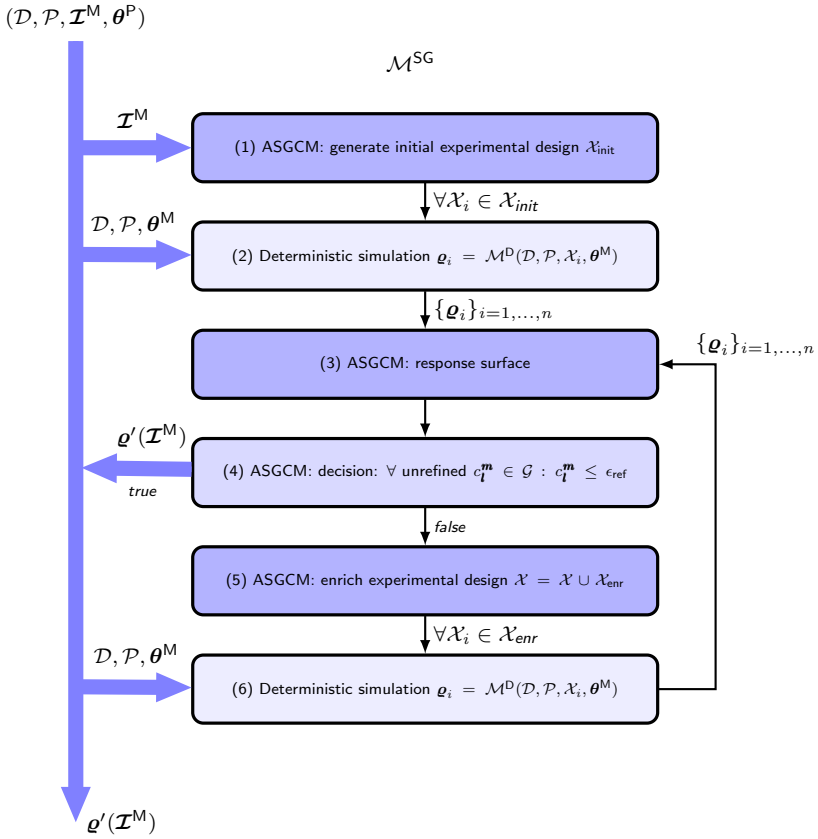

Figure 10.2: Program sequence for a simulation call of the surrogate model $\mathcal{M}^{\mathrm{SG}}$.

displayed in figure 10.2. As mentioned earlier, the surrogate, i.e., the response surface, is

built by the adaptive sparse grid collocation method (ASGCM), defined in chapter 9. First, an initial experimental design $\mathcal{X}_{\text{init}}$ has to be created (1) for the hierarchical surpluses $c_{\boldsymbol{l}}^{\boldsymbol{m}}$ to provide a reliable improvement prediction. In general, $d+1$ hierarchical levels will be sufficient for a d-dimensional parametric model. For every $\mathcal{X}_i \in \mathcal{X}_{\text{init}}$, a deterministic simulation $\boldsymbol{\varrho}_i = \mathcal{M}^{\text{D}}(\mathcal{D}, \mathcal{P}, \mathcal{X}_i, \boldsymbol{\theta}^{\text{M}})$ is carried out (2). In the first place, the response surface (3) is generated with the help of the initial experimental design $\mathcal{X}_{\text{intit}}$ alone.
Consequently, the experimental design is enriched: by evaluating the hierarchical surpluses for each unrefined collocation point, the collocation points that spawn their hierarchical children can be determined. Again, deterministic simulations are carried out whenever a new collocation point is spawned (6). With each new collocation point, the resolution in state-space increases. Eventually, the response surface is stated to be converged if the hierarchical surplus $c_{\boldsymbol{l}}^{\boldsymbol{m}}$ is smaller than some predefined threshold ϵ_{ref} for all unrefined collocation points.

Chapter 11

Numerical examples

In this chapter, all of the previously introduced methods shall be used in order to create a comprehensive example of bone remodeling due to total hip replacement with a parametric prosthesis position.

11.1 Configuration of the model

In chapter 10, different computation models were defined, first by means of abstract in- and outputs. Afterward, the deterministic model $\mathcal{M}^{\mathrm{D}}$ and the reduced model $\mathcal{M}^{\mathrm{SG}}$ were further defined by their respective simulation procedures. What is left to define are the precise in- and outputs for the deterministic and surrogate model, that is, the patient-specific and simulation-specific parameters $\boldsymbol{\theta}^{\mathrm{P}}$ and the range of physically admissible prothesis positions $\mathcal{I}^{\mathrm{M}}$, respectively. While the former is defined in the following, the latter will be defined in the next section together with their concrete applications.

11.1.1 Patient-specific and simulation-specific parameters $\boldsymbol{\theta}^{\mathbf{P}}$

As already mentioned, in $\boldsymbol{\theta}^{\mathrm{P}}$, all parameters are assembled that does not change during the parametric computation. In the following, $\boldsymbol{\theta}^{\mathrm{P}}$ shall be defined by the different simulation steps, which are X-ray simulation, automatic model generation, numerical bone remodeling, and the numerical simulation of osseointegration.

X-ray simulation. For the X-ray simulation, the algorithm described in chapter 6 is adopted as is, except for the resolution, which is decreased to 1600 rays per cm^2 and 60 samples per cm in the depth-direction as this seems to result in a sufficient resolution while reducing computational time.

Automatic model generation. In geometric modeling, the only parameter which does not vary for both numeric examples is the length of the coating area $\theta_7 = 4.5$ cm. Still, this parameter could readily be used for further studies concerning the influence of the length of the coating area on the long-term stability of hip prostheses. In the meshing procedure, the mesh density is reduced to approximately 50.000 degrees of freedom for each model.

Numerical bone remodeling. The parameters in section 7.1 defining the E-ϱ-relation are adopted. The reference strain energy and the additional exponent are set to $\Psi^{\mathrm{ref}} = 2.25 \cdot 10^{-4}$ $\mathrm{N/mm}^2$ and $m = 4$, respectively, while all other parameters are adopted from the numerical example 7.6.2.

Numerical simulation of osseointegration For the simulation of osseointegration, all parameters introduced in section 8.12.2 are adopted. An overview of all parameters is given in table 8.1.

11.1.2 Quantity of interest

Another crucial parameter is the *quantity of interest* $y = f(\boldsymbol{x})$, which is defined by the output of the deterministic model. Often it is assumed that f changes smoothly with changes in $\boldsymbol{x}$, a prerequisite for using sparse grids with global Lagrangian bases. For the highly complex and multi-staged simulation carried out in this thesis, a smooth response surface in parametric state-space cannot be guaranteed in general. Nevertheless, a smooth response in state-space is highly advantageous for efficient integration, and for many non-smooth problems, it is still possible to define a smooth quantity of interest. For example, pressure and velocity fields in compressible flow models may be non-smooth functions, but derived quantities, such as an integrated measure of the pressure, may be smooth [Constantine, 2015].
The outcome of the deterministic simulation defined in section 10.2.1 was two X-ray images: the first one from the bone in pre-operative state and the second one of the bone with an implanted prosthesis in the long-term equilibrated state. Therefore, it is possible to generate an image displaying the change in the percentage of bone mineral density due to the implanted prosthesis. This image itself is not an objective measure since the prosthesis position differs for different input vectors. For example, if the prosthesis is shifted in the longitudinal direction, the resection height is altered, which leads to a change of total bone mass of the remaining bone. To mitigate the effects of the change in prosthesis position on the smoothness of the

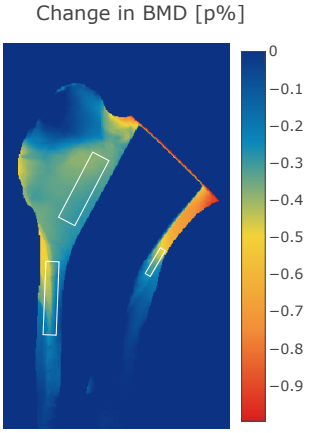

Figure 11.1: Example plot of percentage change in bone mineral density due to THA.

response surface, three boxes are defined in which the change in bone mineral density should be measured instead. Since the image is just a matrix filled with values between 0 and 1, it is easy to select the subset of values inside the three boxes, defined in figure 11.1, and subsequently derive the L^2-norm of the matrix defined by each box and sum up the results.

11.1.3 Boundary conditions

One more crucial point is the application of boundary conditions. While for parts of the mesh that remain unchanged, boundary conditions defined in section 7.6.2 can be adopted, boundary conditions applied to the femoral head have to be transferred to the upper surface of the prosthesis (see figure 11.2) with care. It shall be recalled at this point that the prosthesis position and, therefore, its upper surface position is altered by the set of parameters $\boldsymbol{\theta}^{\mathrm{M}}$. Thus, it

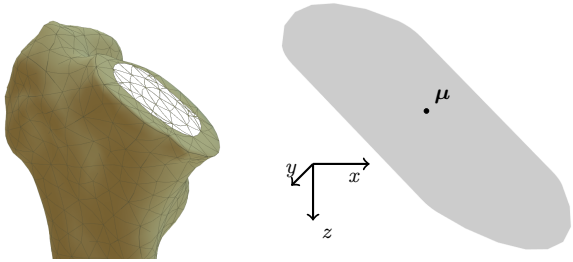

Figure 11.2: Bone with implanted prosthesis (left picture) and prosthesis surface with center $\boldsymbol{\mu}$ for application of Neumann boundary conditions (right picture).

seems sensible to make the following assumption to transfer the Neumann boundary conditions applied to the femoral head to the upper prosthesis surface, equivalently: despite the implanted prosthesis, the transmission of forces remains *physiological*, i.e., the internal forces are not being altered.

The forces applied to the femoral head, as shown in figure 7.5, are readily available in terms of equivalent nodal force coefficients $\boldsymbol{f}^{\mathrm{FH,ext}}$ (c.f. section 4.5). We can disassemble the latter vector into three vectors $\boldsymbol{f}_x^{\mathrm{FH}}$,$\boldsymbol{f}_y^{\mathrm{FH}}$, and $\boldsymbol{f}_z^{\mathrm{FH}}$, with equivalent nodal force coefficients pointing in the x, y, and z-direction, respectively. Note that these vectors are constructed to be aligned with the ordered set $\hat{\boldsymbol{x}}^{\mathrm{FH}}$. In $\hat{\boldsymbol{x}}^{\mathrm{FH}}$, all nodal position vectors of the two-dimensional elements $\mathcal{E}^{\mathrm{FH}}$ on the surface of the femoral head are uniquely assembled. By notational abuse, we denote a scalar-valued entry of $\boldsymbol{f}_x^{\mathrm{FH}}$ by f_{ix}^{FH} and a vector-valued entry of $\hat{\boldsymbol{x}}^{\mathrm{FH}}$ by $\hat{\boldsymbol{x}}^{i,\mathrm{FH}}$.

At this point, another simplification is introduced: the moments generated by the original boundary condition and the moments generated by the new boundary conditions, applied on the upper prosthesis surface shall coincide at the center of the prosthesis surface $\boldsymbol{\mu}$. The center itself is calculated as shown in (6.4).

To get a *1-load* in each coordinate direction, the vector $\boldsymbol{t}_{\mathrm{F}} = [1,1,1]^{\mathrm{T}}$ is integrated numerically, according to equations (4.44) - (4.41), against all shape functions of the two-dimensional elements $\mathcal{E}^{\mathrm{PS}}$ on the upper surface of the prosthesis. The result is disassembled, equivalently to $\boldsymbol{f}^{\mathrm{FH,ext}}$, resulting in the three vectors $\boldsymbol{f}_{1,x}^{\mathrm{PS}}$,$\boldsymbol{f}_{1,y}^{\mathrm{PS}}$, and $\boldsymbol{f}_{1,z}^{\mathrm{PS}}$, which are aligned with the nodal positions $\hat{\boldsymbol{x}}^{\mathrm{PS}} \in \mathcal{E}^{\mathrm{PS}}$. For moment generating equivalent nodal force coefficients, the latter procedure is repeated with the vectors $\boldsymbol{t}_{\mathrm{M}_x} = [0,0,x-\mu_1]^{\mathrm{T}}$, $\boldsymbol{t}_{\mathrm{M}_y} = [0,0,y-\mu_2]^{\mathrm{T}}$, and $\boldsymbol{t}_{\mathrm{M}_z} = [y-\mu_2,0,0]^{\mathrm{T}}$, resulting in the vectors $\boldsymbol{f}_{z,\mathrm{M}_x}^{\mathrm{PS}}$ $\boldsymbol{f}_{z,\mathrm{M}_y}^{\mathrm{PS}}$, and $\boldsymbol{f}_{x,\mathrm{M}_z}^{\mathrm{PS}}$, respectively. Note that the sum of the vectors

$$F_{z,\mathrm{M}_x} = \sum f_{z,\mathrm{M}_x}^{\mathrm{PS}} \neq 0\,, \tag{11.1}$$

$$F_{z,\mathrm{M}_x} = \sum f_{z,\mathrm{M}_y}^{\mathrm{PS}} \neq 0\,, \text{ and} \tag{11.2}$$

$$F_{x,\mathrm{M}_z} = \sum f_{x,\mathrm{M}_z}^{\mathrm{PS}} \neq 0 \tag{11.3}$$

is small but not exactly zero. We further define the total applied forces to the femural head as

$$F_x = \sum_i f_{ix}^{\mathrm{FH}}\,, \tag{11.4}$$

$$F_y = \sum_i f_{iy}^{\mathrm{FH}}\,, \text{ and} \tag{11.5}$$

$$F_z = \sum_i f_{iz}^{\mathrm{FH}}\,, \tag{11.6}$$

the total applied moment to the femural head with respect to $\boldsymbol{\mu}$ as

$$[M_x, M_y, M_z]^{\mathrm{T}} = \sum_i \left[[f_{ix}^{\mathrm{FH}}, f_{iy}^{\mathrm{FH}}, f_{iz}^{\mathrm{FH}}]^{\mathrm{T}} \times (\hat{\boldsymbol{x}}^{i,\mathrm{FH}} - \boldsymbol{\mu}) \right]\,, \tag{11.7}$$

the resultant 1-load forces applied to the prosthesis as

$$1_x = \sum_i f_{ix}^{\mathrm{PS}}\,, \tag{11.8}$$

$$1_y = \sum_i f_{iy}^{\mathrm{PS}}\,, \text{ and} \tag{11.9}$$

$$1_z = \sum_i f_{iz}^{\mathrm{PS}}\,, \tag{11.10}$$

the intentionally generated moments applied to the prosthesis as

$$[M_{x,\mathrm{M}_x}^{\mathrm{PS}}, M_{y,\mathrm{M}_x}^{\mathrm{PS}}, 0]^{\mathrm{T}} = \sum_i \left[[0, 0, f_{iz,\mathrm{M}_x}^{\mathrm{PS}}]^{\mathrm{T}} \times (\hat{\boldsymbol{x}}^{i,\mathrm{FH}} - \boldsymbol{\mu}) \right]\,, \tag{11.11}$$

$$[M_{x,\mathrm{M}_y}^{\mathrm{PS}}, M_{y,\mathrm{M}_y}^{\mathrm{PS}}, 0]^{\mathrm{T}} = \sum_i \left[[0, 0, f_{iz,\mathrm{M}_y}^{\mathrm{PS}}]^{\mathrm{T}} \times (\hat{\boldsymbol{x}}^{i,\mathrm{FH}} - \boldsymbol{\mu}) \right]\,, \text{ and} \tag{11.12}$$

$$[0, M_{y,\mathrm{M}_z}^{\mathrm{PS}}, M_{z,\mathrm{M}_z}^{\mathrm{PS}}]^{\mathrm{T}} = \sum_i \left[[f_{ix,\mathrm{M}_z}^{\mathrm{PS}}, 0, 0]^{\mathrm{T}} \times (\hat{\boldsymbol{x}}^{i,\mathrm{FH}} - \boldsymbol{\mu}) \right]\,, \tag{11.13}$$

and, finally, the unintentionally generated moments applied to the prosthesis as

$$[0, M_{y,1_x}^{\mathrm{PS}}, M_{z,1_x}^{\mathrm{PS}}]^{\mathrm{T}} = \sum_i \left[[f_{ix}^{\mathrm{PS}}, 0, 0]^{\mathrm{T}} \times (\hat{\boldsymbol{x}}^{i,\mathrm{FH}} - \boldsymbol{\mu}) \right]\,, \tag{11.14}$$

$$[M_{x,1_y}^{\mathrm{PS}}, 0, M_{z,1_y}^{\mathrm{PS}}]^{\mathrm{T}} = \sum_i \left[[0, f_{iy}^{\mathrm{PS}}, 0]^{\mathrm{T}} \times (\hat{\boldsymbol{x}}^{i,\mathrm{FH}} - \boldsymbol{\mu}) \right]\,, \quad \text{and} \tag{11.15}$$

$$[M_{x,1_z}^{\mathrm{PS}}, M_{y,1_z}^{\mathrm{PS}}, 0]^{\mathrm{T}} = \sum_i \left[[0, 0, f_{iz}^{\mathrm{PS}}]^{\mathrm{T}} \times (\hat{\boldsymbol{x}}^{i,\mathrm{FH}} - \boldsymbol{\mu}) \right]\,. \tag{11.16}$$

The latter assembles a linear system of equations

$$\mathbf{A}\boldsymbol{x} = \boldsymbol{b}\,, \tag{11.17}$$

with

$$\mathbf{A} = \begin{bmatrix} 1_x & 0 & 0 & 0 & 0 & F_{x,\mathrm{M}_z} \\ 0 & 1_y & 0 & 0 & 0 & 0 \\ 0 & 0 & 1_z & F_{z,\mathrm{M}_x} & F_{z,\mathrm{M}_y} & 0 \\ 0 & M_{x,1_y}^{\mathrm{PS}} & M_{x,1_z}^{\mathrm{PS}} & M_{x,\mathrm{M}_x}^{\mathrm{PS}} & M_{x,\mathrm{M}_y}^{\mathrm{PS}} & 0 \\ M_{y,1_x}^{\mathrm{PS}} & 0 & M_{y,1_z}^{\mathrm{PS}} & M_{y,\mathrm{M}_x}^{\mathrm{PS}} & M_{y,\mathrm{M}_y}^{\mathrm{PS}} & M_{y,\mathrm{M}_z}^{\mathrm{PS}} \\ M_{z,1_x}^{\mathrm{PS}} & M_{z,1_y}^{\mathrm{PS}} & 0 & 0 & 0 & M_{z,\mathrm{M}_z}^{\mathrm{PS}} \end{bmatrix} \quad \text{and} \quad \boldsymbol{b} = \begin{bmatrix} F_x \\ F_y \\ F_z \\ M_x \\ M_y \\ M_z \end{bmatrix}\,, \tag{11.18}$$

which owns full rank and can be solved for the coefficients $\boldsymbol{x}$. Finally, the vectors are scaled with their corresponding coefficients as $\boldsymbol{f}'^{\mathrm{PS}}_{1,x} = x_1 \boldsymbol{f}^{\mathrm{PS}}_{1,x}$, $\boldsymbol{f}'^{\mathrm{PS}}_{1,y} = x_2 \boldsymbol{f}^{\mathrm{PS}}_{1,y}$, $\boldsymbol{f}'^{\mathrm{PS}}_{1,z} = x_3 \boldsymbol{f}^{\mathrm{PS}}_{1,z}$, $\boldsymbol{f}'^{\mathrm{PS}}_{z,\mathrm{M}_x} = x_4 \boldsymbol{f}^{\mathrm{PS}}_{z,\mathrm{M}_x}$, $\boldsymbol{f}'^{\mathrm{PS}}_{z,\mathrm{M}_y} = x_5 \boldsymbol{f}^{\mathrm{PS}}_{z,\mathrm{M}_y}$, and $\boldsymbol{f}'^{\mathrm{PS}}_{x,\mathrm{M}_z} = x_6 \boldsymbol{f}^{\mathrm{PS}}_{x,\mathrm{M}_z}$ and assembled into the global system of equations (4.39).

11.2 Two-dimensional parametric study

In this first numerical study, only two of all six possible parameters affecting prosthesis placement shall be varied, that is, the longitudinal shift θ_1 and the transversal shift θ_2. Therefore, the vector defining the prothesis position can be stated as

$$\boldsymbol{\theta}^{\mathrm{M}} = [\theta_1, \theta_2, 0, 0, 0, 0]\,, \quad \theta_1, \theta_2 \in [-1\,\mathrm{mm}, 1\,\mathrm{mm}]\,, \tag{11.19}$$

and a sparse grid with two dimensions in parametric state-space is created. Consequently, 29 collocation points on four consecutive levels of the sparse grid are generated. This can be done

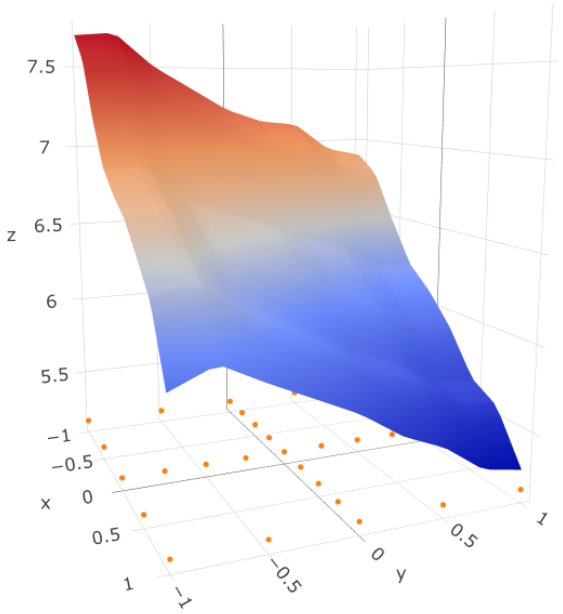

Figure 11.3: Response surface with the longitudinal shift plotted on the x-axis, the transversal shift on the y-axis, and the L^2-norm of the percentage loss in bone mineral density in the three defined regions on the z-axis.

fully in parallel. Every single calculation takes approximately less than two hours on a recent workstation (Intel i7@3.6GHz, 32GB RAM), so presuming 29 distinct workers are available,

$\boldsymbol{\theta}^{\mathrm{M}} = [0.9, 0, 9]$ $\boldsymbol{\theta}^{\mathrm{M}} = [-0.9, -0, 9]$

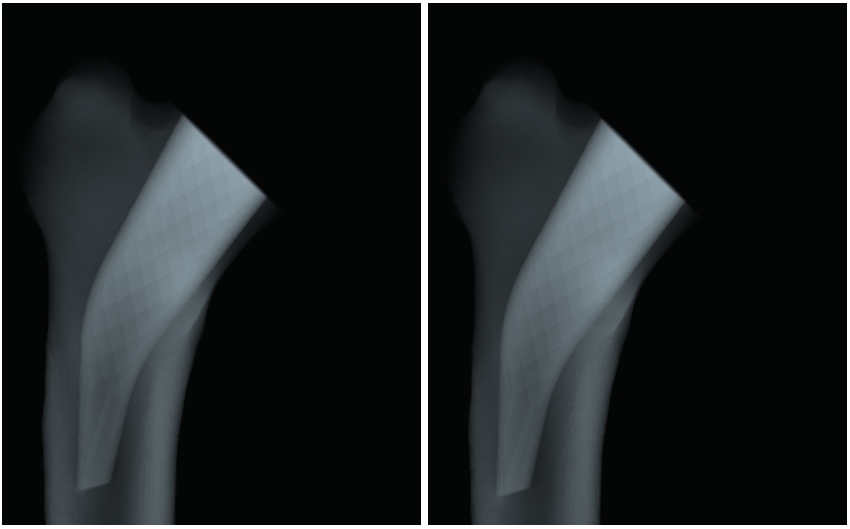

(a) (b)

Virtual X-ray images of long-term equilibrated bone mineral density.

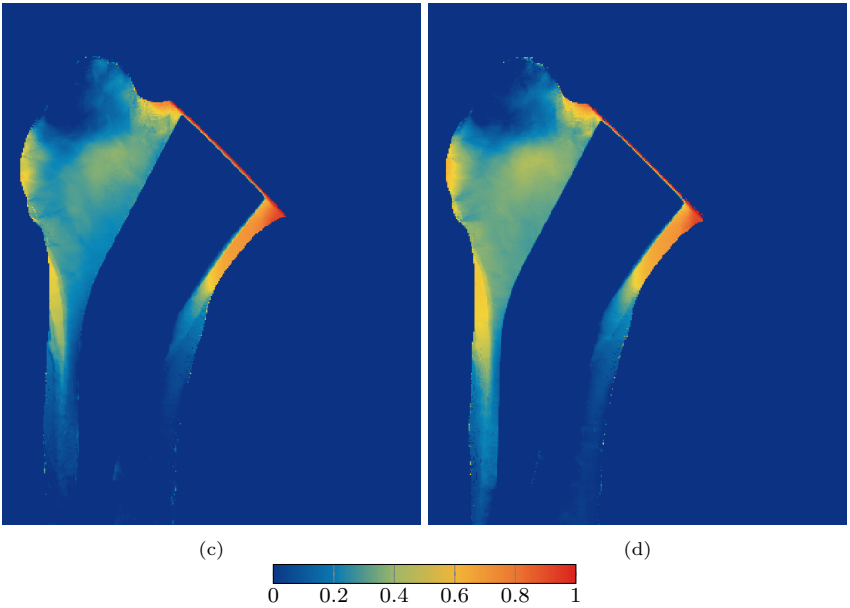

(c) (d)

Percentage change [p%] in bone mineral density.

Figure 11.4: Exemplary results of two-dimensional parametric study.

the complete simulation takes about two hours in total. More points could be added to the parametric state-space, but as can be seen in figure 11.4, the informative value and sharpness of virtual X-ray images interpolated by the sparse grid at intermediate locations seem sufficient. It is noted that since it is physical in nature, the problem should exhibit a smooth variation in state-space. But there is evidence of a certain low-magnitude non-smoothness in the response surface, as seen in figure 11.3. This non-smoothness can be interpreted as a measure for the modeling error made in the simulation process, primarily the non-exact application of boundary conditions and the not fully objective quantity of interest. The same applies to the operations performed in the geometry and mesh creation, which are not exact to the accuracy of the calculation. As a result, adding more collocation points has to be done with great care since the error is additive across levels, and therefore its magnitude is likely to increase. Consequently, adaptive refinement is not applied in the shown numerical examples. But more important here is that the magnitude of this error is much smaller than the solution itself, which is the case since a clear trend is visible: both a positive longitudinal and transversal shift, which coincides with a greater resection height, seem beneficial for a smaller loss in bone mineral density. Still, for both exemplarily shown prosthesis positions, there is a great loss of around 70-85% of bone mineral density in the neck region of the femur.

11.3 Six-dimensional parametric study

To provide an example in full complexity, all possible parameters affecting prosthesis placement shall be varied:

$$\boldsymbol{\theta}^{\mathrm{M}} = [\theta_1, \theta_2, \theta_3, \theta_4, \theta_5, \theta_6]\,, \tag{11.20}$$

$$\theta_1, \theta_2, \theta_3 \in [-0.25\,\mathrm{mm}, 0.25\,\mathrm{mm}]\,, \text{ and} \tag{11.21}$$

$$\theta_4, \theta_5, \theta_6 \in [-1^\circ, 1^\circ]\,. \tag{11.22}$$

Unfortunately, for a reliable meshing procedure, the interval range of the parameters had to be further reduced. However, this does not affect the numerical complexity of the problem and could be remedied by using better initial models. In the last example, the four corner collocation points of the rectangle, i.e., $[1, 1]$, $[-1, 1]$, $[1, -1]$ and $[-1, -1]$, were sampled on the third level, where the grid contains 13 collocation point in total (see figure 9.5b). In six dimensions, the 64 extremal points of the hypercube, i.e $[1, 1, 1, 1, 1, 1], \ldots, [-1, -1, -1, -1, -1, -1]$, spawn on level seven of the six-dimensional grid. Consequently, 15121 collocation points across seven hierarchical levels of the sparse-grid were generated using the cluster system at the Leibniz University of Hanover. Here, 768 workers can be allocated per user, where around 600 workers were available on average. Therefore, the simulation took around 50 hours to be carried out. Exemplary results of two illustrative prosthesis positions $\boldsymbol{\theta}_1^{\mathrm{M}} = [0.995, 0.999, -0.997, 0.996, 0.978, 0.993]$ and $\boldsymbol{\theta}_2^{\mathrm{M}} = [-0.995, -0.999, 0.997, -0.996, -0.978, -0.993]$ are shown in figure 11.5. The interpolation quality is inferior compared with the two-dimensional example. For more information on convergence and interpolation quality of sparse grids in higher dimensions, the reader is referred to Pflüger [2010]. For comparable interpolation results, at least one or two additional refinement steps would have to be made, resulting in a sparse grid with up to 127105 collocation points. Since that would result in an estimated simulation time on the cluster of about three weeks, it was decided not to further refine. As a first conclusion, it can be stated that a six-dimensional sparse grid for such a complex simulation can be created but not yet for a cost-efficient application with user-specific predictions, at least with the methods presented in this work. A way to overcome this obstacle could be achieved with *dimension adaptive sparse grids* (see, e.g., Jakeman and Roberts [2011]), which could be included in this approach as a next model refinement step.

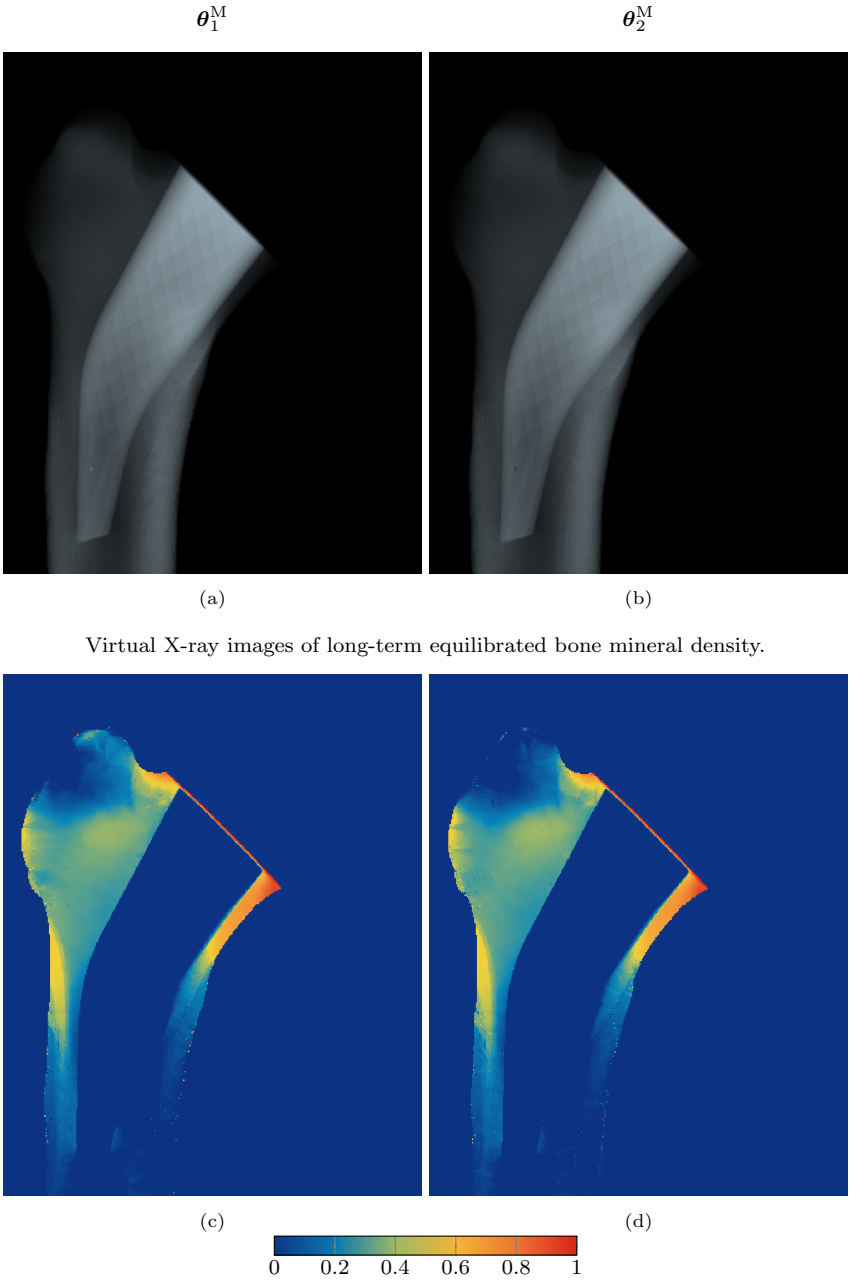

Figure 11.5: Exemplary results of six-dimensional parametric study.

Chapter 12

Conclusion and outlook

The overall objective of this thesis was to provide a comprehensive modeling approach that predicts secondary and long-term stability in total hip arthroplasty, including different patient individual characteristics and all possible protheses positions within a physically admissible range. This modeling approach was provided in chapter 10, first using an abstract full model, which was found to be computationally unfeasible. For this reason, a reduced model has been derived with the use of a response surface surrogate model, which renders the problem computationally feasible. Hereby, the full model is resembled by a number of deterministic simulation calls. Each deterministic simulation call can be divided into four distinct parts: automatic model generation, virtual X-ray generation, bone remodeling, and simulation of osseointegration.

The automatic model generation was carried out with the help of FreeCAD and Gmsh. This was readily possible due to their in-built scripting interfaces. It is noted that within this thesis, no proprietary software was used at all and the automatic model generation is the only part where third-party software was used. Here, FreeCAD and Gmsh were chosen because of their open-source software philosophy.

Conclusions are often hard to infer from finite element results for non-engineers. Therefore, complexity was reduced, and interpretability was facilitated by a novel virtual X-ray simulation approach for finite element results. Hereby, the finite element mesh is divided into a hierarchy of successively finer tight-fitting oriented bounding boxes. Subsequently, ray casting is performed on the tree of oriented bounding boxes first to pre-select finite element candidates, which are ray casted thereafter. By that, the non-linear problem of ray casting a finite element of higher polynomial order has to be solved for only a small fraction of all finite elements. This procedure resulted in high-quality virtual radiographs, even if the geometry is represented by only a few elements (see example 6.7.1).

Bone remodeling was described with the help of the theory of thermodynamic open systems and carried out as a finite element material model following the guidelines of thermodynamically consistent material modeling, as described in de Souza Neto et al. [2011]. This resulted in an accurate, efficient, and reliable implementation of bone remodeling.

The same approach was applied for the simulation of osseointegration: the principles of bone remodeling were translated to a contact interface between bone and prosthesis and combined with a micro-motion threshold. This was done by the restriction to small deformation, an assumption commonly made in the simulation of bone remodeling. By that, the contact interface could be carried out as a *node-to-node* contact interface, facilitating the introduction of constitutive relations within the interface since advection does not need to be considered. This ultimately resulted in a geometrically accurate and thermodynamically consistent description of the constitutive relations within the interface.

It is stated that great care was taken in the reliable and efficient implementation of the latter three methods within a self-developed finite element framework since this was a prerequisite

for performing larger-scale parametric simulations.
The response surface is built by the adaptive-sparse grid collocation method. The basis of the adaptive grid is assembled by local Lagrangian basis functions. Although convergence is inferior to the global Lagrangian approach, the use of local basis functions was highly beneficial in the development process since modeling or implementation errors were often readily visible as kinks on the response surface.
In conclusion, it can be stated that a framework simulating the changes in bone mineral density following total hip arthroplasty in a holistic approach at this level of detail was not available in the scientific literature, as well as the combination of a deterministic biomechanical framework with parametric computations with this variety of parametric dimensions.

12.1 Capabilities and limitations of the presented approach

The overall motivation for this thesis was to move one step forward to the genuinely beneficial introduction of digital tools and the higher precision that comes with them into surgical planning. It was stated in the introduction that to make good use of the increased accuracy of the prosthesis position, the surgeon must be able to estimate how these changes will affect long-term stability. Within this thesis, this can now be regarded as accomplished since after sampling the parametric state-space with the help of the surrogate model, a simulation result is available for **every possible prosthesis position** without the need for further computation. That being said, it has to be mentioned that for practical use, every single method used here, and subsequently, the complete parametric framework, needs configuration and clinical validation. To make it accessible for testing, every single method was designed and developed with its utilization as a stand-alone application in mind. Thereby, it is possible to replace a method if it fails clinical validation or a better method is available. And both of the latter are possible since, during the development process, many choices had to be made which are hard to justify without clinical validation. If such choices were to be made, two principles were applied: (1) physical reasoning and (2) the basic idea to retain the complexity of the problem as far as possible. So given another solution method arises, it probably does not affect the computability of the framework, in general.
Referring to the objective, the primary capability of this framework is to provide a prediction for secondary and long-term stability for arbitrary prothesis positions within a predefined range. But also parts of this framework could be combined or used individually to provide either deterministic or, in combination with the sparse-grid surrogate model, parametric predictions in biomechanics. All parameters of each method are exposed to the top level, which makes it easy to exchange the parameters that are included in the parametric calculation. By that, a multitude of numeric analyses is possible with the developed framework.
Despite the efficient sparse-grid sampling of the parametric state-space, the most significant limitation is still the curse of dimension. It is questionable if prediction in biomechanical compatibility of total hip arthroplasty, with the modeling approach presented here, is, in fact, cost-efficient for a larger number of dimensions ($\gtrapprox 5$) anywhere in the near future. Nevertheless, the framework can be used in a higher number of parametric dimensions in order to analyze the response surface for efficient reduction of parametric dimensions by eliminating less sensitive parameters. Furthermore, if a response surface is generated, it can be efficiently used for various sensitivity analyses and determination of extremal points, for example.
Another limitation of the framework so far is the modeling procedure. The input CAD geometries, obtained from CT data, are not of the best quality, and there is not much space for variation of the prosthesis position available in the first place. If deviations from the initial position are too large, applying boolean operations within FreeCAD might result in possible intersecting or overlapping Bezier splines, which cannot be meshed by gmsh. This further reduces the space for variation. Possible solutions to this problem are: create better input geometries, exchange the complete modeling procedure by something less error-prone, or maybe

these problems are simply no longer prominent in future versions of the actively developed open-source projects FreeCAD, Gmsh, and Open Cascade.

12.2 Further research

As mentioned above, this framework and each method used here require configuration and clinical validation if it is to be used in clinical practice. Each method on its own could also need further research efforts. The automatic model generation could be further investigated and combined with approaches for parametric prostheses design, such as Saravana Kumar and Gupta [2011] or Tabaković et al. [2014]. As a result, a framework for the optimal patient-specific prostheses design could be established. Predictions for a larger set of individuals could be provided if a parameterized model for the femur itself could be found.
The virtual X-ray imaging approach lends itself perfectly to parallelization and, in addition, could be performed on the GPU since ray casting is an operation commonly done by GPUs. This was not needed in the scope of this thesis since the generation of the X-ray barely carried weight in a deterministic simulation call.
Tests have suggested that the noise on the response surface is mainly caused by applying boundary conditions and the choice of a quantity of interest. Thereby, boundary conditions were used with the assumption that the transmission of forces remains physiological after the implantation. In the following, this was reduced to the equivalence of forces and moments with respect to the center point of the prosthesis surface. This could be improved by demanding equivalence of forces and moments in the complete prosthesis surface. An alternative approach would be to actually simulate the effect on the transmission of forces due to the altered conditions with the help of a dynamic multi-body model, as shown in Heller et al. [2001] or Kähler et al. [2010], for example, and subsequently finding its static equivalent. The quantity of interest, which was chosen here for the sake of simplicity as the percentage loss in three predefined rotated boxes near the prosthesis, could be improved as well. For example, the change in bone mineral density could be measured in the *seven zones according to Gruen* [Sarmiento and Gruen, 1985]. Therefore, these zones would have to be identified in virtual X-ray images, a problem the solution of which could be found by *digital image processing*.
For the simulation of the osseointegration, the same boundary conditions as for bone remodeling were used. It is worth investigating, if a single static-equivalent load case is sufficient to represent the process of osseointegration or if more load cases should be introduced and averaged according to equation (7.1).
Since the coating length of the prosthesis was included in the automatic model generation but not used as a parameter for the sparse grid, the study of the influence of the coating length on the long-term stability would be readily possible.
This parametric framework can be translated into a stochastic framework by only small alterations. If for all input parameters a probability density function is known, an output cumulative distribution function can be generated with the help of the response surface. As already mentioned, to account for an uncertain prosthesis position, an approach describing the statistics of orientation [see among others Downs, 1972, Mardia, 1975, Habeck, 2009] has to be included. Since the modeling approach described in chapter 10 can be altered quite simply, it is conceivable to address different stochastic problems, for example, the problem of bone remodeling under uncertain boundary conditions. Finally, it shall be mentioned that conducting stochastic simulations without a clinically validated parametric framework is a purely academic exercise, which again highlights the need for clinical validation.
Finally, the model needs further refinement for cost-efficient application where dimensional adaptivity of the sparse grid, as shown in Jakeman and Roberts [2011], surely has the greatest potential.

Chapter 13

Appendix

In this thesis an attempt has been made to use a notation that is familiar to most readers. Nevertheless, notations, symbols, and syntax used throughout this thesis shall be introduced in the following.

13.1 Notation

In the following, a list with notations used throughout this thesis shall be compiled:

$a, A, \alpha, \mathrm{a}, \mathrm{A}, ...$	Scalars, constants, indicies
$\boldsymbol{a}, \boldsymbol{A}, ...$	Vectors, multi-indices,
$a_i, A_i, ...$	Components of vectors,
$\mathbf{a}, \mathbf{A}, ...$	Tensors, matrices,
$\mathrm{a}_{ij}, \mathrm{A}_{ij}, \mathrm{a}_{ijk}, \mathrm{A}_{ijkl}, ...$	Components of tensors or matrices,
$a_{(n)}, \boldsymbol{a}_{(n)}, \mathbf{A}_{(n)}, ...$	Quantity (scalar, vector, tensor,...) at timestep n
$\tilde{\mathbf{a}}$,	Voigt notated symmetric tensor,
$\mathbf{I}$,	Identity tensor of order 2,
$\mathbb{I}$,	Identity tensor of order 4,
$\mathbf{A}^{\mathrm{T}}$ (with components $\mathrm{A}_{ij} = (\mathrm{A}^{\mathrm{T}})_{ji}$),	Transposition of a tensor or matrix,
δ_{ij},	Kronkecker delta,
$\mathbb{C}$,	Material tensor of order 4,
ϱ,	Bone mineral density,
ϱ_0,	Initial value of bone mineral density,
ρ,	Osseointegration degree,
t_0,	Start time of the simulation,
T,	End time of the simulation,
Δt,	time increment,
$\mathcal{B}$,	A body in the current configuration,
$\mathcal{B}_0$,	A body in the reference configuration,
$\partial\mathcal{B}$,	Boundary domain of body $\mathcal{B}$ and
$\mathbb{R}$,	Real numbers .

13.2 Definitions

In this section definitions, operators, and abbreviated expressions used throughout this thesis will be introduced in order to provide a concise and unique notation.

- Basic objects and rules of calculation might not be explained and no proofs will be given. For more information about vector and tensor calculus, the reader is referred to Hjelmstad

[2007].

- In general objects denoted by capital letters refer to the initial configuration and objects denoted by lowercase letters refer to the current configuration.
- Explicit expression of the arguments of functions can be omitted for readers convenience if dependencies are clear from the context.
- If no "dot" is written between two non-scalar objects, matrix multiplication rules apply.

13.2.1 Einstein's summation convention

If a subscript occurs twice in a product, summation of that term overall values of the index is implied, if not stated else in advance.
Example:

$$\boldsymbol{a}, \boldsymbol{b} \in \mathbb{R}^3 : \quad a_i b_i = a_1 b_1 + a_2 b_2 + a_3 b_3 \,. \tag{13.1}$$

13.2.2 Tensor product of two vectors

Let $\boldsymbol{a}, \boldsymbol{b} \in \mathbb{R}^n$ be two vectors. The tensor product, also referred to as dyadic product, of $\boldsymbol{a} = a_i \boldsymbol{e}_i$ and $\boldsymbol{b} = b_i \boldsymbol{e}_i$ is then given by

$$\mathbf{S} = \boldsymbol{a} \otimes \boldsymbol{b} = a_i b_j \boldsymbol{e}_i \otimes \boldsymbol{e}_j \,, \tag{13.2}$$

and the result is a tensor $\mathbf{S} = S_{ij} \boldsymbol{e}_i \otimes \boldsymbol{e}_j$.

13.2.3 Dot products

Beside the standard scalar product between two scalar entities, several other dot products can be defined. All non-standard dot products used throughout this thesis are defined below.

Vector-vector dot product:

$$\boldsymbol{a}, \boldsymbol{b} \in \mathbb{R}^n : \quad s = \boldsymbol{a} \cdot \boldsymbol{b} = a_i b_i \,. \tag{13.3}$$

Tensor-tensor double-dot product: Let $\mathbf{a} = \mathrm{a}_{ij} \boldsymbol{e}_i \otimes \boldsymbol{e}_j$ and $\mathbf{b} = \mathrm{b}_{ij} \boldsymbol{e}_i \otimes \boldsymbol{e}_j$ be two tensors of order two. Then the scalar result s of the double contraction $\mathbf{a} : \mathbf{b}$ is defined by

$$s = \mathbf{a} : \mathbf{b} = \mathrm{a}_{ij} \mathrm{b}_{ij} \,. \tag{13.4}$$

Let $\mathbb{C} = \mathbb{C}_{ijkl} \boldsymbol{e}_i \otimes \boldsymbol{e}_j \otimes \boldsymbol{e}_k \otimes \boldsymbol{e}_l$ be a tensor of order four and $\mathbf{a} = \mathrm{a}_{ij} \boldsymbol{e}_i \otimes \boldsymbol{e}_j$ a tensor of order two. Then the double contraction is defined by

$$\mathbf{b} = \mathbb{C} : \mathbf{a} = \mathbb{C}_{ijmn} \mathrm{a}_{mn} \boldsymbol{e}_i \otimes \boldsymbol{e}_j \,, \tag{13.5}$$

and the result $\mathbf{b} = \mathrm{b}_{ij} \boldsymbol{e}_i \otimes \boldsymbol{e}_j$ is a tensor of order two.

Tensor-vector dot product: Let $\mathbf{A} = \mathrm{A}_{ij} \boldsymbol{e}_i \otimes \boldsymbol{e}_j$ be a tensor of order two and $\boldsymbol{b} = b_i \boldsymbol{e}_i$ a vector of the same dimension. The tensor-vector dot product is defined by

$$\boldsymbol{c} = \mathbf{A} \cdot \boldsymbol{b} = b_k \mathrm{A}_{ij} \delta_{jk} \boldsymbol{e}_i \tag{13.6}$$

and the result is again a vector $\boldsymbol{c} = c_i \boldsymbol{e}_i$.

13.2.4 Derivatives

In the following, a notation for different derivatives for scalars, vectors, and tensors is introduced.

Gradient. The gradient of a scalar-valued differentiable function $f : \mathbb{R}^n \to \mathbb{R}$ is defined as

$$\mathrm{Grad}(f) = f_{,i}\boldsymbol{e}_i = \frac{\partial f}{\partial X_i}\boldsymbol{e}_i \,. \tag{13.7}$$

Similarly, the gradient of a vector-valued function $\boldsymbol{a}$ and a second-order tensor field $\mathbf{A}$ is defined as

$$\mathrm{Grad}(\boldsymbol{a}) = \frac{\partial(a_j\boldsymbol{e}_j)}{\partial X_i} \otimes \boldsymbol{e}_i = a_{j,i}\boldsymbol{e}_j \otimes \boldsymbol{e}_i = \frac{\partial a_j}{\partial X_i}\boldsymbol{e}_j \otimes \boldsymbol{e}_i \tag{13.8}$$

and

$$\mathrm{Grad}(\mathbf{A}) = \frac{\partial(\mathrm{A}_{jk}\boldsymbol{e}_j \otimes \boldsymbol{e}_k)}{\partial X_i} \otimes \boldsymbol{e}_i = \mathrm{A}_{jk,i}\boldsymbol{e}_j \otimes \boldsymbol{e}_k \otimes \boldsymbol{e}_i = \frac{\partial \mathrm{A}_{jk}}{\partial X_i}\boldsymbol{e}_j \otimes \boldsymbol{e}_k \otimes \boldsymbol{e}_i \,, \tag{13.9}$$

respectively.

Divergence. The divergence of a vector-valued function $\boldsymbol{a}$ in cartesian coordinates is the scalar-valued function $\mathrm{Div}(\boldsymbol{a})$ defined by

$$\mathrm{Div}(\boldsymbol{a}) = \frac{\partial a_i}{\partial X_i} = a_{i,i} \,. \tag{13.10}$$

Subsequently, the divergence of a second-order tensor field is the first-order tensor field given by

$$\mathrm{Div}(\mathbf{A}) = \frac{\partial \mathrm{A}_{ki}}{\partial X_k}\boldsymbol{e}_i = \mathrm{A}_{ki,k}\boldsymbol{e}_i \,. \tag{13.11}$$

13.2.5 Voigt notation for symmetric tensors

For symmetric tensors, there exists a condensed representation called *Voigt notation* [Voigt et al., 1928], which is particularly useful in numerical implementation of continuum mechanic frameworks. Thereby, the order of a symmetric tensor is reduced, i.e., a symmetric second-order tensor $\mathbf{a}$ is reduced to a vector[1] $\tilde{\mathbf{a}}$, and a fourth-order tensor $\mathbb{C}$ is reduced to a second-order tensor $\tilde{\mathbb{C}}$. In continuum mechanics, the precise notation is motivated by demanding equivalence of the following expressions:

$$\left.\begin{aligned} \boldsymbol{\sigma} &= \mathbb{C} : \boldsymbol{\varepsilon} \\ \psi &= \tfrac{1}{2\varrho}\boldsymbol{\sigma} : \boldsymbol{\varepsilon} \end{aligned}\right\} \Leftrightarrow \begin{cases} \tilde{\boldsymbol{\sigma}} = \tilde{\mathbb{C}} : \tilde{\boldsymbol{\varepsilon}} \\ \psi = \tfrac{1}{2\varrho}\tilde{\boldsymbol{\sigma}} : \tilde{\boldsymbol{\varepsilon}} \end{cases} . \tag{13.12}$$

[1] Despite $\tilde{\mathbf{a}}$ being a vector-like object, formally, we keep the notation of a tensor to indicate Voigt notation's nature as an exclusive matter of representation of tensors.

By that, the Cauchy stress tensor and the linearized strain can be re-written as follows

$$[\sigma_{ij}] = \begin{bmatrix} \sigma_{11} & \sigma_{12} & \sigma_{13} \\ & \sigma_{22} & \sigma_{23} \\ \text{sym.} & & \sigma_{33} \end{bmatrix} \Leftrightarrow [\tilde{\sigma}_i] = \begin{bmatrix} \sigma_{11} \\ \sigma_{22} \\ \sigma_{33} \\ \sigma_{12} \\ \sigma_{13} \\ \sigma_{23} \end{bmatrix}, \quad \text{and} \tag{13.13}$$

$$[\varepsilon_{ij}] = \begin{bmatrix} \varepsilon_{11} & \varepsilon_{12} & \varepsilon_{13} \\ & \varepsilon_{22} & \varepsilon_{23} \\ \text{sym.} & & \varepsilon_{33} \end{bmatrix} \Leftrightarrow [\tilde{\varepsilon}_i] = \begin{bmatrix} \varepsilon_{11} \\ \varepsilon_{22} \\ \varepsilon_{33} \\ 2\varepsilon_{12} \\ 2\varepsilon_{13} \\ 2\varepsilon_{23} \end{bmatrix}, \tag{13.14}$$

respectively. The material tensor then follows as

$$[\tilde{\mathbb{C}}_{ij}] = \begin{bmatrix} \tilde{\mathbb{C}}_{11} & \tilde{\mathbb{C}}_{12} & \tilde{\mathbb{C}}_{13} & \tilde{\mathbb{C}}_{14} & \tilde{\mathbb{C}}_{15} & \tilde{\mathbb{C}}_{16} \\ \tilde{\mathbb{C}}_{21} & \tilde{\mathbb{C}}_{22} & \tilde{\mathbb{C}}_{23} & \tilde{\mathbb{C}}_{24} & \tilde{\mathbb{C}}_{25} & \tilde{\mathbb{C}}_{26} \\ \tilde{\mathbb{C}}_{31} & \tilde{\mathbb{C}}_{32} & \tilde{\mathbb{C}}_{33} & \tilde{\mathbb{C}}_{34} & \tilde{\mathbb{C}}_{35} & \tilde{\mathbb{C}}_{36} \\ \tilde{\mathbb{C}}_{41} & \tilde{\mathbb{C}}_{42} & \tilde{\mathbb{C}}_{43} & \tilde{\mathbb{C}}_{44} & \tilde{\mathbb{C}}_{45} & \tilde{\mathbb{C}}_{46} \\ \tilde{\mathbb{C}}_{51} & \tilde{\mathbb{C}}_{52} & \tilde{\mathbb{C}}_{53} & \tilde{\mathbb{C}}_{54} & \tilde{\mathbb{C}}_{55} & \tilde{\mathbb{C}}_{56} \\ \tilde{\mathbb{C}}_{61} & \tilde{\mathbb{C}}_{62} & \tilde{\mathbb{C}}_{63} & \tilde{\mathbb{C}}_{64} & \tilde{\mathbb{C}}_{65} & \tilde{\mathbb{C}}_{66} \end{bmatrix} \tag{13.15}$$

$$= \begin{bmatrix} \mathbb{C}_{1111} & \mathbb{C}_{1122} & \mathbb{C}_{1133} & \mathbb{C}_{1123} & \mathbb{C}_{1113} & \mathbb{C}_{1112} \\ \mathbb{C}_{2211} & \mathbb{C}_{2222} & \mathbb{C}_{2233} & \mathbb{C}_{2223} & \mathbb{C}_{2213} & \mathbb{C}_{2212} \\ \mathbb{C}_{3311} & \mathbb{C}_{3322} & \mathbb{C}_{3333} & \mathbb{C}_{3323} & \mathbb{C}_{3313} & \mathbb{C}_{3312} \\ \mathbb{C}_{2311} & \mathbb{C}_{2322} & \mathbb{C}_{2333} & \mathbb{C}_{2323} & \mathbb{C}_{2313} & \mathbb{C}_{2312} \\ \mathbb{C}_{1311} & \mathbb{C}_{1322} & \mathbb{C}_{1333} & \mathbb{C}_{1323} & \mathbb{C}_{1313} & \mathbb{C}_{1312} \\ \mathbb{C}_{1211} & \mathbb{C}_{1222} & \mathbb{C}_{1233} & \mathbb{C}_{1223} & \mathbb{C}_{1213} & \mathbb{C}_{1212} \end{bmatrix}. \tag{13.16}$$

It is mentioned that the expressions (13.13), (13.14), (13.15) are just a choice in order to fulfill the requirement (13.12). There are several other choices, resulting in the *Mandel notation* or *Kelvin notation*, for example. Caution is advised if calculating quantities not depicted in (13.12): equivalence is generally not maintained, and translating Voigt-notated quantities back to the non-symmetric tensor notation is in most cases less cumbersome compared with introducing the proper scaling into the Voigt-notated expressions artificially.

13.2.6 Abbreviated expressions

To avoid long and complex formulas, abbreviated expressions will be used where it seems appropriate. A list of all abbreviated expressions is compiled in the following.

Derivative of a quantity:

$$\mathrm{D}_{\{\bullet\}}\{*\} = \frac{\mathrm{D}}{\mathrm{D}\{\bullet\}}\{*\}\,; \quad \text{example:} \quad \mathrm{D}_t\,\varrho = \frac{\mathrm{D}\varrho}{\mathrm{D}t}\,. \tag{13.17}$$

Partial derivative of a quantity:

$$\partial_{\{\bullet\}}\{*\} = \frac{\partial}{\partial\{\bullet\}}\{*\}\,; \quad \text{example:} \quad \partial_t\,\varrho = \frac{\partial\varrho}{\partial t}\,. \tag{13.18}$$

Bibliography

A. Abdulkarim, P. Ellanti, N. Motterlini, T. Fahey, and J. M. O'Byrne. Cemented versus uncemented fixation in total hip replacement: a systematic review and meta-analysis of randomized controlled trials. *Orthopedic reviews*, 5(1), 2013.

Y. Abols, H. Genant, D. Rosenfeld, C. Cann, B. Ettinger, and G. Gordan. Spinal bone-mineral determination using computerized tomography in patients, controls and phantoms. *American journal of roentgenology*, 131:548–549, 1978.

O. Ahmad, K. Ramamurthi, K. E. Wilson, K. Engelke, R. L. Prince, and R. H. Taylor. Volumetric DXA (VXA): a new method to extract 3d information from multiple in vivo DXA images. *Journal of bone and mineral research*, 25(12):2744–2751, 2010.

American Society of Mechanical Engineers. *Applied Mechanics Reviews*. Number 4-6 in 54. American Society of Mechanical Engineers, 2001. URL `https://books.google.de/books?id=-TqyKg44HKwC`.

D. N. Arnold, R. S. Falk, and R. Winther. Finite element exterior calculus, homological techniques, and applications. *Acta numerica*, 15:1–155, 2006.

M. J. Asher, B. F. Croke, A. J. Jakeman, and L. J. Peeters. A review of surrogate models and their application to groundwater modeling. *Water Resources Research*, 51(8):5957–5973, 2015.

S. Azhar. Building information modeling (BIM): Trends, benefits, risks, and challenges for the AEC industry. *Leadership and management in engineering*, 11(3):241–252, 2011.

I. Babuška, F. Nobile, and R. Tempone. A stochastic collocation method for elliptic partial differential equations with random input data. *SIAM Journal on Numerical Analysis*, 45(3): 1005–1034, 2007.

V. Baca, Z. Horak, P. Mikulenka, and V. Dzupa. Comparison of an inhomogeneous orthotropic and isotropic material models used for FE analyses. *Medical engineering & physics*, 30(7): 924–930, 2008.

M. T. Bah, P. B. Nair, M. Taylor, and M. Browne. Efficient computational method for assessing the effects of implant positioning in cementless total hip replacements. *Journal of biomechanics*, 44(7):1417–1422, 2011.

C. Barber, D. Dobkin, D. Dobkin, and H. Huhdanpaa. The quickhull algorithm for convex hulls. *ACM Transactions on Mathematical Software (TOMS)*, 22(4):469–483, 1996.

J. Baro, J. Sempau, J. Fernández-Varea, and F. Salvat. PENELOPE: an algorithm for Monte Carlo simulation of the penetration and energy loss of electrons and positrons in matter. *Nuclear Instruments and Methods in Physics Research Section B: Beam Interactions with Materials and Atoms*, 100(1):31–46, 1995.

Y. Basar and D. Weichert. *Nonlinear continuum mechanics of solids: fundamental mathematical and physical concepts*. Springer Science & Business Media, 2013.

K.-J. Bathe. *Finite element procedures*. Klaus-Jürgen Bathe, 2006.

L. E. Bayliss, D. Culliford, A. P. Monk, S. Glyn-Jones, D. Prieto-Alhambra, A. Judge, C. Cooper, A. J. Carr, N. K. Arden, D. J. Beard, et al. The effect of patient age at intervention on risk of implant revision after total replacement of the hip or knee: a population-based cohort study. *The Lancet*, 389(10077):1424–1430, 2017.

G. Beaupré, T. Orr, and D. Carter. An approach for time-dependent bone modeling and remodeling – application: A preliminary remodeling simulation. *Journal of Orthopaedic Research*, 8(5):662–670, 1990a.

G. Beaupré, T. Orr, and D. Carter. An approach for time-dependent bone modeling and remodeling – theoretical development. *Journal of Orthopaedic Research*, 8(5):651–661, 1990b.

A. K. Bedaka and C.-Y. Lin. CAD-based robot path planning and simulation using OPEN CASCADE. *Procedia computer science*, 133:779–785, 2018.

J. Bezanson, A. Edelman, S. Karpinski, and V. B. Shah. Julia: A fresh approach to numerical computing. *SIAM review*, 59(1):65–98, 2017.

J. Bradley, H. Huang, and R. Ledley. Evaluation of calcium concentration in bones from CT scans. *Radiology*, 128(1):103–107, 1978.

D. Braess. *Finite Elemente: Theorie, schnelle Löser und Anwendungen in der Elastizitätstheorie*. Springer-Verlag, 2013.

P.-I. Branemark. Osseointegrated implants in the treatment of the edentulous jaw. Experience from a 10-year period. *Scand. J. Plast. Reconstr. Surg. Suppl.*, 16, 1977.

J. T. Byrd. *Operative hip arthroscopy*. Springer Science & Business Media, 2012.

J. R. Cameron, R. B. Mazess, and J. A. Sorenson. Precision and accuracy of bone mineral determination by direct photon absorptiometry. *Investigative radiology*, 3(3):141–150, 1968.

C. E. Cann and H. K. Genant. Precise measurement of vertebral mineral content using computed tomography. *Journal of computer assisted tomography*, 4(4):493–500, 1980.

D. Carter, D. Fyhrie, and R. Whalen. Trabecular bone density and loading history: regulation of connective tissue biology by mechanical energy. *Journal of biomechanics*, 20(8):785–794, 1987.

D. Carter, T. Orr, and D. Fyhrie. Relationships between loading history and femoral cancellous bone architecture. *Journal of Biomechanics*, 22(3):231–244, 1989.

D. R. Carter and W. C. Hayes. The compressive behavior of bone as a two-phase porous structure. *The Journal of bone and joint surgery. American volume*, 59(7):954–962, 1977.

P. Cattaneo, M. Dalstra, and L. H. Frich. A three-dimensional finite element model from computed tomography data: a semi-automated method. *Proceedings of the Institution of Mechanical Engineers, Part H: Journal of Engineering in Medicine*, 215(2):203–212, 2001.

J. Céa. Approximation variationnelle des problèmes aux limites. In *Annales de l'institut Fourier*, volume 14:2, pages 345–444, 1964.

B. Cerfontaine, A.-C. Dieudonné, J.-P. Radu, F. Collin, and R. Charlier. 3d zero-thickness coupled interface finite element: Formulation and application. *Computers and Geotechnics*, 69:124–140, 2015.

J.-D. Chang, I.-S. Kim, A. M. Bhardwaj, and R. N. Badami. The evolution of computer-assisted total hip arthroplasty and relevant applications. *Hip & pelvis*, 29(1):1–14, 2017.

R. Chidambaram and A. Cobb. Change in the age distribution of patients undergoing primary hip and knee preplacement over 13 years – an increase in the number of younger men having hip surgery. In *Orthopaedic Proceedings*, volume 91, pages 152–152. The British Editorial Society of Bone & Joint Surgery, 2009.

Y. Chien and K.-S. Fu. On the generalized Karhunen-Loève expansion (corresp.). *IEEE Transactions on Information Theory*, 13(3):518–520, 1967.

P. G. Constantine. *Active subspaces: Emerging ideas for dimension reduction in parameter studies*, volume 2. SIAM, 2015.

S. Cowin and D. Hegedus. Bone remodeling I: theory of adaptive elasticity. *Journal of Elasticity*, 6(3):313–326, 1976.

S. C. Cowin and S. B. Doty. *Tissue mechanics*. Springer Science & Business Media, 2007.

J. D. Currey. The relationship between the stiffness and the mineral content of bone. *Journal of biomechanics*, 2(4):477–480, 1969.

J. D. Currey. *The mechanical adaptations of bones*. Princeton University Press, 2014.

J. A. Davila, M. J. Kransdorf, and G. P. Duffy. Surgical planning of total hip arthroplasty: accuracy of computer-assisted endomap software in predicting component size. *Skeletal radiology*, 35(6):390–393, 2006.

R. Day and D. Potts. Zero thickness interface elements – numerical stability and application. *International Journal for numerical and analytical methods in geomechanics*, 18(10):689–708, 1994.

E. A. de Souza Neto, D. Peric, and D. R. Owen. *Computational methods for plasticity: theory and applications*. John Wiley & Sons, 2011.

C. Dick, J. Georgii, R. Burgkart, and R. Westermann. Computational steering for patient-specific implant planning in orthopedics. In *VCBM*, pages 83–92, 2008.

C. Dick, J. Georgii, R. Burgkart, and R. Westermann. Stress tensor field visualization for implant planning in orthopedics. *IEEE Transactions on Visualization and Computer Graphics*, 15(6):1399–1406, 2009.

M. Dittmann. *Isogeometric analysis and hierarchical refinement for multi-field contact problems*, volume 4. KIT Scientific Publishing, 2017.

C. Dopico-González, A. M. New, and M. Browne. Probabilistic analysis of an uncemented total hip replacement. *Medical engineering & physics*, 31(4):470–476, 2009.

J. Douglas and T. Dupont. A finite element collocation method for quasilinear parabolic equations. *mathematics of computation*, 27(121):17–28, 1973.

T. D. Downs. Orientation statistics. *Biometrika*, 59(3):665–676, 1972.

V. Dubourg, B. Sudret, and J.-M. Bourinet. Reliability-based design optimization using kriging surrogates and subset simulation. *Structural and Multidisciplinary Optimization*, 44(5):673–690, 2011.

J. Duyck, K. Vandamme, L. Geris, H. Van Oosterwyck, M. De Cooman, J. Vandersloten, R. Puers, and I. Naert. The influence of micro-motion on the tissue differentiation around immediately loaded cylindrical turned titanium implants. *Archives of oral biology*, 51(1):1–9, 2006.

M. Epstein and G. A. Maugin. Thermomechanics of volumetric growth in uniform bodies. *International Journal of Plasticity*, 16(7-8):951–978, 2000.

E. F. Eriksen. Cellular mechanisms of bone remodeling. *Reviews in Endocrine and Metabolic Disorders*, 11(4):219–227, 2010.

A. Ern and J.-L. Guermond. *Theory and practice of finite elements*, volume 159. Springer Science & Business Media, 2013.

D. T. Felson. Epidemiology of hip and knee osteoarthritis. *Epidemiologic reviews*, 10:1–28, 1988.

X. Feng. Chemical and biochemical basis of cell-bone matrix interaction in health and disease. *Current chemical biology*, 3(2):189–196, 2009.

B. A. Finlayson. *The method of weighted residuals and variational principles*, volume 73. SIAM, 2013.

R. A. Frazer, W. N. P. Jones, and S. W. Skan. *Approximations to functions and to the solutions of differential equations*. HSMO, 1937.

Fred the Oyster. Skeletal pelvis-pubis. Licensed under CC BY-SA 4.0 (`https://creativecommons.org/licenses/by-sa/4.0`), 2014. URL `https://commons.wikimedia.org/wiki/File:Skeletal_pelvis-pubis.svg`.

N. Freud, P. Duvauchelle, J. Létang, and D. Babot. Fast and robust ray casting algorithms for virtual X-ray imaging. *Nuclear Instruments and Methods in Physics Research Section B: Beam Interactions with Materials and Atoms*, 248(1):175–180, 2006.

H. Frost. The Utah Paradigm of Skeletal Physiology. *ISMNI*, 1960.

X. Gao, M. Fraulob, and G. Haïat. Biomechanical behaviours of the bone-implant interface: a review. *Journal of the Royal Society Interface*, 16(156):20190259, 2019.

J. M. Garcia-Aznar, T. Rüberg, and M. Doblare. A bone remodelling model coupling microdamage growth and repair by 3D BMU-activity. *Biomechanics and modeling in mechanobiology*, 4(2-3):147–167, 2005.

R. L. Gates and M. R. Bittens. A multilevel adaptive sparse grid stochastic collocation approach to the non-smooth forward propagation of uncertainty in discretized problems. *arXiv preprint arXiv:1509.01462*, 2015.

L. Gaul and M. Mayer. Modeling of contact interfaces in built-up structures by zero-thickness elements. In *Conf. Proc.(CD ROM) IMAC XXVI: Conf. & Expo. on Str. Dyn*, 2008.

C. Geuzaine and J.-F. Remacle. Gmsh: A 3-D finite element mesh generator with built-in pre- and post-processing facilities. *International journal for numerical methods in engineering*, 79(11):1309–1331, 2009.

I. Gibson and M. F. Ashby. The mechanics of three-dimensional cellular materials. *Proceedings of the Royal Society of London. A. Mathematical and Physical Sciences*, 382(1782):43–59, 1982.

R. E. Goodman, R. L. Taylor, and T. L. Brekke. A model for the mechanics of jointed rock. *Journal of Soil Mechanics & Foundations Div*, 1968.

S. Gottschalk, M. Lin, and D. Manocha. Obbtree: A hierarchical structure for rapid interference detection. In *Proceedings of the 23rd annual conference on Computer graphics and interactive techniques*, pages 171–180. ACM, 1996.

L. Grassi, S. P. Väänänen, M. Ristinmaa, J. S. Jurvelin, and H. Isaksson. Prediction of femoral strength using 3D finite element models reconstructed from DXA images: validation against experiments. *Biomechanics and modeling in mechanobiology*, 16(3):989–1000, 2017.

R. Guldberg, S. Hollister, and G. Charras. The accuracy of digital image-based finite element models. *Journal of Biomechanical Engineering*, 120, 1998.

C. U. Gwam, J. B. Mistry, N. S. Mohamed, M. Thomas, K. C. Bigart, M. A. Mont, and R. E. Delanois. Current epidemiology of revision total hip arthroplasty in the United States: National Inpatient Sample 2009 to 2013. *The Journal of arthroplasty*, 32(7):2088–2092, 2017.

Y. Haba, T. Lindner, A. Fritsche, A.-K. Schiebenhöfer, R. Souffrant, D. Kluess, R. Skripitz, W. Mittelmeier, and R. Bader. Relationship between mechanical properties and bone mineral density of human femoral bone retrieved from patients with osteoarthritis. *The open orthopaedics journal*, 6:458, 2012.

M. Habeck. Generation of three-dimensional random rotations in fitting and matching problems. *Computational Statistics*, 24(4):719, 2009.

M. Haga, N. Fujii, K. Nozawa-Inoue, S. Nomura, K. Oda, K. Uoshima, and T. Maeda. Detailed process of bone remodeling after achievement of osseointegration in a rat implantation model. *The Anatomical Record: Advances in Integrative Anatomy and Evolutionary Biology: Advances in Integrative Anatomy and Evolutionary Biology*, 292(1):38–47, 2009.

Z.-H. Han and S. Görtz. Hierarchical kriging model for variable-fidelity surrogate modeling. *AIAA journal*, 50(9):1885–1896, 2012.

T. Harrigan and J. Hamilton. Optimality conditions for finite element simulation of adaptive bone remodeling. *International journal of solids and structures*, 29(23):2897–2906, 1992.

W. Hayes and B. Snyder. Correlations between stress and morphology in trabecular bone of the patella. In *Proceedings of the 25th Annual Meeting of the Orthopaedic Research Society*, volume 88. ORS Chicago, 1979.

W. Hayes, B. Snyder, B. Levine, and S. Ramaswamy. *Stress-morphology relationships in trabecular bone of the patella*, volume 12. Wiley, Chichester, 1982.

D. Hegedus and S. Cowin. Bone remodeling II: small strain adaptive elasticity. *Journal of elasticity*, 6(4):337–352, 1976.

S. Heinrich. Multilevel monte carlo methods. In *International Conference on Large-Scale Scientific Computing*, pages 58–67. Springer, 2001.

M. Heller, G. Bergmann, G. Deuretzbacher, L. Dürselen, M. Pohl, L. Claes, N. Haas, and G. Duda. Musculo-skeletal loading conditions at the hip during walking and stair climbing. *Journal of biomechanics*, 34(7):883–893, 2001.

K. D. Hjelmstad. *Fundamentals of structural mechanics*. Springer Science & Business Media, 2007.

G. C. Hsiao, P. Kopp, and W. L. Wendland. A Galerkin collocation method for some integral equations of the first kind. *Computing*, 25(2):89–130, 1980.

H. Huang, F. Suarez, T. Toridis, K. Khonozeimeh, and L. Ovenshire. Utilization of computerized tomographic scans as input to finite element analysis. In *International Conference Procedings: Finite Element in Biomechanics*, volume 2, pages 797–815, 1980.

R. Huiskes. Stress shielding and bone resorption in THA: clinical versus computer-simulation studies. *Acta Orthop Belg*, 59(Suppl 1):118–129, 1993.

L. Humbert, Y. Martelli, R. Fonollà, M. Steghöfer, S. Di Gregorio, J. Malouf, J. Romera, and L. M. D. R. Barquero. 3D-DXA: assessing the femoral shape, the trabecular macrostructure and the cortex in 3D from DXA images. *IEEE transactions on medical imaging*, 36(1):27–39, 2016.

Y. Inaba, H. Ike, M. Oba, and T. Saito. Evaluation of adaptive bone remodeling after total hip arthroplasty using finite element analysis. *Perusal of the Finite Element Method*, page 213, 2016.

C. Jacobs, M. Levenston, G. Beaupré, J. Simo, and D. Carter. Numerical instabilities in bone remodeling simulations: the advantages of a node-based finite element approach. *Journal of biomechanics*, 28(4):449–459, 1995.

J. D. Jakeman and S. G. Roberts. Local and dimension adaptive sparse grid interpolation and quadrature. *arXiv preprint arXiv:1110.0010*, 2011.

P. Jolbäck, O. Rolfson, M. Mohaddes, S. Nemes, J. Kärrholm, G. Garellick, and H. Lindahl. Does surgeon experience affect patient-reported outcomes 1 year after primary total hip arthroplasty? A register-based study of 6,713 cases in western Sweden. *Acta orthopaedica*, 89(3):265–271, 2018.

I. Jolliffe. *Principal component analysis*. Springer, 2011.

D. R. Jones. A taxonomy of global optimization methods based on response surfaces. *Journal of global optimization*, 21(4):345–383, 2001.

H. Kadner. Untersuchungen zur Kollokationsmethode. *ZAMM-Journal of Applied Mathematics and Mechanics/Zeitschrift für Angewandte Mathematik und Mechanik*, 40(1-3):99–113, 1960.

M. Kähler, R. Rachholz, S. Herrmann, J. Zierath, R. Souffrant, D. Kluess, R. Bader, and C. Woernle. Development of a biomechanical multibody model for the hardware-in-the-loop simulation of total hip endoprostheses. In *Proceedings of the 1st Joint international conference on multibody system dynamics. Lappeenranta (Finland)*, 2010.

M. M. Kajotoni. *A comparative study of collocation methods for the numerical solution of differential equations*. PhD thesis, Citeseer, 2008.

N.-B. Kandala, M. Connock, R. Pulikottil-Jacob, P. Sutcliffe, M. J. Crowther, A. Grove, H. Mistry, and A. Clarke. Setting benchmark revision rates for total hip replacement: analysis of registry evidence. *Bmj*, 350:h756, 2015.

Y. Kang, H. Park, Y. Youm, I. Lee, M. Ahn, and J. Ihn. Three dimensional shape reconstruction and finite element analysis of femur before and after the cementless type of total hip replacement. *Journal of biomedical engineering*, 15(6):497–504, 1993.

J. L. Katz. Hard tissue as a composite material – I. Bounds on the elastic behavior. *Journal of biomechanics*, 4(5):455–473, 1971.

J. L. Katz. Anisotropy of Young's modulus of bone. *Nature*, 283(5742):106–107, 1980.

T. Kay and J. Kajiya. Ray tracing complex scenes. In *ACM SIGGRAPH computer graphics*, volume 20(4), pages 269–278. ACM, 1986.

J. Keyak, J. Meagher, H. Skinner, and C. Mote Jr. Automated three-dimensional finite element modelling of bone: a new method. *Journal of biomedical engineering*, 12(5):389–397, 1990.

A. I. Khuri and S. Mukhopadhyay. Response surface methodology. *Wiley Interdisciplinary Reviews: Computational Statistics*, 2(2):128–149, 2010.

T. Kim. Frequency-domain Karhunen-Loève method and its application to linear dynamic systems. *AIAA journal*, 36(11):2117–2123, 1998.

Y. Klausner. *Fundamentals of continuum mechanics of soils*. Springer Science & Business Media, 2012.

N. K. Knowles, J. M. Reeves, and L. M. Ferreira. Quantitative computed tomography (QCT) derived bone mineral density (BMD) in finite element studies: a review of the literature. *Journal of experimental orthopaedics*, 3(1):36, 2016.

E. Kuhl. *Theory and Numerics of Open System Continuum Thermodynamics: Spatial and Material Setting*. Universität Kaiserslautern, 2004.

E. Kuhl and P. Steinmann. Mass- and volume-specific views on thermodynamics for open systems. *Proceedings of the Royal Society of London. Series A: Mathematical, Physical and Engineering Sciences*, 459(2038):2547–2568, 2003.

E. Kuhl, A. Menzel, and P. Steinmann. Computational modeling of growth. *Computational Mechanics*, 32(1-2):71–88, 2003.

G. Labek, M. Thaler, W. Janda, M. Agreiter, and B. Stöckl. Revision rates after total joint replacement: cumulative results from worldwide joint register datasets. *The Journal of Bone and Joint Surgery. British Volume*, 93(3):293–297, 2011.

R. Lam, D. L. Allaire, and K. E. Willcox. Multifidelity optimization using statistical surrogate modeling for non-hierarchical information sources. In *56th AIAA/ASCE/AHS/ASC Structures, Structural Dynamics, and Materials Conference*, page 0143, 2015.

R. Lattanzi, M. Viceconti, C. Zannoni, P. Quadrani, and A. Toni. Hip-op: an innovative software to plan total hip replacement surgery. *Medical informatics and the internet in medicine*, 27(2):71–83, 2002.

T. A. Laursen. *Computational contact and impact mechanics: fundamentals of modeling interfacial phenomena in nonlinear finite element analysis*. Springer Science & Business Media, 2013.

C. Lavecchia, D. Espino, K. Moerman, K. Tse, D. Robinson, P. Lee, and D. Shepherd. Lumbar model generator: a tool for the automated generation of a parametric scalable model of the lumbar spine. *Journal of the Royal Society Interface*, 15(138):20170829, 2018.

P. Lax and A. Milgram. Parabolic equations: Contributions to the theory of partial differential equations. 1954. *Annals of mathematical studies*, 1954.

L. Le Gratiet, S. Marelli, and B. Sudret. *Metamodel-based sensitivity analysis: polynomial chaos expansions and Gaussian processes*, chapter 38, pages 1289–1325. Springer International Publishing, 2017. Cham, Switzerland.

M. Listgarten, N. Lang, H. Schroeder, and A. Schroeder. Periodontal tissues and their counterparts around endosseous implants. *Clinical oral implants research*, 2(1):1–19, 1991.

D. Lühmann, B. Hauschild, and H. Raspe. *Hüftgelenkendoprothetik bei Osteoarthrose: eine Verfahrensbewertung*. Nomos-Verlag-Ges., 2000.

Y. Luo, S. Ahmed, and W. D. Leslie. Automation of a DXA-based finite element tool for clinical assessment of hip fracture risk. *Computer methods and programs in biomedicine*, 155:75–83, 2018.

A. Lutz. *Ein integrales Modellierungskonzept zur numerischen Simulation der Osseointegration und Langzeitstabilität von Endoprothesen*. IBNM, 2011.

A. Lutz and U. Nackenhorst. Computation of static-equivalent load sets for bone remodeling simulation. In *PAMM: Proceedings in Applied Mathematics and Mechanics*, volume 7(1), pages 4020007–4020008. Wiley Online Library, 2007.

A. Lutz and U. Nackenhorst. Numerical investigations on the osseointegration of uncemented endoprostheses based on bio-active interface theory. *Computational Mechanics*, 50(3):367–381, 2012.

X. Ma and N. Zabaras. An adaptive hierarchical sparse grid collocation algorithm for the solution of stochastic differential equations. *Journal of Computational Physics*, 228(8):3084–3113, 2009.

L. E. Malvern. *Introduction to the Mechanics of a Continuous Medium*. Addison-Wesley Publishing Company, 1965.

K. V. Mardia. Statistics of directional data. *Journal of the Royal Statistical Society: Series B (Methodological)*, 37(3):349–371, 1975.

L. Mehrez and M. Browne. A numerically validated probabilistic model of a simplified total hip replacement construct. *Computer methods in biomechanics and biomedical engineering*, 15(8):845–858, 2012.

S. Mellon and K. Tanner. Bone and its adaptation to mechanical loading: a review. *International Materials Reviews*, 57(5):235–255, 2012.

B. Merz, R. Müller, and P. Rüegsegger. Solid modeling and finite element modeling of bones and implant-bone systems. In *Interfaces in Medicine and Mechanics—2*, pages 319–328. Springer, 1991.

B. C. Moffett Jr, L. C. Johnson, J. B. McCabe, and H. C. Askew. Articular remodeling in the adult human temporomandibular joint. *American Journal of Anatomy*, 115(1):119–141, 1964.

T. Möller and B. Trumbore. Fast, minimum storage ray/triangle intersection. In *ACM SIGGRAPH 2005 Courses*, page 7. ACM, 2005.

L. Monfils. X-ray of a total hip protesis left. Licensed under CC BY-SA 3.0 (`https://creativecommons.org/licenses/by/3.0/legalcode`), 2011. URL `https://commons.wikimedia.org/wiki/File:X-ray_of_a_Total_Hip_Protesis_left.jpg`.

P. Moreo, M. Pérez, J. García-Aznar, and M. Doblaré. Modelling the mechanical behaviour of living bony interfaces. *Computer Methods in Applied Mechanics and Engineering*, 196 (35-36):3300–3314, 2007.

E. F. Morgan, H. H. Bayraktar, and T. M. Keaveny. Trabecular bone modulus – density relationships depend on anatomic site. *Journal of biomechanics*, 36(7):897–904, 2003.

S. Mori and D. Burr. Increased intracortical remodeling following fatigue damage. *Bone*, 14 (2):103–109, 1993.

U. K. Munzinger, J. G. Boldt, and P. A. Keblish. *Primary knee arthroplasty*. Springer Science & Business Media, 2004.

U. Nackenhorst, N. Krstin, and R. Lammering. A constitutive law for anisotropic stress adaptive bone remodeling. *ZAMM-Journal of Applied Mathematics and Mechanics/Zeitschrift für Angewandte Mathematik und Mechanik*, 80(S2):399–400, 2000.

A. N. Natali, E. A. Meroi, K. R. Williams, and L. Calabrese. Investigation of the integration process of dental implants by means of a numerical analysis. *Dental Materials*, 13(5-6): 325–332, 1997.

F. H. Netter, S. Colacino, et al. *Atlas of human anatomy*. Ciba-Geigy Corporation, 1989.

J. Newman. *An improved method of collocation for the stress analysis of cracked plates with various shaped boundaries*. National Aeronautics and Space Administration, 1971.

S. Nobakhti and S. J. Shefelbine. On the relation of bone mineral density and the elastic modulus in healthy and pathologic bone. *Current osteoporosis reports*, 16(4):404–410, 2018.

F. Nobile, R. Tempone, and C. G. Webster. A sparse grid stochastic collocation method for partial differential equations with random input data. *SIAM Journal on Numerical Analysis*, 46(5):2309–2345, 2008.

K. L. Ong, E. Lau, J. Suggs, S. M. Kurtz, and M. T. Manley. Risk of subsequent revision after primary and revision total joint arthroplasty. *Clinical Orthopaedics and Related Research*, 468(11):3070–3076, 2010.

OpenStax. 0910 Oateoarthritis Hip. Licensed under CC BY 4.0 (`https://creativecommons.org/licenses/by/4.0`), 2016. URL `https://commons.wikimedia.org/wiki/File:0910_Oateoarthritis_Hip.jpg`.

OpenStax College. 810 Femur and Patella. Licensed under CC BY 3.0 (`https://creativecommons.org/licenses/by/3.0/legalcode`), 2013. URL `https://commons.wikimedia.org/wiki/File:810_Femur_and_Patella.jpg`.

R. V. O'Toole III, B. Jaramaz, A. M. DiGioia III, C. D. Visnic, and R. H. Reid. Biomechanics for preoperative planning and surgical simulations in orthopaedics. *Computers in biology and medicine*, 25(2):183–191, 1995.

S. M. Ott. Cortical or trabecular bone: What's the difference? *American journal of nephrology*, 47(6):373–376, 2018.

N. S. Ottosen and M. Ristinmaa. *The mechanics of constitutive modeling*. Elsevier, 2005.

C. Pabinger, H. Lothaller, N. Portner, and A. Geissler. Projections of hip arthroplasty in OECD countries up to 2050. *HIP International*, 28(5):498–506, 2018.

A. Palit, R. King, Y. Gu, J. Pierrepont, D. Simpson, and M. A. Williams. Subject-specific surgical planning for hip replacement: A novel 2D graphical representation of 3D hip motion and prosthetic impingement information. *Annals of biomedical engineering*, 47(7):1642–1656, 2019.

S. Parithimarkalaignan and T. Padmanabhan. Osseointegration: an update. *The Journal of Indian Prosthodontic Society*, 13(1):2–6, 2013.

F. Pauwels. Funktionelle Anpassung des Knochens durch Längenwachstum. In *Gesammelte Abhandlungen zur funktionellen Anatomie des Bewegungsapparates*, pages 400–423. Springer, 1965.

E. Pavarino, L. A. Neves, J. M. Machado, M. F. de Godoy, Y. Shiyou, J. C. Momente, G. F. Zafalon, A. R. Pinto, and C. R. Valêncio. Free tools and strategies for the generation of 3d finite element meshes: modeling of the cardiac structures. *International journal of biomedical imaging*, 2013, 2013.

L. Peng, J. Bai, X. Zeng, and Y. Zhou. Comparison of isotropic and orthotropic material property assignments on femoral finite element models under two loading conditions. *Medical engineering & physics*, 28(3):227–233, 2006.

H. Pfister, J. Hardenbergh, J. Knittel, H. Lauer, and L. Seiler. The VolumePro real-time ray-casting system. In *Proceedings of the 26th annual conference on Computer graphics and interactive techniques*. Association for Computing Machinery, 1999.

D. M. Pflüger. *Spatially adaptive sparse grids for high-dimensional problems*. PhD thesis, Technische Universität München, 2010.

G. Poplau. *Multivariate Periodic Interpolation by Translates and Applications*. PhD thesis, University of Rostock, 1995 (Germany), 1995.

D. Porter. Pragmatic multiscale modelling of bone as a natural hybrid nanocomposite. *Materials Science and Engineering: A*, 365(1-2):38–45, 2004.

N. V. Queipo, R. T. Haftka, W. Shyy, T. Goel, R. Vaidyanathan, and P. K. Tucker. Surrogate-based analysis and optimization. *Progress in aerospace sciences*, 41(1):1–28, 2005.

S. S. Rajaee, J. C. Campbell, J. Mirocha, and G. D. Paiement. Increasing burden of total hip arthroplasty revisions in patients between 45 and 64 years of age. *JBJS*, 100(6):449–458, 2018.

S. Razavi, B. A. Tolson, and D. H. Burn. Review of surrogate modeling in water resources. *Water Resources Research*, 48(7), 2012.

B. Reggiani, L. Cristofolini, E. Varini, and M. Viceconti. Predicting the subject-specific primary stability of cementless implants during pre-operative planning: preliminary validation of subject-specific finite-element models. *Journal of Biomechanics*, 40(11):2552–2558, 2007.

G. Regling. *Wolff's Law and Connective Tissue Regulation: Modern Interdisciplinary Comments on Wolff's Law of Connective Tissue Regulation and Rational Understanding of Common Clinical Problems*. Walter de Gruyter, 2011.

T. J. Reiter. Knochen – eine selbstoptimierende Struktur? In *Evolution und Optimierung: Strategien in Natur und Technik*, pages 121–136. S. Hierzel Wissenschaftliche Verlagsgesellschaft Stuttgart, 1995.

T. J. Reiter. *Functional adaption of bone and application in optimal structural design*. VDI-Verlag, 1996.

N. Reznikov, R. Shahar, and S. Weiner. Bone hierarchical structure in three dimensions. *Acta biomaterialia*, 10(9):3815–3826, 2014.

J. Riegel, W. Mayer, and Y. van Havre. FreeCAD, 2016.

J. Ro, P. Kim, and C. S. Shin. Optimizing total hip replacement prosthesis design parameter for mechanical structural safety and mobility. *International Journal of Precision Engineering and Manufacturing*, 19(1):119–127, 2018.

W. Roux. Der züchtende Kampf der Teile, oder die "Teilauslese" im Organismus (Theorie der "funktionellen Anpassung"). *Leipzig: Wilhelm Engelmann*, 1881.

C. W. Rowley. Model reduction for fluids, using balanced proper orthogonal decomposition. *International Journal of Bifurcation and Chaos*, 15(03):997–1013, 2005.

D. K. Roy and B. Datta. A review of surrogate models and their ensembles to develop saltwater intrusion management strategies in coastal aquifers. *Earth Systems and Environment*, 2(2): 193–211, 2018.

R. Russell and L. F. Shampine. A collocation method for boundary value problems. *Numerische Mathematik*, 19(1):1–28, 1972.

F. A. Sabet, A. Raeisi Najafi, E. Hamed, and I. Jasiuk. Modelling of bone fracture and strength at different length scales: a review. *Interface focus*, 6(1):20150055, 2016.

G. Saravana Kumar and M. Gupta. Patient specific parametric geometric modelling of cementless hip prosthesis. In *Proceedings of the 5th international conference on advanced research in virtual and rapid prototyping, Leiria*, volume 28, 2011.

A. Sarmiento and T. Gruen. Radiographic analysis of a low-modulus titanium-alloy femoral total hip component. two to six-year follow-up. *The Journal of bone and joint surgery. American volume*, 67(1):48–56, 1985.

R. A. Schapery. A simple collocation method for fitting viscoelastic models to experimental data. Technical report, California Institute of Technology, 1962.

R. K. Schenk and D. Buser. Osseointegration: a reality. *Periodontology 2000*, 17(1):22–35, 1998.

E. Schileo, F. Taddei, A. Malandrino, L. Cristofolini, and M. Viceconti. Subject-specific finite element models can accurately predict strain levels in long bones. *Journal of biomechanics*, 40(13):2982–2989, 2007.

P. Schneider, P. Berger, E. Moll, C. Reiners, and W. Börner. Getrennte Messung von Kompakta- und Spongiosadichte mit einem Transversal-Rotations-Scanner. In *RöFo-Fortschritte auf dem Gebiet der Röntgenstrahlen und der bildgebenden Verfahren*, volume 143(8), pages 178–182. Georg Thieme Verlag Stuttgart · New York, 1985.

B. W. Schreurs and G. Hannink. Total joint arthroplasty in younger patients: heading for trouble? *The Lancet*, 389(10077):1374–1375, 2017.

E. Schrödinger. *What is life? The physical aspect of the living cell and mind*. Cambridge University Press Cambridge, 1944.

A. H. Shaikh. Preoperative planning of total hip arthroplasty. In *Total Hip Replacement-An Overview*. IntechOpen, 2018.

A. K. Singh. *Mechanics of solids*. PHI Learning Pvt. Ltd., 2007.

W. S. Slaughter. *The linearized theory of elasticity*. Springer Science & Business Media, 2012.

S. A. Smolyak. Quadrature and interpolation formulas for tensor products of certain classes of functions. In *Doklady Akademii Nauk*, volume 148(5), pages 1042–1045. Russian Academy of Sciences, 1963.

F. Sprengel. A unified approach to error estimates for interpolation on full and sparse Gauß-Chebyshev grids. *Rostock. Math. Kolloq.*, 51:51–64, 1997.

E. L. Steinberg, N. Shasha, A. Menahem, and S. Dekel. Preoperative planning of total hip replacement using the TraumaCad system. *Archives of orthopaedic and trauma surgery*, 130 (12):1429–1432, 2010.

A. Sujar, A. Meuleman, P.-F. Villard, M. Garcia, and F. Vidal. gVirtualXRay: virtual X-ray imaging library on GPU. In *Computer Graphics and Visual Computing*, pages 61–68. The Eurographics Association, 2017.

D. Swinehart. The Beer-Lambert law. *Journal of chemical education*, 39(7):333, 1962.

S. Szmukler-Moncler, H. Salama, Y. Reingewirtz, and J. Dubruille. Timing of loading and effect of micromotion on bone – dental implant interface: review of experimental literature. *Journal of biomedical materials research*, 43(2):192–203, 1998.

S. Tabaković, M. Zeljković, and A. Živković. General parametric model of the body of the total hip endoprosthesis. *Acta Polytechnica Hungarica*, 11(1):227–246, 2014.

L. Taber. Biomechanics of growth, remodeling, and morphogenesis. *Applied mechanics reviews*, 48(8):487–545, 1995.

F. Taddei, M. Viceconti, M. Manfrini, and A. Toni. Mechanical strength of a femoral reconstruction in paediatric oncology: a finite element study. *Proceedings of the Institution of Mechanical Engineers, Part H: Journal of Engineering in Medicine*, 217(2):111–119, 2003.

C. Truesdell, S. Flügge, S. Nemat-Nasser, and W. Olmstead. Mechanics of Solids II. *Journal of Applied Mechanics*, 42:247, 1975.

Y. Tyson, O. Rolfson, J. Kärrholm, N. P. Hailer, and M. Mohaddes. Uncemented or cemented revision stems? Analysis of 2,296 first-time hip revision arthroplasties performed due to aseptic loosening, reported to the swedish hip arthroplasty register. *Acta orthopaedica*, 90 (5):421–426, 2019.

M. Üffinger, S. Frey, and T. Ertl. Interactive high-quality visualization of higher-order finite elements. In *Computer Graphics Forum*, volume 29(2), pages 337–346. Wiley Online Library, 2010.

J. Van Houcke, V. Khanduja, C. Pattyn, and E. Audenaert. The history of biomechanics in total hip arthroplasty. *Indian journal of orthopaedics*, 51(4):359, 2017.

M. Viceconti. *Multiscale modeling of the skeletal system*. Cambridge University Press, 2012.

M. Viceconti, L. Bellingeri, L. Cristofolini, and A. Toni. A comparative study on different methods of automatic mesh generation of human femurs. *Medical engineering & physics*, 20 (1):1–10, 1998a.

M. Viceconti, C. Zannoni, and L. Pierotti. TRI2SOLID: an application of reverse engineering methods to the creation of CAD models of bone segments. *Computer Methods and Programs in Biomedicine*, 56(3):211–220, 1998b.

M. Viceconti, R. Lattanzi, B. Antonietti, S. Paderni, R. Olmi, A. Sudanese, and A. Toni. CT-based surgical planning software improves the accuracy of total hip replacement preoperative planning. *Medical engineering & physics*, 25(5):371–377, 2003.

M. Viceconti, M. Qasim, P. Bhattacharya, and X. Li. Are CT-based finite element model predictions of femoral bone strengthening clinically useful? *Current osteoporosis reports*, 16 (3):216–223, 2018.

J. Villadsen and W. E. Stewart. Solution of boundary-value problems by orthogonal collocation. *Chemical Engineering Science*, 22(11):1483–1501, 1967.

W. Voigt et al. *Lehrbuch der Kristallphysik*, volume 962. Teubner Leipzig, 1928.

H. D. Wagner and S. Weiner. On the relationship between the microstructure of bone and its mechanical stiffness. *Journal of Biomechanics*, 25(11):1311–1320, 1992.

H. Weinans, R. Huiskes, and H. Grootenboer. The behavior of adaptive bone-remodeling simulation models. *Journal of biomechanics*, 25(12):1425–1441, 1992.

D. F. Wiley, H. Childs, B. Hamann, and K. Joy. Ray casting curved-quadratic elements. In *VisSym*, pages 201–210, 2004.

K. Willcox and J. Peraire. Balanced model reduction via the proper orthogonal decomposition. *AIAA journal*, 40(11):2323–2330, 2002.

D. F. Williamson, R. A. Parker, and J. S. Kendrick. The box plot: a simple visual method to interpret data. *Annals of internal medicine*, 110(11):916–921, 1989.

J. Wolff. Das Gesetz der Transformation der Knochen. *Hirschwald*, pages 1–152, 1892.

S.-Y. Woo, B. Simon, W. Akeson, and M. McCarty. An interdisciplinary approach to evaluate the effect of internal fixation plate on long bone remodeling. *Journal of biomechanics*, 10(2): 87–95, 1977.

P. Wriggers. *Nonlinear finite element methods*. Springer Science & Business Media, 2008.

P. Wriggers and G. Zavarise. Computational contact mechanics. *Encyclopedia of computational mechanics*, 2004.

K. Wright. Chebyshev collocation methods for ordinary differential equations. *The Computer Journal*, 6(4):358–365, 1964.

W. Yang and A. C. Peet. The collocation method for bound solutions of the Schrödinger equation. *Chemical physics letters*, 153(1):98–104, 1988.

Z. Yosibash, D. Tal, and N. Trabelsi. Predicting the yield of the proximal femur using high-order finite-element analysis with inhomogeneous orthotropic material properties. *Philosophical Transactions of the Royal Society A: Mathematical, Physical and Engineering Sciences*, 368 (1920):2707–2723, 2010.

P. Young, T. Beresford-West, S. Coward, B. Notarberardino, B. Walker, and A. Abdul-Aziz. An efficient approach to converting three-dimensional image data into highly accurate computational models. *Philosophical Transactions of the Royal Society A: Mathematical, Physical and Engineering Sciences*, 366(1878):3155–3173, 2008.

L. Zagra. Advances in hip arthroplasty surgery: what is justified? *EFORT open reviews*, 2(5): 171–178, 2017.

C. Zenger and W. Hackbusch. Sparse grids. Technical report, Mathematisches Institut und Institut für Informatik, Technische Universität München, 1990.

K. Zenk, S. Finze, D. Kluess, R. Bader, J. Malzahn, and W. Mittelmeier. Einfluss der Erfahrung des Operateurs in der Hüftendoprothetik. *Der Orthopäde*, 43(6):522–528, 2014.

C. Zhang, C. H. Yan, and W. Zhang. Cemented or cementless fixation for primary hip arthroplasty – evidence from the international joint replacement registries. *Annals of Joint*, 2017.

O. C. Zienkiewicz and J. Zhu. The superconvergent patch recovery (SPR) and adaptive finite element refinement. *Computer Methods in Applied Mechanics and Engineering*, 101(1-3): 207–224, 1992.

O. C. Zienkiewicz, R. L. Taylor, P. Nithiarasu, and J. Zhu. *The finite element method*, volume 3. McGraw-hill London, 1977.